INVESTIGATION OF DYNAMIC BEHAVIOR OF BRITTLE SOLIDS BY DISCRETE SYSTEMS

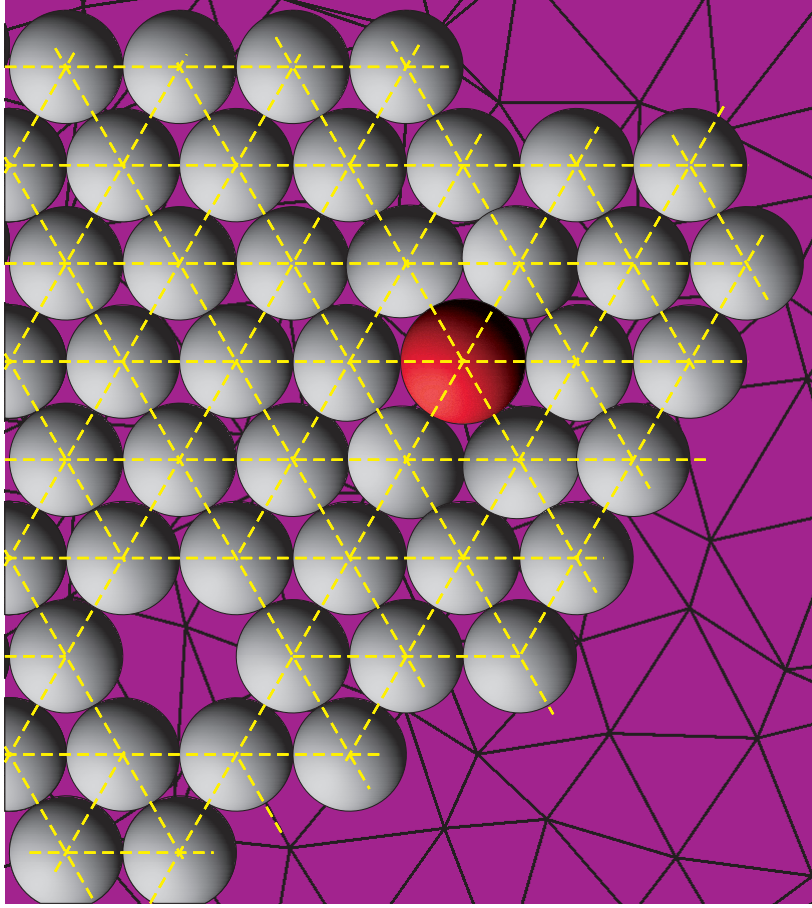

S. Mastilovic

INVESTIGATION OF DYNAMIC BEHAVIOR OF BRITTLE SOLIDS BY DISCRETE SYSTEMS

Sreten Mastilovic
Union University

Faculty of Construction Management
Union University, Belgrade, Serbia

Sreten Mastilović

INVESTIGATION OF DYNAMIC BEHAVIOR OF BRITTLE SOLIDS BY DISCRETE SYSTEMS

Izdavač:

Fakultet za graditeljski menadžment
Univerziteta Union
Cara Dušana 62-64, Beograd

Recenzenti:

Prof. dr Dragoslav Šumarac, dipl. inž. građ.
V. Prof. dr Vesna Milošević-Mitić, dipl. inž. maš.

Štampa:

"Stillart", Beograd

Tiraž: 100

ISBN 978-86-85175-02-2

Beograd • 2008

Dedicated to the memory of Professor Dusan Krajcinovic

PREFACE

With the remarkably rapid growth of computer capabilities and corresponding advance of numerical algorithms as background, the landscape of the engineering and scientific research is continually changing. In the pre-computer era, the physical sciences were characterized by interplay between theory and experiment, both necessarily simplified to eliminate the complexities that rendered the phisical phenomena impossible to tackle. In the last two-three decades, the computer technology surge altered substantially this relationship by enriching the research by a new element: the computer experiment. The change is far reaching indeed. The computer simulations significantly pushed the envelope of "solvable" problems. When they, by constantly demanding more accurate inputs from both theorists and experimentalists, manage to come very close to capturing the reality of a phenomenon, they become an extremely powerful tool indispensible in interpretation of the experimental results at the spatial and temporal scales beyond the reach of ever-developing experimental techniques. More than that: the virtual laboratory enables us to perform experiments that are beyond imagination in the actual laboratory, with practically unlimited level of control.

The objective of the research efforts reviewed in this monograph was threefold. First, to identify patterns and dominant aspects of dynamic response of idealized brittle solids subjected to high strain rates. Second, to propose simple, approximate, design oriented models needed to capture some of those salient features. Third, to investigate universal trends in which disorder and strain rate influence that dynamic response. The outlined approach leads to rational estimates of the radial tractions required to expand dynamically a cylindrical cavity and, consequently, the forces on the projectile nose resisting penetration; and eventually, the corresponding penetration depth of the superior-strength projectile through the infinite brittle medium. The models are based on the micromechanics of deformation and damage evolution in the generic brittle material with random microstructure and inferior tensile strength. The considered problems are, in addition to ballistics, also frequently encountered in mining, metalworking, transportation, etc. The proposed models accounts for the prominent properties of brittle materials: a random microstructure, pressure-dependent shear strength, inferior tensile strength and presence of process induced micro-defects; and the characteristic deformation features such as the rate-dependent fracture pattern, granular flow, and deterioration of the effective material properties. The effect of

"pre-existing" material imperfections on the material properties and their change in the course of deformation is an indication that a rational model should be sought within the scope of damage mechanics.

The strategy selected in this study is to use the virtual laboratory experiments to reduce the dependence on actual tests (often too difficult and/or expensive, if not impossible, to perform) and provide a reasonably detailed picture of the state of material and mechanical fields in the infinite brittle target. Due to the extreme loading conditions, the concepts of strain, stiffness tensor, damage and temperature are, at best, conditionally acceptable since the corresponding deformation process is non-local, non-linear and non-equilibrated. To eliminate large spatial and temporal fluctuations the "local" values of these fields are determined by volume averaging. As a consequence, the model resolution is rather coarse and the results are primarily directed to the estimates of the global parameters of the problem which are, fortunately, most important for engineering purposes.

The approximation of a solid by an ensemble of interacting particles (so called, lattice, spring-network, or discrete models) is selected for at least three reasons. First, the introduction of morphological and structural disorder is straightforward. Second, the selection of the constitutive relations is not arbitrary since it can be, in principle, inferred from the molecular dynamics simulations on the sub-meso scales. Finally, there is no need for developing time-consuming numerical techniques to track the material interfaces. The rationale for the selected strategy is fully supported by the simulation results.

This monograph grew out of my dissertation "Dynamic Loading of Brittle Materials with Random Microstructure" presented at Arizona State University (1997) in partial fulfillement of the requirements for the degree Doctor of Philosophy. The offsprings of that dissertation were numerous research papers prepared in collaboration with the late Professor Dusan Krajcinovic. The monograph is organized in five chapters describing the major subject areas; the chapters are divided into sections and the sections into thematic subsections. It is important to note that this book is not a review monograph of the discrete numerical methods, but a brief treatise on a narrow multidisciplinary research area. Thus, many valuable references in the topical areas are surely inadverantly left out.

The material in Section 2.1 is a brief survey of standard background information on conventional molecular dynamics. The introduction to particle dynamics models presented in Section 2.2 is based mostly on Krajcinovic and Mastilovic (1999) and Mastilovic and Krajcinovic (1999a). The core of the monograph, which comprises Chapters 3 and 4 describing the numerical simulations and the corresponding analytical modelling, is founded primarily on the following publications: Mastilovic

and Krajcinovic (1999b) (Sections 3.1 through 3.3); Mastilovic and Krajcinovic (1999a) (Section 3.4 and 4.1); Krajcinovic and Mastilovic (2001a) (Section 3.4); and Mastilovic et al. (2008) (Subsection 3.3.1). Section 4.2, concerned with the penetration depth modelling, follows closely analysis in Mastilovic and Krajcinovic (1999c). The topics covered in Appendices A and D are originally published in Mastilovic (2008) and Mastilovic (accepted).

Finally, the mentioned advent of high productivity computing takes its toll on many results presented in this study. Many numerical models that pushed the envelope of PC performace 10-15 years ago are orders of magnitude behind the current state-of-the-art, which is an unavoidable drawback of postponed publication in rapidly developing research areas. Therefore, as I prepared the manuscript, I had to resist a strong urge to re-do many simulations presented herein; successfully, I am happy to admit.

Last but not least, I am indepted to many for help and support during the years of work shaped in this monograph; no one is named here but no one is forgotten.

S.M.

CONTENTS

CHAPTER 1

INTRODUCTION

1.1 GENERAL REMARKS

At the simplest level, in order to understand fracture, materials could be categorized as brittle and ductile.[1] Phenomenologically, a fracture is classified as perfectly brittle if it takes place in the course of elastic deformation, suddenly and without observable warning. The brittle materials subjected to the extreme loading power (defined by the magnitude and the rate of externally imparted energy) tend to shatter since the micro-defects, most notably microcracks, tend to propagate unabatedly and cut through atomic bond in razor-like manner. Finkel (1970) labels a fracture brittle if the specimen elastic energy suffices for fracture occurrence and completion, that is, if the fracture process is autocatalytic and energy consumption low. In contrast, a fracture is said to be ductile if it is preceded by a protracted regime of hardening and significant accumulation of inelastic strains and expenditure of thermal energy. Thus, the ductile materials subjected to the extreme loading power tend to deform substantially as cracks blunt and propagate with great difficulty. Micromechanics study of Rice and Thompson (1974) demonstrated that the degree of brittleness of the crack propagation is on microscopic scale decided by the outcome of the competition between the atomistic decohesion (Griffith's cleavage) and emission rate of the blunting crack-tip dislocations.

The deformation of damage tolerant materials (that is, the materials susceptible to micro-cracking: ceramics, rocks, concrete, composites, epoxy, silicone, glass, iron, human bones, etc.), laterally confined and subjected to far-field compression, is sometimes referred to as being quasi-brittle and sometimes quasi-ductile since the failure of the specimen is also preceded by the hardening, and sometimes also the

[1] Brittleness and ductility are, strictly speaking, not just material properties but also depend on temperature, confining pressure, and loading rate.

softening, phase. Hardening in these materials is attributed to the gradual increase of micro-defects density and corresponding decrease of components of the stiffness tensor (Krajcinovic and Mastilovic, 1995). The slope of the softening phase, that follows the peak of the stress-strain curve, ranges from being steep to being rather mild (Section 3.3). The orientation-weighted density of ruptured bonds (damage) is the measure of irreversible changes of the material microstructure in the course of quasi-brittle deformation (Krajcinovic et al., 1998). The type of the deformation process and failure mode results from a subtle interplay of boundary conditions, specimen size and shape, material texture on all scales, existing defects, and, last but not least, the loading power.

The application of an external load to a solid is, by definition, a dynamic event on at least some spatial and temporal scale(s). However, when the external forces are applied slowly, the deformation process can be justifiably approximated on macroscale by a temporal sequence of static-equilibrium states. This approxiametion is justifiable if each non-equilibrium state is *close* to its acompanying equilibrium state. (The latter is equilibrated by a set of fictitious thermodynamic forces conjugate to a set of history parameters called internal variables.) The non-equilibrium state and its acompanying equilibrium state are considered being close if the ratio of the relaxation time (characterizing the transition from the former to the latter state) and the characteristic external time (e.g., the dwell time under constant loading) is small. The ratio between the characteristic internal and external times under the given mechanical load is called Deborah number. This class of deformation processes, commonly referred to as being quasi-static, is treated extensively in the classical solid mechanics. On the other side of the loading spectrum are the impact events and other transient phenomena characterized by the rapid change of external forces, propagation of stress waves, absence of steady-state conditions, and the essential role of the inertial forces in deformation process.[2] It is crucial for a rational model of any transient phenomenon to recognize these aspects of high strain rate events and incorporate them into the governing equations (Kipp et al., 1980).

The traditional continuum models, based on irreversible thermodynamics with internal variables, consist of the equations of conservation of linear and angular momentum, conservation of energy, and constitutive relations. The second law of thermodynamics is the constraint that must be satisfied by the selected parameters of continuum model. Based on the principles of determinism and local action,[3] and

---

[2] The wave propagation may be envisioned on atomic scale as a succession of impacts between adjacent atoms (Mayers, 1994).

[3] A majority of traditional models of continuum mechanics are, in the absence of a material characteristic length, local. Local models are based on the principle of local action, according to which the response at a "continuum particle" is determined if the conditions in its

material objectivity and invariance (Billington and Tate, 1981), models of this class are appropriate if:

- the internal variables are related to the microscopic modes of inelastic (irreversible) deformation,
- the material within volume element is statistically homogeneous, and
- Deborah number is small (Krajcinovic and Mastilovic, 2000, 2001a).

Continuum models of damage mechanics, developed along traditional lines of plasticity, can predict the onset and mode of failure only if the failure threshold can be determined from the receding thermodynamic state (e.g., Voyiadjis and Kattan, 1987; Lubarda and Krajcinovic, 1995; Lubarda et al., 1996). These conditions are satisfied when deformation process depends primarily on volume and time averages of stress, strain, and damage. In many cases, the constitutive equations are further simplified by assuming that the evolution of internal variables (such as a damage parameter) can be determined from a potential. The potential exists only if the "local dependence" assumption (Rice, 1991) is satisfied, that is, in the absence of direct interaction of defects. The damage mechanics models of damage evolution that depend on the sign of normal stress and interdependence of ductile and brittle deformation modes (Ortiz, 1985; Voyiadjis and Kattan, 1987; Lubarda and Krajcinovic, 1995) are primarily of formal value since they did not address all above criteria.

The objective of micromechanical models is to eliminate some of the arbitrariness of continuum models by selecting internal variables in a manner that relates the inelastic deformation and the irreversible change of the microstructure (Krajcinovic and Mastilovic, 1999). These models are successful in providing correct estimates of effective properties of damaged material (thermodynamic state) although the analytical solutions are limited to dilute concentrations of the simple-shape micro-defects (for extensive treatment refer to, for instance, Nemat-Nasser and Hori, 1993; Krajcinovic, 1996; Lemaitre, 1996). Most of micromechanical models assume that the matrix is homogeneous and isotropic. The effective properties of the matrix (which, in principle, could be determined by homogenization from the nano-scale discrete models) should account for the nano-scale defects, both pre-existing and induced. Moreover, the resolution length of these models is commensurate to the size of defects. The effect of micro-defects on the effective transport properties of the

---

infinitesimal neighborhood are known (Billington and Tate, 1981). The principle of local action is inherent to the derivation of "material" properties and field equations from the consideration of infinitesimal elements of the medium that disregards fluctuations of mechanical fields in the exterior of these elements. In reality, each material with a microstructure is necessarily nonlocal (Kunin, 1983).

representative volume is determined using effective field or medium approximations (Kunin, 1983; Nemat-Nasser and Hori, 1993; Krajcinovic, 1996; etc.). Assuming that the material within the volume is statistically homogeneous (Krajcinovic, 1997) these effective properties are intensive. These models are based on the assumptions that:

- the statistical properties of all relevant random fields do not depend on the exact locations of heterogeneities (translational invariance), and
- the external field of each defect is equal to the externally applied field.

In this approximation a many-defect problem is reduced to many single-defect problems. The homogenization is objective if the volume is self-similar (scale invariance).

Finally, the novel micromechanical models of damage evolution in materials with random texture (energy barriers affecting micro-crack propagation) are formulated within the framework of statistical micromechanics (see for instance, Rinadi et al., 2007; Bazant, 2008; and references therein), but such models are, to my knowledge, limited at present to the quasi-static phenomena.

At the risk of stating the obvious, the analytical modelling of high velocity penetration of a projectile through a brittle solid is beset with the complexity coupled with a dearth of detailed test data. As already mentioned, the typical penetration process is a catastrophic event characterized by large deformations and high strain rates, encompassing inertia effects, wave propagation, fracture, mass transport, and phase transitions that take place within few microseconds. The identification of relevant material properties is very often obscured by the inherent complexities of this non-equilibrium, nonlocal process that are not often encountered in the literature dealing with the classical solid mechanics. The deformation process is adiabatic with highly non-uniform *instantenous* temperature field. The penetrator is often locally melted, deformed, and eroded to a fraction of its original mass. In view of the imparted loading power it is obvious that measurement of the strain, damage and temperature fields in the penetrator and target is a Sisyphean task.

1.2 FAILURE PHENOMENOLOGY OF PENETRATION PROCESS

The penetration of a long rod (typically made of heavy tungsten alloys or depleted uranium) into a well confined[4] brittle target is characterized by several distinctive processes (Bless et al., 1987). At fixed target and penetrator geometries and material properties, the fracture pattern and evolution depend mainly upon striking velocity. A qualitative picture observed in the laboratory and field tests can be classified into two large classes: low- and high-velocity impact.

In the case of low-velocity impact the projectile forms a shallow crater without penetrating deeply into the target (Fig. 1.1). Consequently, the low velocity is, within the context of the present study, defined as the velocity at which the deep penetration, i.e. emergence of a notable tunneling phase, does not occur.

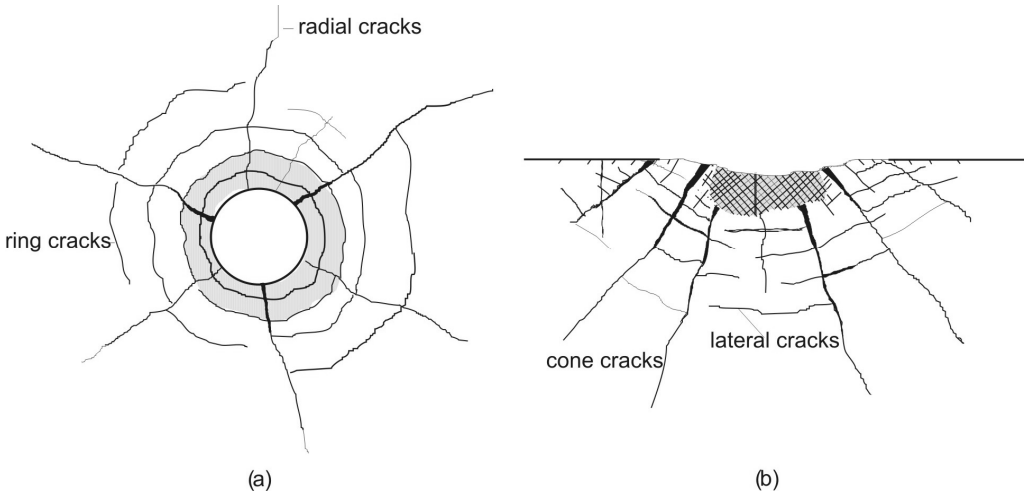

Fig. 1.1. Low-velocity impact - fracture pattern: (a) top view; (b) sectional view.

The phenomenology of the low-velocity impact is considered first since it also entails few qualitative features observed in the initial and terminal phases of the high-velocity penetration. Immediately after the impact, the stress field in the target is elastic, and the largest tensile stresses are radial (the Boussinesq stress field, see for instance Shockey et al., 1990). Therefore, the first cracks formed behind the Rayleigh

[4] The target system is typically made of the ceramic, concrete or rock block encased in a steel box formed by the cover and rear confinement plates and the heavy lateral walls.

stress wave front are ring cracks that are concentric about the impact site (Fig. 1.1a). In the course of deformation some of the ring cracks continue to grow driven by the principal tensile stress (at an angle $25-75°$ with respect to the flight path). Several large Hertzian cone cracks extend through the target (Evans et al., 1977). Other ring cracks remain shallow, arrested only a millimeter or so beneath the surface (Fig. 1.1b).

As the penetrator advances, the compressive strength is exceeded in the target material within the immediate neighborhood of the contact zone. Extensive microcrack nucleation process takes place directly ahead of the penetrating rod. Eventually, a zone of heavily damaged material is formed. The development of this zone is a prerequisite for the penetration since it enables the mass transport and provides a path of least resistance for further advance of the penetrator. Several large radial cracks extending outward from the process zone are caused by the principal circumferential tensile stress (Fig. 1.1a). Depending on the confinement level, these radial cracks may reach the target boundaries, degrading the strength and causing, ultimately, the structural failure of the target.

Finally, during the release-wave unloading, lateral cracks form parallel to the impact surface (Fig. 1.1b). These cracks intersect both cone and radial cracks causing the fragmentation of the brittle target. According to Grady's energy analysis (1982) the fragment sizes scale inversely with strain rate as $d \propto \dot{\varepsilon}^{-2/3}$. Consequently, the fragment sizes increase with the distance from the impact zone. It should be emphasized that the large radial macrocracks do not facilitate the penetration process directly in a heavily confined target. Instead, they promote penetration indirectly by weakening the confinement imposed on the heavily damaged material (Shockey et al., 1990).

A quite different target response is observed during the high-velocity penetration (Fig. 1.2). Immediately upon the impact, a high-pressure shock wave, formed at the contact site, propagates through both the target and projectile. The target material in the contact zone is fragmented. Transport of the fragments away from the vicinity of the contact zone, commonly called cratering, marks the initial phase of penetration. In the vicinity of the projectile path the brittle target material is pulverized or at the very least inundated by microcracks. This heavily deformed material is transported away from the projectile path, and some of the fragments are ejected from the crater. The next, tunneling, phase of penetration consists of formation of a cylindrical hole (canal) through the target.[5] The cavity is, in brittle materials, formed by crushing the material in the process region and pushing it away from the projectile path.

---

[5] The onset of the tunneling phase is usually considered to be the penetration depth of approximately $4a_P$, where a_P is the initial projectile shank radius (Fig. 1.2).

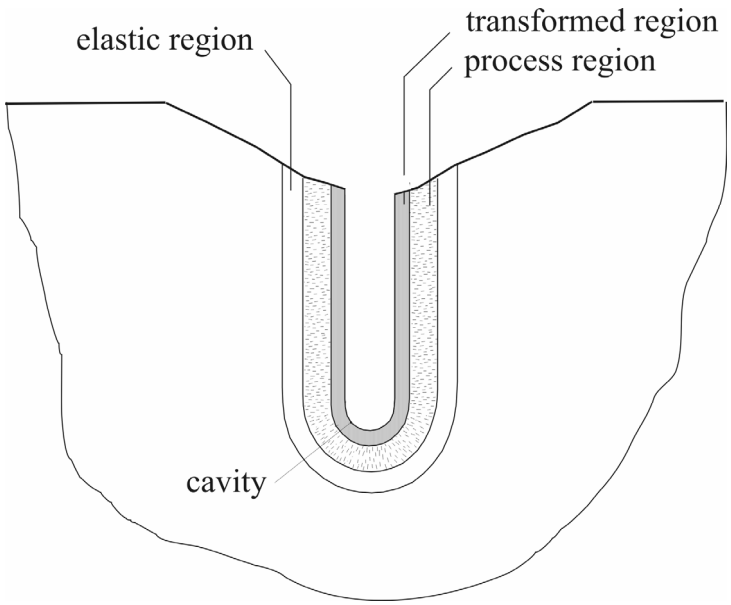

Fig. 1.2. High-velocity penetration - damage pattern.

The stress waves attenuate with the distance from the contact zone. Consequently, the accumulated damage (microcrack density) also decreases rapidly with increasing distance from the impact zone (Strassburger and Senf, 1996). The material closest to the forming cavity (subjected to the largest stresses) is comminuted (crushed, pulverized, transformed). Next to it is a damaged layer, densely populated by microcracks. Finally, the material behind the shock front and ahead of damage front is elastically deformed (Fig. 1.2). The exact geometry and extent of these three regions depend on the target and penetrator materials, striking velocity, and confinement. The end of penetration is marked by several macrocracks extending from the bottom of the tunnel (Hauver et al., 1991); the fracture pattern is similar to that described in relation to the low-velocity impact.

As mentioned before, in order for the penetrator to advance, the target material directly ahead of the penetrator proximal end has to be pushed away from its path, which is made possible by pulverization of the target material and ejection of debris. These processes are almost simultaneous and their chronological order is established by the dynamics of stress field evolution in the confined target. It is important to note that,[6] except for the initial instant of impact, "penetration in brittle materials means penetration in a fractured target" (Sternberg, 1989). Hence, the knowledge of the

[6] Except in the case when the striking velocity of the projectile is higher than the velocity of longitudinal elastic wave propagation.

target material parameters in its pristine state is not sufficient. Since the material resistance is inversely proportional to the extent of the target fracture, a rational prediction of the extent of damage as the function of the loading power is one of the important tasks of penetration mechanics.

The lateral expansion of comminuted material is resisted by the stiffness of the surrounding material which has both chemical (dependent on the cohesive strength) and geometrical (dependent of the imposed structural confinement) components. The pressure build-up in the contact zone increases with the penetration resistance of the target. The macrocracks facilitate the penetration indirectly by reducing the constraint level imparted on the comminuted material. The experimental data reported by Strassburger and Senf (1995) suggest that even the ceramic material melts in the zone of large temperatures close to target-penetrator interface. The extent of comminution decreases rapidly with the distance from the impact zone due to the decay of the imparted energy.

Finally, the different damage and fracture modes that occur in the course of penetration event are characterized by different propagation velocities (Strassburger and Senf, 1995). Most notably, the velocity of propagation of the localized macrocracks and the rate of growth of the homogeneous regions of distributed microcracks are quite different. The terminal velocity of propagating macrocracks is approximately equal to one-half of the Rayleigh wave velocity.[7] In contrast, at high loading rates the velocity of the process zone front, that separates the elastic and process regions, approaches the velocity of longitudinal elastic waves C_L.

[7] The classical result of continuum theory (Yoffe, 1951), according to which as the crack length increases the velocity of crack propagation asymptotically approaches the Rayleigh wave velocity (C_r), is still considered to be exact (Freund, 1990) even though, to our knowledge, it was never experimentally confirmed. Experimental results (e.g., Senf and Winkler, 1997) and atomistic simulations (e.g., Sieradzki et al., 1988; Zhou et al., 1996) repeatedly suggest that a more realistic estimate of the crack tip terminal velocity is approximately equal to $0.5C_r$. It is interesting to note that although the recent simulations by Buehler et al. (2004) confirmed the Yoffe's prediction that crack branching starts at $0.7C_r$, they managed to achieve the continuum mechanics predicted terminal crack velocity equal to C_r only along a *weak interface*. Nonetheless, the recent theoretical and experimental findings suggest that the upper bound for the crack velocity lies far below C_r (Cox et al., 2005, and references therein).

1.3 PENETRATION MECHANICS MODELS

Engineering models developed to tackle the problems that involve high strain rate loading are commonly divided into three large classes: empirical, analytical, and numerical.

The empirical approach is limited to the formulation of equations that correlate the cause with the outcome inferred from the experimental data. The empirical equations (quasi-analytical "models") are traditionally used to replicate the test data, provide guidance for further experiments, and evaluate performance characteristics of various materials or structures for a particular configuration. The predictive ability of empirical models is generally not satisfactory when the circumstances and configuration are changed – predictions that extrapolate available experimental data to materials, geometries, and strain rates outside the ranges of the performed tests are, generally, unreliable. Although the correlation of the test data may provide some useful insights into the problem, it is generally believed that the fundamental understanding of the underlying physical mechanisms can be seldom gained from purely empirical models (Jonas and Zukas, 1978; Mayers, 1994).

Analytical approaches (either continuum or micromechanical) are often based on simplified models incorporating the perceived dominant aspects of physical phenomena and ignoring complexities of the "second-order" importance. As discussed in Section 1.1, these models are commonly based on the conservation laws, simplified by assumptions based on the available experimental data and other insights into the particular problem, either inferred from experience or borrowed from the theories of inelastic deformation of solids. The objective of analytical modelling is, in general, limited to the estimates of global parameters (such as for instance, in case of penetration mechanics: depth of penetration, crater dimensions, residual length of the projectile). These models, although limited in scope, can be, nonetheless, useful for the development of an understanding of the dominant physical mechanisms that govern the dynamic deformation processes in materials. The analytical models, unlike the purely empirical counterparts, may also be used as predictive tools as long as the assumptions used in the process of solving the problem are not violated. Distinction between empirical (quasi-analytical) and analytical approaches is somewhat blurred in literature since "many empirical observations and curve-fitting schemes are referred to as models" (Nicholas and Recht, 1990).

1.3.1 Numerical Algorithms

The computer simulations have no viable alternative if a complete thermo-mechanical analysis of penetration event is required. Simulations are, for instance, unavoidable in analysis of the complex ballistic problems dealing with three-dimensional stress state, such as oblique impacts. The reliance on computations is especially necessitated by the stochastic nature of deformation modes and patterns in brittle materials that requires considerations of a representative sample of physical realizations of given statistics. The traditional analytical analyses of complex penetration problems based on elasticity, inelasticity and, more recently, damage mechanics, are virtually impossible in view of the mathematical complexities. Instead, the set of field equations must be solved numerically using the finite difference or finite element discretization schemes. Computational codes, custom made for the large deformation, high strain rate, transient phenomena, are in literature usually referred to as hydrocodes. Traditional numerical algorithms used in the hydrocodes to solve the partial differential equations governing the high-velocity impact phenomena commonly fall into two categories: Lagrangian and Eulerian. The basic difference between the two approaches is that in the Lagrangian codes the computational mesh is embedded in, and distorts with, the material; while in the Eulerian formulation the mesh is fixed. The Lagrangian codes are, in general, computationally more efficient than the Eulerian codes since they lack convective terms that represent the mass flow. The Lagrangian codes, unfortunately, have a tendency to lose accuracy with excessive mesh distortion. It is possible to use free Lagrangian methods to overcome the mesh-distortion problems (Fritts et al., 1983; Belytschko et al., 1994). The Eulerian codes can handle large deformations without difficulties but they present unique problems such as the tracking of the material interfaces in the case when more than one material is involved in the deformation process. Additionally, they have a more limited spatial resolution. The hybrid methods are developed to combine the advantages of both, Lagrangian and Eulerian, approaches (Benson, 1992). The major disadvantage of the hybrid codes is that they are not very adaptable. Consequently, a new code has to be developed for every particular application.

Although the use of standard numerical algorithms may provide accurate solutions to many complex problems their unquestionable merit can be overshadowed by certain difficulties. First, it cannot be overemphasized that the utility of numerical methods is limited by the required type of material description, including failure behavior, embodied in the traditional (deterministic) constitutive equations. Secondly, the computational approach can be very time-consuming for a number of reasons: large deformation gradients require sophisticated adaptive meshing schemes, and the fracture processes impose serious difficulties related to the frictional effects, tracking

of material interfaces, and preventing the element "overlaps". As emphasized by Zukas (1982) a "...fairly complex logic is required to define behavior at material interfaces...(and)...a price is paid in the number of additional computations required per cycle, thus slowing overall run time." Difficulties related to the propagation of shock waves require application of an extremely complex and computationally intensive technique commonly known as "shock fitting", or introduction of artificial parameters (e.g., artificial viscosity) into the governing equations (Zukas, 1992).

In the last three decades two alternative numerical approaches based on simulations of discrete systems, namely the molecular dynamics (including particle dynamics offshot) and smooth particle hydrodynamics, gained popularity in the impact and shock physics communities (e.g., Stellinwerf, 1990; Trent and Margolin, 1995). Both methods are still developing rapidly, as far as the application in the field of mechanics is concerned. The smooth particle hydrodynamics (smooth particle applied mechanics) is a three-dimensional free Lagrangian algorithm custom made to study the large deformation problems and transient phenomena. It is completely grid-free, thus, insensitive to the mesh distortion problems that impair the traditional Lagrangian codes. In this approach a continuum is approximated by a "cloud of particles" (Fritts et al., 1983) that moves according to the conservation laws of mechanics. The material properties are introduced by means of conventional constitutive relations (Monaghan, 1988). The method is simple, robust and flexible. The extension of an existing code to a different physical problems requires only a relatively straightforward addition of new features (Stellinwerf, 1990). In last couple of years the method matured enough to be included in commercial multiphysics simulation software packages such as LS-DYNA® (Livermore Software Technology Corporation).

A more detailed account of molecular dynamics is left for Section 2.1. Briefly, it deals with an ensemble of atoms (or molecules) arranged in a particular order (network or lattice). The interaction of atoms is, in the conventional approach, defined by the selected empirical interatomic potentials and the evolution of the discrete system is completely defined by Newton's equations of motion. The main advantage of molecular dynamics over the conventional numerical methods and continuum based theories is that it provides a detailed dynamic picture of the involved discrete atomic and nonlinear processes (Sutton and Pethica, 1990). It is generally accepted that atomistic analyses provide useful insights into the phenomena controlled by the discrete lattice defects. The thorough understanding of the underlying atomistics leads to a rational constitutive description of material behavior. The shortcomings are the small spacio-tempotal scales achievable at present and the "data glut." The major obstacle for the wider application of molecular dynamics in engineering solid mechanics is that it requires a homogenization (coarse graining) over many length

scales to provide parameters that enter the continuum models. To overcome this difficulty with available hardware, it is necessary to resort to either a hybrid approach that combine the finite-element and atomistic methods (Cundall and Strack, 1979, Ortiz, 1996; Tadmor et al., 1996) or one of the alternative discrete models (Trent and Margolin, 1995; Jirasek and Bazant, 1995).

The virtual laboratory provides powerful tools of analysis on the scale of crystal lattice. However, despite the advent of high performance computers, the hardware still imposes severe limits on the size of systems and duration of events that can be studied by purely atomistic models. Fortunately, in many physical phenomena of interest, such as for instance nanoindentation or crack growth, the vast majority of the material "deforms smoothly and closely obeys continuum elasticity" (Ortiz, 1996). Hence, the large-scale atomistic simulations are not necessary. Instead, it is more rational to resort to simulation models combining the finite elements continuum mesh and the discrete atomistic lattice. An inherent difficulty of these mixed models is the adequate treatment of the transition between the lattice and continuum (Kohlhoff et al., 1991; Mesarovic and Padbidri, 2005). Nonetheless, a quasicontinuum approach, proposed by Tadmor et al. (1996a, b), exploits the advantages of both atomistic and continuum theories in a natural and sophisticated way. This method permits the explicit treatment of multiple scales "by utilizing direct atomistic calculations as the source of the constitutive input used in the finite elements analysis" (Tadmor et al., 1996b) coupled with a traditional adaptive re-meshing. Nonetheless, this promising method still suffers from problems inherent to the finite-elements analysis. The most prominent one is the time consuming re-meshing technique that must be continuously performed to keep the computation and results objective (mesh-independent). The method is still not applied on dynamics problems because of the unresolved difficulties concerning the introduction of a time scale. Regardless of that, it should be noted that the mixed models based on "simple patching of unrelated lattice and continuum models" (Tadmor et al., 1996) are ill suited to deal with physical phenomena that are characterized by a relatively spread zone of extensive deformation and fracture. Further discussion of these hybrid simulation schemes is beyond the scope of this study.

An alternative strategy, advocated herein, is to use the molecular dynamics to provide understanding of macroscopic behavior in microscopic terms. The insights from atomistic simulations may be utilized to infer the constitutive equations that can be embodied into particle dynamics models through the process of homogenization (Krajcinovic and Mastilovic, 2000). Within the framework of particle dynamics, continuum is discretized into a set of "continuum particles" (Weiner, 1983) arranged in a lattice. Each continuum particle describes a system on the microscale (Vujosevic, 1996). The resolution length of this meso-scale model is equal to the mean distance

between the neighboring particles. All interactions and defects on smaller scales are taken into account indirectly through the bond properties and lattice statistics. The ultimate goal of the particle dynamics approach is to provide universal trends that can be used in analytical or numerical modeling of a continua on the macroscopic scale.

1.3.2 Summary

Neither of the outlined methodological approaches (empirical, analytical, numerical) can provide all desired information related to the complex physics of high strain rate loading of brittle materials. Hence, a clever combination of all three procedures seems to be the most reasonable approach. The success of this strategy depends largely upon the understanding of the physical underpinning of the penetration phenomena reflected in the wave propagation, microcracking, and effects of inertia. A thorough comprehension of the material behavior under high strain rate loading is another prerequisite for successful modeling. The last requirement is especially important since some of the processes that occur in solids subjected to rapidly changing loads are significantly different from similar processes that take place under static or quasi-static conditions. For instance, in a majority of cases that are important in engineering applications the target material in the neighborhood of the projectile tip is not statistically homogeneous on a small enough scale. In fact, as previously discussed, the material near the projectile tip is transformed by the extreme imparted energy. The transformation process belongs to the class of non-equilibrium thermodynamic processes that cannot be approximated by the methods of thermodynamics with internal variables. Hence, the continuum concepts such as stress, strain and even temperature are, rigorously speaking, not applicable. It seems, therefore, that the objective of analytical models must be reduced to the estimates of the global parameters such as penetration depth. However, to estimate penetration depth analytically it is necessary to infer the major trends of deformation and damage evolution. An attempt to formulate the constitutive description of the target and projectile materials will by necessity relate volume averages of stress, strain and temperature fields. Large scatter of local values of these fields is a moot point since they cannot be measured and will change from one physical realization to the other in the absence of ergodicity. However, if the objective of the analytical model is to identify material and structural parameters of the model on the macroscopic scale the local fluctuations of the parameters of state (σ, ε, T) may, indeed, found to be irrelevant. This conclusion is supported by a surprisingly robust dependence of the penetration depth on the impact velocity evidenced in tests.

CHAPTER 2

NUMERICAL SIMULATION TECHNIQUES

On the atomic (nano) scale a solid is a large ensemble of "initially isolated atoms...gradually brought together from infinity until the actual interatomic spacing of the solid is attained" (Zallen, 1983). Molecular dynamics is the most important numerical simulation technique to study the spatio-temporal evolution of such discrete systems at spatial and temporal scales that go beyond the current experimental limits. Except for the thermal vibrations about their equilibrium state, atoms of a solid body are “immobilized” (for example, in a crystal lattice) by interactions with their neighbors. Larger scale translations of atoms in solids are associated with inelastic phenomena such as inelastic flow and fracturing. The chemical composition, topology and geometry of atomic arrangements characterize nano-structure of a solid. A certain level of disorder of these three nano-structural aspects is inevitable in engineering materials. Typical defects on this scale are dislocations, vacancies, interstitials, substitute atoms, and disclinations. The static properties of crystals with a perfectly periodic structure are available in many sources going back to Love (1927).

Particle dynamics simulations can be classified with respect to the lattice morphology and type of links. The central-force (truss-type) lattice, formed by nonlinear springs that can transmit only the axial forces whose magnitude depend only on the interatomic distance, is the simplest. More elaborate links (Born and Huang, 1954) can carry shear force (simulating granular flow, Jenkins, 1988; Goddard, 1990; Jagota and Scherer, 1993) and/or axial force and bending moments (simulating crack propagation in concrete, Schlangen and van Mier, 1992; and hydraulic fracture, Tzschichholz et al., 1994). The popularity of complex lattices is often traced to the large number of model parameters that make fitting of test data much easier. The identification of these parameters and their relation to measurable continuum parameters is often not possible. One of the objectives of this study is to demonstrate that particle dynamics simulations can be used to determine changes of thermodynamic states during a non-uniform, non-equilibrium deformation process.

Computer simulations are the most natural and effective method used to study the dynamics of discrete element systems. Only a small fraction of the growing volume of literature that is of direct utility in the problems considered in this study are referenced herein.

2.1 MOLECULAR DYNAMICS

This brief overview is intended to present, albeit often quite superficially, some basics of the molecular dynamics that are actually applied in the presented simulations. No attempt is made to introduce the advanced molecular dynamics topics such as, for instance, non-equilibrium simulations or parallel algorithms, although they lean quite naturally on the subject area of interest. The first paper reporting the molecular dynamics simulation of atomic motion, Alder and Wainwright (1957), appeared more than a half of century ago. Hence, it is not surprising that an interested reader should have at his disposal many excellent treatises devoted to the computer simulations in condensed matter physics (e.g., Allen and Tildesley, 1987; Hoover, 1986; Haule, 1992; Rapaport, 1995; Ercolessi, 1997).

The molecular dynamics is a numerical simulation branch of statistical mechanics frequently applied in physics and chemistry to analyze motion of an ensemble[8] of atoms or molecules. The rigorous theoretical approach to these simulations, in which each atom interacts with all other atoms based on the quantum mechanics (so called, Car-Parrinello, or *ab initio*, molecular dynamics) leads to extremely intensive computations that limit the system size of the order of thousand atoms, which is extremely modest indeed compared to the 1-billion-atom simulations performed by Abraham and colleagues using the conventional molecular dynamics (Cox, 2005). The scope of the present overview is limited to the traditional molecular dynamics in which the motion (location and momentum) of each atom is defined by Newton's second law and appropriate sets of initial and boundary conditions. Therefore, in contrast to Monte Carlo method, the motion of each atom and each ensemble (i.e. each physical realization of some disorder) is deterministic. The statistically representative

[8] An ensemble is a collection of a large number of identical systems evolving in time under the same macroscopic conditions but different microscopic initial conditions. However, more often than not, we do not use the actual ensemble to perform experiments, but, by the virtue of the ergodic hypothesis, observe one particle system over some period of time (Krajcinovic and Rinaldi, 2005).

sample of physical realizations will, finally, provide a rational insight into the manner in which the disorder of the system affects the system response under considered set of circumstances and ambient effects (loads, temperature, etc.).

A discrete system (ensemble) consists of N atoms (or moleculs) of known masses m_i, and positions $\vec{r}_i \,(i = 1,...,N)$.[9] It is also assumed that the original stress-free state is known. The masses of the system interact according to the empirical interatomic force law or, equivalently, a potential energy function

$$\mathfrak{E}_{\mathrm{P}} = \mathfrak{E}_{\mathrm{P}}(\vec{r}_1,...,\vec{r}_N) = \sum_i \mathfrak{E}_{\mathrm{P1}}(\vec{r}_i) + \sum_i \sum_{j>i} \mathfrak{E}_{\mathrm{P2}}(\vec{r}_i,\vec{r}_j) + \sum_i \sum_{j>i} \sum_{k>j>i} \mathfrak{E}_{\mathrm{P3}}(\vec{r}_1,...,\vec{r}_N) + ... \qquad (2.1a)$$

where the first term represents the external fields; the second, pairwise interactions; the third, three-body interactions (extremely computationally expensive). In most simulations the rigor is relaxed by assuming that each atom interacts only with a rather small number of its nearest neighbors (so called, the first-nearest, the second-nearest, etc., approximations). The nearest-neighbors approximation is based on the primacy of the short-range order (Zallen, 1983), and motivated by straightforward crack definition and tremendous computational savings (of solving O(N) rather than O(N^p) problem, where N is the number of particles in the system, and $p \geq 2$ the interaction range parameter). Ignoring further the three-body interactions the potential energy of the system can be approximated by the sum of isolated empirical pair potentials (pairwise additivity assumption),

$$\mathfrak{E}_{\mathrm{P}} = \frac{1}{2} \sum_i \sum_j \phi(r_{ij}) \qquad (2.1b)$$

where ϕ is an interatomic potential, and $r_{ij} = |\vec{r}_{ij}| = |\vec{r}_i - \vec{r}_j|$ the distance between linked atoms i and j. Obviously, the concept of additive pair interactions (2.1b) is a far reaching simplification. For some crystal lattices two-body interactions cannot account for an appreciable fraction of the cohesive energy (Born and Huang, 1956).

---

[9] To avoid confusion it seems necessary to clarify the notation used in this section. The lower-case alphabetic indices (i, j) refer to the particular nodes of the lattice, while the lower-case Greek letter subscripts $(\alpha, \beta, \gamma, \delta)$ are reserved for tensor components. For instance, $\vec{r}_i$ is position vector of particle i with components $(r_i)_\alpha, (\alpha = 1,2)$, T_i refers to the temperature computed over the averaging area centered at node i, while $\vec{F}_{ij}$ designates the force between particles i and j with components $(F_{ij})_\alpha$, $(\alpha = 1,2)$.

Moreover, interaction in ionic crystals may occur due to the polarization effects, attributed to the electric fields of surrounding ions, that cannot be described by simple pair potentials. Nonetheless, the principal interactions in ionic and van der Waals lattices are essentially pairwise (Born and Huang, 1956). More general forms of the system potential energy can be used, if necessary, at the expense of computation time. As a consequence of the selection of the central force potentials, the potential energy, $\in_P$, depends only of the position of atoms $\vec{r}_i \,(i = 1,..., N)$, and the total energy of the system $\in$ (as determined by the solution of the system of differential equations) is conserved during the motion. In the language of statistical physics, the conventional molecular dynamics generates a microcanonical (Ω, $\in$, N) ensemble (Reif, 1965; Hoover, 1991).

The system of N Newton's differential equations of motion of this ensemble of particles

$$m_i \ddot{\vec{r}}_i = \vec{F}_i = \sum_{j \neq i} \frac{1}{r_{ij}} \frac{d\phi}{dr_{ij}} \vec{r}_{ij} \tag{2.2}$$

is usually approximated by corresponding finite difference equations and subsequently solved using one of many available algorithms. In addition to being accurate, the integration method should be fast and require little memory, permit the use of long timestep, and be easy to implement. Several different methods are at our disposal for this purpose. Although few more powerful procedures are available for integrating the finite difference equations, the Verlet algorithm is still the most widely used one (Allen and Tildesley, 1987). The Verlet method seems to be most efficient in terms of the computation cost and the most convenient for our modest computer facilities. According to this method the positions, velocities and accelerations at time $(t + \delta t)$ are computed directly by solving the second-order equations (2.2) knowing the current positions $\vec{r}(t)$, accelerations $\ddot{\vec{r}}(t)$, and the positions $\vec{r}(t - \delta t)$ of all particles of the system in the previous time. The time-reversible equation for advancing the position has a form

$$\vec{r}_i(t + \delta t) = 2\vec{r}_i(t) - \vec{r}_i(t - \delta t) + \delta t^2 \sum_{j \neq i} \frac{\vec{F}_{ij}(\vec{r}_i, \vec{r}_j)}{m_i} \tag{2.3}$$

where m_i is mass of the i-th atom and δt computational time step. This integration method is very compact and easy to implement. Since no dissipative forces act among the atoms, the interatomic forces are conservative. Therefore, the force exerted on the

i-th atom by the *j*-th atom is $\vec{F}_{ij} = -\vec{\nabla}_i \phi(\vec{r}_{ij})$ (2.2), and its calculation is by far the most computationally expensive part of the molecular dynamics simulation. The major disadvantages of the Verlet algorithm are the awkward handling of velocities, $\vec{v}_i(t) = [\vec{r}_i(t+\delta t) - \vec{r}_i(t-\delta t)]/2\delta t$ (advanced calculation of $\vec{r}_i$), and potential sensitivity to truncation error. Other integration methods (Stoermer, the half-step "leap-frog", Gear predictor-corrector, and Beeman algorithm) are also used in the simulation reported in this study.

The Stoermer algorithm (Allen and Tildesley, 1987) is a modification of the Verlet algorithm with numerical benefits that stem from the fact that at no stage the difference of two large numbers are taken to obtain a small number. The form is

$$\vec{r}_i(t+\delta t) = \vec{r}_i(t) + \delta t\, \vec{v}_i\left(t + \delta t/2\right) \tag{2.4}$$

In addition to the current positions and accelerations the stored quantities include mid-step velocities $\vec{v}_i(t+\delta t/2) = \vec{v}_i(t-\delta t/2) + \delta t\, \vec{a}_i(t)$; see also (2.19).

The time necessary to evaluate the interactions among all *N* atoms within the ensemble using algorithm (2.3) is proportional to N^2 (Allen and Tildesley, 1987). To improve the speed of program execution it is very useful to maintain a list of neighbors for each atom. The list of neighbors for *i*-th atom is formed by including all surrounding atoms within an extended cut-off distance. Between the periodical updates of the neighbors list (typically, a few time steps) the program does not check all others atoms in the ensemble but only those appearing in the list.

Furthermore, in the simulations presented in this study, the atomic interactions are limited, almost exclusively, to the first-nearest neighbors. In general, the short-range approximation is due to two major reasons: (*i*) the electronic screening effectively limits the range of interatomic forces, and (*ii*) the long-range interactions (e.g., Coulombic interactions in ionic solids) are prohibitively computationally expensive for large discrete systems. Consequently, the common approach in classical molecular dynamics is to use the short-range interactions (Haule, 1992).

2.1.1. Empirical Interatomic Potentials

In the molecular dynamics, atoms interact with each other. These interactions cause atomic motions by initiatiating interatomic forces that act upon atoms. The resulting change of interatomic distances, in turn, affects the forces. The role of interatomic forces is, therefore, pivotal for the realistic capturing of the simulated physical event.

Thus, the simulation is realistic only to the extent that the interatomic forces are similar to those operating between real atoms arranged in the same configuration (Ercolessi, 1997). As already mentioned, atomic bonding can be simulated with either quantum mechanics (*ab initio*) or empirical (conventional) models. The interatomic forces are, from the rigorous point of view, quantum mechanical in nature, but despite the advent of high performance computers there are few meso-scale phenomena that can be treated with the *ab initio* simulations. As described previously, interatomic forces are usually obtained as gradients of interatomic potentials depending on atomic configurations (which in the simplest case of the first-neighbor pairwise interactions reduces to the mutual distance from the nearest neighbors). Consequently, the interatomic potentials are the main ingredients in molecular dynamics simulations, and since *ab initio* molecular dynamics is beyond the scope of the present study the attention is focused exclusively on empirical interatomic potentials (consequently, the adjective "empirical" is ommited for brevity henceforth).

In molecular dynamics simulations the interatomic potential must be inferred or selected *a priory*. The construction of an interatomic potential is more of an art than a science, but on the user end the selection is nowadays made more straighforward by the wide variety of existing literature. The choice of the interatomic potential is crucial for at least two reasons: (*i*) the accuracy of the potential dictates the quality of the simulation results, (*ii*) its complexity determines the efficiency of the code in the terms of the computational time. Although some compact pair potentials may ultimately appear to be inadequate, many fundamental, generic aspects of the physical phenomena may be observed by taking advantage of their simplicity.

The simplest potentials are the pairwise potentials in which the force between two atoms depends solely on their mutual distance. These potentials, strictly speaking, describe realistically only the noble gases that are characterized by spherical electron clouds that stick close to nuclei. The simplest possible among pairwise potentials is the hard-sphere potential that implies: (*i*) that no force occurs if the interatomic distance is larger then some characteristic value and (*ii*) that at or below that threshold the interactive force exerted on both particles is infinite.

More realistic interatomic interactions are obtained assuming that the interactive force varies smoothly from being strongly repulsive at small distances to becoming attractive at intermediate separation and finally asymptotically converge to zero as the distance between two interactive masses increases (so called, cut-off distance). The best known potential of this type that is standardly used when the research focus is on the fundamental, rather than specific, issues is the Lennard-Jones 6-12 potential, originally developed for noble gasses with van der Waals-type cohesion (Lennard-Jones and Devonshire, 1939). The general form of this potential is

$$\phi\left(\bar{r}_{ij}\right) = -\varepsilon_{LJ}\left[2\left(\frac{1}{\bar{r}_{ij}}\right)^{6} - \left(\frac{1}{\bar{r}_{ij}}\right)^{12}\right] \tag{2.5}$$

where ε_{LJ} is the depth of potential well, and $\bar{r}_{ij} = \left(r/r_0\right)_{ij}$ ratio between the current and the equilibrium inter-atomic distance. The parameters ε_{LJ} and r_0 are selected with desire to fit optimally the most desired physical properties of the material. The amount of work performed on Lennard-Jones systems since the birth of molecular dynamics is unsurpassed by any other, and for that reason, if no other, the importance of this potential could not be overemphasized.

The term $\bar{r}_{ij}^{-12}$ in (2.5), dominating the atomic repulsion, is selected for convenience: on physical grounds the exponential term is a more appropriate choice. The simplest pairwise potential that accounts for this is the Morse potential

$$\phi\left(\bar{r}_{ij}\right) = \varepsilon_M\left\{\exp\left[-2\alpha_M\left(\frac{1}{\bar{r}_{ij}} - 1\right)\right] - 2\exp\left[-\alpha_M\left(\frac{1}{\bar{r}_{ij}} - 1\right)\right]\right\} \tag{2.6}$$

The adjustable parameter α_M defines the slope of the repulsive wall. The parameters like ε_M, r_0 and α_M are again commonly determined by fitting the material properties that are most relevant for the problem at hand.

Some pair potentials were constructed with a narrow goal of capturing the repulsive interaction between particles, while the attractive part may be described by some other type of interaction. A very useful potential, belonging to this class, is the Born-Mayer potential developed to represent the salient features of closed-shell repulsion between ions in ionic crystals characteristic of ceramic materials. The functional form of this potential is

$$\phi\left(r_{ij}\right) = A_b \exp\left(-B_b\, r_{ij}\right) \tag{2.7}$$

where A_b and B_b are fitting parameters. Although the inverse power form of interatomic potential (2.5) is the most widely used in heuristic studies, the results of quantum-mechanical calculation, as already mentioned, favor the exponential form.

The fundamental purpose of any interatomic potential is to capture correctly the most prominent characteristics of the atomic bonds. Therefore, one should always keep in mind that the pairwise potentials “were originally developed to describe

atomic interactions in systems in which these potential forms are physically justified" (Vitek, 1996) and resist temptation to use them indiscriminately to benefit from their simplicity. These simplistic potentials cannot accurately describe interatomic interactions in more complicated systems such as, for example, the strongly covalent systems (e.g., SiC), the most ceramic materials characterized by the closed-shell systems, or the metals characterized by delocalized "electron sea." Nonetheless, the pairwise potentials were almost exclusively used from the 1950's to the 1980's. Afterward, a host of different potentials have been constructed with the intention to account for the most important features of material behavior while keeping the functional form of potential as simple as possible. For example, in metals all electrons are not localized in a spherical clouds around the nuclei and the valence electrons are often shared among many ions. Consequently, the force exerted on an atom depends not only on the distance separating it from neighbor(s) but also on the local atomic density. In other words, forces between ions are many-body in character, rather than simply being pairwise additive, reflecting the weakening of the interatomic bond in "crowded environment." The focus is usually on the attractive part of the potential. Consequently, so called, embedded atom potential is developed based on the effective medium description to approximate the interactions between ions in metals. The general form of this potential is

$$\phi\left(\vec{r}_{ij},\rho_i\right)=\sum_i\left[\frac{1}{2}\sum_{j\neq i}\varphi\left(\vec{r}_{ij}\right)+\psi\left(\rho_i\right)\right] \tag{2.8}$$

where φ is the pairwise term depending only on the atomic separation while ψ is density-dependent contribution (the embedding energy necessary to insert i-th atom into the background electron density ρ_i). The many-body contributions reflect the nonlinearity of the density-dependent term. The differences between the pairwise and many-body potentials are examined in detail (see for instance, Holian et al., 1991).

Another many-body potential that is of particular interest for modeling of semiconductor materials (such as SiC) is the Tersoff potential (Tersoff, 1988). This interatomic potential is taken to have the general form

$$\phi=\frac{1}{2}\sum f_C\left(r_{ij}\right)\left[a_{ij}f_R\left(r_{ij}\right)+b_{ij}f_A\left(r_{ij}\right)\right]. \tag{2.9}$$

The term f_C is the smooth cutoff function, while the functions f_R and f_A, which represent the repulsive and attractive pair potentials, can be chosen to have an exponential form (following the Morse potential).

Further discussion of the benefits and advantages of potentials and their functional form are beyond the scope of this brief introduction; they can be found in the literature (Tersoff, 1988; Vitek, 1996; and many others). However, it seems appropriate to end this brief overview by adding that in neverending struggle between the more sophisticated and the more spacial discrete models, under the given computer performance constraints, the latter is still considered more important to the meaningfulness of results. In other words, it is generally accepted that for fracture simulations it is more advantegous to increase the size of the discrete system and simplify the potential, than to do the opposite.

2.1.2 Stress and Stiffness Tensors

Strictly speaking the discrete system parameters of state can be related to the continuum concepts of stiffness, stress, temperature, and damage only when the thermodynamic system is: (*i*) large enough to be statistically homogeneous, and (*ii*) either in equilibrium or close to it (measured by Deborah number; Section 1.1). If there requirements are not fulfilled the meaning of the continuum concepts becomes uncertain.

The general expression for the stress tensor at a given particle in a system of interacting particles in an equilibrium state ($\mathfrak{E} = \mathfrak{E}_P$) can be obtained by expanding the total energy of the system (2.1b) into a Taylor series (Hoover, 1985). The linear term in the series represents the stress tensor. If the interaction of a system of atoms can be approximated by a central force potential $\phi = \phi(r_{ij})$, the $\alpha\beta$ component of the stress tensor acting on the *i*-th atom has the following form

$$(\sigma_i)_{\alpha\beta} = \frac{1}{2\Omega} \sum_{\substack{i,j \\ j \neq i}} \frac{d\phi}{dr_{ij}} \frac{(r_{ij})_\alpha (r_{ij})_\beta}{|r_{ij}|} \tag{2.10}$$

where Ω is a volume (area), and $(r_{ij})_\alpha$ and $(r_{ij})_\beta$ the α and β components of the vector r_{ij}, respectively (Born and Huang, 1956; Vitek, 1996). The Cauchy stress defined by (2.10) depends only on interatomic forces proving that as a measure of internal system interaction it is independent of kinetic energy and mass transfer (Zhou, 2003). It is important to recognize that since the stress given by (2.10) is defined with respect to the static (quasi-static) equilibrium state, $\mathfrak{E}_P = \mathfrak{E}_P$ ($\mathfrak{E}_P \approx \mathfrak{E}_P$), the resultant force $\vec{F}_i = (1/2)\sum(\partial\phi/\partial r_{ij})(\vec{r}_{ij}/|\vec{r}_{ij}|)$ acting on each atom *i* is (close to) zero. On the other

hand, the dynamic deformation involves wave propagation, and in order to use expression (2.10) it has to be tacitly assumed that the non-equilibrium process can be represented as a sequence of equilibrium states, which is a concept commonly used in the non-equilibrium thermodynamics.

The quadratic term in Taylor series for the total energy of the system defines the elastic stiffness tensor

$$\left(C_i\right)_{\alpha\beta\gamma\delta} = \frac{1}{2\Omega}\sum_{\substack{i,j \\ j\neq i}}\left(\frac{d^2\phi}{dr_{ij}^2} - \frac{1}{r_{ij}}\frac{d\phi}{dr_{ij}}\right)\frac{\left(r_{ij}\right)_\alpha\left(r_{ij}\right)_\beta\left(r_{ij}\right)_\gamma\left(r_{ij}\right)_\delta}{\left|r_{ij}\right|^2} \tag{2.11}$$

related to the area or volume centered on the *i*-th atom.

Finally, the two-dimensional triangular lattice is equivalent to three-dimensional continuum under a plane strain conditions (Monette and Anderson, 1994). Therefore, expressions for modulus of elasticity

$$E = \frac{C_{1212}\left(3\,C_{1111} - 4\,C_{1212}\right)}{\left(C_{1111} - C_{1212}\right)} \tag{2.12a}$$

and Poisson's ratio

$$\upsilon = \frac{\left(C_{1111} - 2\,C_{1212}\right)}{2\left(C_{1111} - C_{1212}\right)} \tag{2.12b}$$

of isotropic material in terms of two arbitrary components of the stiffness tensor can be derived by using appropriate plane strain relation (Appendix A). A comprehensive review of plane elasticity related to the lattice simulations in micromechanics is provided by Ostoja-Starzewsky (2002).

2.1.3 Temperature

The estimate of temperature fields in the course of dynamic events (from penetration processes to any macrocrack propagation) is of fundamental importance for the analysis and modelling. As discussed before, this estimate gives rise, unfortunately, to some basic questions related to the non-equilibrium thermodynamics concerning the fundamental thermodynamic (more accurately, thermostatic) concepts such as entropy and absolute temperature of the system that is not in equilibrium. Some non-equilibrium thermodynamic theories have postulated that classical thermostatics concepts have to be applied locally in inhomogeneous non-equilibrium situations since "no useful description of time-dependent nonequilibrium behavior is possible without some recipe for describing the instantaneous state of a system" (Hoover, 1985). Others, resorted to definition of the non-equilibrium entropy that is then used as a potential for derivation of a generalized temperature, which differs from the local equilibrium temperature (Jou and Casas-Vazques, 1992). As it was pointed out by Callen (1985) the non-equilibrium entropy definitions are dependent on uncertain premises. In the absence of consensus it seems prudent to use the standard, ideal-gas thermometer definition, familiar from the kinetic theory

$$T \equiv \frac{2}{3k_B}\left\langle \frac{mv^2}{2} \right\rangle \tag{2.13a}$$

which has the firm statistical-mechanics foundations since it follows from the canonical-ensemble maximum-probability distribution (Hoover, 1985; Wannier, 1987).

The expression (2.13a) tacitly assumes that the considered ensemble is canonical, the system is thermally equilibrated, and the particle velocities are distributed according to Maxwell-Boltzmann distribution (Chandler, 1987). Thus, the term "temperature," whenever used henceforth within the molecular dynamics framework, implies the "instantaneous kinetic temperature." Nonetheless, it should be kept in mind that "thermodynamic temperature ≡ long-time average of the instantaneous kinetic temperature at equilibrium" are the only rigorously defined equivalencies. Indeed, "in non-equilibrium situations, the instantaneous kinetic temperature is the only meaningful definition" (Holian et al., 1995). Be it as it may, the (instantaneous kinetic) temperature is defined (in two-dimensional space) as

$$T_i = \frac{m_i}{2N_i k_B} \sum_{j=1}^{N_i} \left(v_{xj}^2 + v_{yj}^2 \right) \tag{2.13b}$$

where m_i is the mass of an atom, N_i the number of atoms belonging to its averaging area, and k_B Boltzmann's constant. Also, v_x and v_y are the components of vibrational velocity (Fig. 2.1) that is obtained by subtracting the velocity of correlative motion ($\bar{v}$ - solid line) from the total particle velocity (v_T - dashed line)

$$v_\alpha = v_{T\alpha} - \bar{v}_\alpha \quad (\alpha = x, y) \tag{2.14}$$

The total velocity follows directly from the solution of Newton's equations of motion (2.2), while the velocity of correlative motion is obtained as the space average of the total velocities of all atoms belonging to a certain averaging area $\bar{v} = \langle v \rangle$.

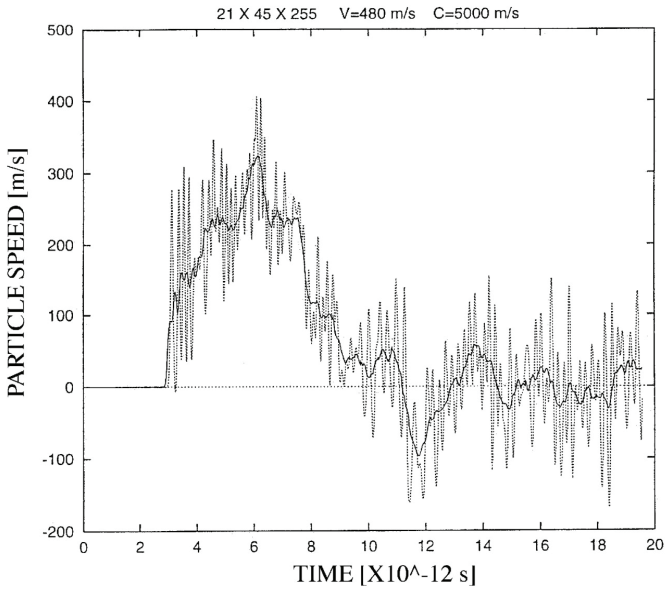

Fig. 2.1. Typical velocity pulse recorded during simulation of bar impact.

The instantaneous kinetic temperature, calculated by using expressions (2.13) and (2.14), is averaged in both time and space. The averaging area is commonly assumed to be the same circular region (shaded area in Fig. 2.2) that is used for calculation of the velocity of correlative motion (2.14). The each node in the lattice is, therefore, characterized by the averaging area of radius R_{av} centered at that node, and

corresponding velocity of correlative motion and temperature averaged within that region. The size of the averaging area is a result of a compromise between the contradicting requirements for as large as possible size of the statistical sample and as small as possible resolution length of the calculation (measurement). The choice of the size of averaging area for the purpose of present study is discussed in Section 3.1.4.

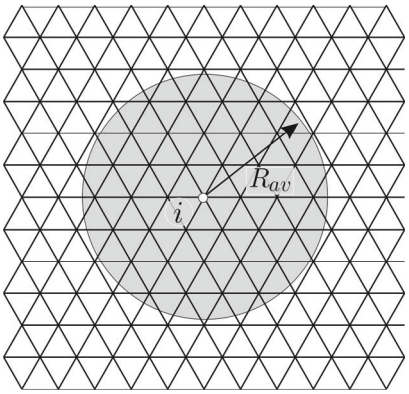

Fig. 2.2. The averaging area (generally, volume) for temperature evaluation in the molecular dynamics simulations.

2.1.4 Molecular Dynamics Simulation Cell

The molecular dynamics simulations that can be performed on standard workstations and desktop computers are limited to the systems consisting of a couple of million atoms; the molecular statics simulations (the molecular dynamics offshot characterized by the artificial damping and equilibration during every load-increment step) are, naturally, much more spatially limited. The response of such a relatively small system may be dominated by surface effects. The unwanted surface effects can be removed by using periodic boundary conditions whenever the properties of the bulk material are of interest (Born and von Karman, 1912). The volume of the periodic box (molecular dynamics cell) is representative of the bulk material in a sense that the bulk is considered to be composed of the periodic boxes surrounded on all sides by the exact replicas of itself (Allen and Tildesley, 1987). The removal of the undesired surface effects using these cells comes at the expense of ntroduction of the non-physical periodicity into the system of atoms. The drawbacks of include: (*i*) unrealisticly stiff response, (*ii*) non-physical wavelengths in the solution fields, and (*iii*) supression of localization that may otherwise occur (Mesarovic and Padbidri,

2005). Another artifact of periodic boundary conditions, the violation of the angular momentum conservation principle (Haule, 1992), is discussed in Appendix C.

In order to simulate the most general loading conditions it is necessary to be able to change the shape and size of the periodic box, and keep certain state parameters (for example temperature or pressure) constant. The restriction that the shape of the periodic cell has to be kept constant has an adverse effect on the applicability of the molecular dynamics cell. For example, the molecular dynamics cell simulations of a two-dimensional uniaxial test, using conventional algorithms can reproduce only a very restrictive, one-dimensional strain state. Several molecular dynamics methods were suggested as potential remedies in a series of papers (Parrinello and Rahman, 1982; Nose and Klein, 1983; Li and Johnson, 1992; Li and Johnson, 1993). According to them the shape of the periodic box is treated as being a phenomenological variable that can change with time.

In general three-dimensional case, the periodic box is parallelepiped, completely described by three vectors $\vec{a}, \vec{b}$ and $\vec{c}$, spanning the edges of the box, that can be of different lengths and arbitrary orientations. The positions and velocities of atoms in the periodic box are scaled by a matrix h in the following way: $\vec{r}_i = h\,\vec{s}_i$ and $\dot{\vec{r}}_i = h\,\dot{\vec{s}}_i$, where $h = \left\{\vec{a}, \vec{b}, \vec{c}\right\}$, and $\vec{s}_i = \{\xi_i, \eta_i, \zeta_i\}$ $\left(0 \le \xi_i, \eta_i, \zeta_i \le 1\right)$. To simplify the writing, the vector arrows will be omitted in the sequel of this section. The box dynamics is completely defined by Lagrangian in the form (Parrinello and Rahman, 1981)

$$\Lambda_{PR} = \frac{1}{2}\sum_{i=1}^{N} m_i\, \dot{s}_i^T M\, \dot{s}_i - \sum_{i=1}^{N}\sum_{j>1}^{N} \phi\left(r_{ij}\right) + \frac{1}{2} W\, Tr\left(\dot{h}^T \dot{h}\right) - p_e\, \Omega_b \tag{2.15}$$

where $M=h^T h$ is the metric tensor, p_e externally applied pressure (mean normal stress), Ω_b volume of the periodic box, and W fictitious mass whose physical meaning and proper choice are discussed in Section 2.1.6. The equations of motion for the time evolution of the particles and the periodic box can be derived from the Lagrangian (2.15) in the form

$$\ddot{s}_i = -\sum_{j \ne i} \frac{1}{m_i} \frac{1}{r_{ij}} \frac{\partial \phi\left(r_{ij}\right)}{\partial r_{ij}} \left(s_i - s_j\right) - M^{-1}\dot{M}\dot{s}_i \qquad \left(i = 1,\ldots,N\right) \tag{2.16}$$

$$W\ddot{h} = \left(\pi - p_e 1\right)\sigma - h\,\Sigma \tag{2.17}$$

where 1 is the unit matrix, and π internally generated pressure matrix that represents the system response to the applied stress *S*. The symmetric tensor Σ is related to the applied stress *S* and the equilibrium box configuration (the details are presented in the Appendix C). From (2.17) it follows that the dynamics of the periodic box is driven by the imbalance between the external and internal forces.

2.1.5 Nose-Hoover Thermostatted Molecular Dynamics

The importance of the constant temperature calculations, and the popularity that this topic enjoyed amongst the computational statistical mechanicians, resulted in an abundance of different algorithms. The Nose-Hoover themostatted molecular dynamics has its theoretical foundation on the classical thermodynamical concept of "connecting" the thermodynamic system (in this case a conventional molecular dynamics cell) to a thermal reservoir, which insures the constant temperature of the ensemble during a simulation (Hoover, 1985; Holian et al., 1995). Therefore, by definition, a given ensemble of particles is canonical (Ω, *T*, *N*), as opposed to the standard molecular dynamics that leads to the microcanonical (Ω, Є, *N*) ensemble. The Nose-Hoover model uses the classical concept of temperature (discussed in Section 2.1.3) being related to the instantaneous kinetic energy of the system. Thermostatting technique is based on the integral feedback type of atomic motion constraint. An additional acceleration term is inserted in Newton's equation of motion,

$$\ddot{\vec{r}}_i = \frac{\vec{F}_i}{m_i} - \vartheta_H \, \xi_H \, \dot{\vec{r}}_i \tag{2.18a}$$

The dynamic variable, ξ_H, must satisfy the additional equation of motion

$$\dot{\xi}_H = \vartheta_H \left(\frac{T}{T_0} - 1 \right) \tag{2.18b}$$

In (2.18) ϑ_H is the rate of particle coupling to the heat reservoir. The Newton's equation of motion (2.2) is recovered from (2.18a) for $\vartheta_H = 0$. The friction coefficient ξ_H (sometimes also called the heat-flow variable) keeps the long-time average of the kinetic energy constant, allowing, simultaneously, the fluctuations of the instantaneous kinetic energy.

In the present work the Nose-Hoover equations of motion are integrated using the method of Stoermer centered-differences (Holian et al., 1990) according to which

$$r(t) = r(t-\delta t) + \delta t\ \dot{r}(t-\delta t/2) + O\left(\delta t^3\right) \tag{2.19a}$$

$$\xi_H(t) = \xi_H(t-\delta t) + \nu\left[\frac{T(t-\delta t/2)}{T_0} - 1\right]\delta t + O\left(\delta t^3\right) \tag{2.19b}$$

$$\dot{r}(t+\delta t/2) = \frac{1}{1+\vartheta_H\,\xi_H(t)\delta t/2}\left\{\dot{r}(t-\delta t/2)\left[1-\frac{1}{2}\delta t\vartheta_H\xi_H(t)\right] + \frac{F(t)}{m}\delta t\right\} + O\left(\delta t^3\right) \tag{2.19c}$$

Detailed discussion of this method is presented by Holian et al. (1995).

2.2 PARTICLE DYNAMICS

The focus of the present overview of particle dynamics (also known as lattice or spring-network) model is on the techniques used throughout this particular study. An excellent, comprehensive review of the topic is presented by Ostoja-Starzewski (2002).

The transition from atomistic (nano) to micro and meso scales involves mapping of an ensemble of atoms onto a "continuum particle" (Weiner, 1983). The dynamics of atoms forming a morphologically perfect ensemble subjected to a uniform state of stress is completely deterministic. However, the material texture is actually random and the problem of dynamic loading of brittle materials is not deterministic but stochastic. The particle dynamics incorporates both variability and uncertainty in a straightforward manner. Variability, also termed randomness or aleatory variability, is the natural randomness in a process. Uncertainty, also termed epistemic uncertainty, is the uncertainty in the model; it is due to limited knowledge or data or both. The material texture (e.g., morphology of atoms, molecular chains, grains of various engineering materials) is an example of the aleatory variability. The disorder may be topological (unequal coordination number), geometrical (unequal length of bonds) or structural (unequal strength and stiffness of bonds). The disorder is further enhanced by damage evolution, which is governed (to an extent depending on the loading power) by the local fluctuations of the energy barriers quenched within the material and the local fluctuations of stress.

Hence, to describe the deformation of brittle solids with random microstructure it is necessary to introduce quenched disorder into the virtual experiment. The initial quenched disorder, frozen in the lattice, can be introduced in the form of the probability distributions of strengths, stiffnesses, and missing links. The disorder attributed to the applied loads and temperature should be determined by simulations and approximated analytically from the model. Due to the initial randomness of the microstructure the damage evolution is inherently stochastic.

In the present monograph the brittle continuum is approximated by a two-dimensional triangular lattice equivalent to a three-dimensional elastic continuum under a plane strain condition (Monette and Anderson, 1994) (see also Appendix A). The lattice is formed by inseparable "continuum particles", located in lattice nodes, interconnected by links that can transform only axial force. The link properties are approximated by a linear force-elongation relation in tension (Hookean potential for a perfectly brittle material), and a nonlinear force-elongation relation in compression. The later is inspired by Born-Meyer potential (2.5), which was originally developed to model closed-shell repulsion in ionic crystals (Born and Huang, 1956; Vitek, 1996). This force-elongation relation is introduced to capture several important features of the deformation process typical of the considered materials; namely, brittle behavior in tension, increase of shock wave velocity and the decrease of compressibility with increasing pressure. The repulsive (compressive) force, derived from this potential, is

$$F_{ij}^{R} = \frac{k_{ij}\lambda_{0ij}}{(B-2)}\left\{\exp\left[B\left(1-\left(\frac{\lambda}{\lambda_0}\right)_{ij}\right)\right]-\left(\frac{\lambda_0}{\lambda}\right)_{ij}^{2}\right\} \tag{2.20}$$

where λ_{0ij} and λ_{ij} are the initial and current distances separating interacting particles i and j, k_{ij} corresponding link stiffness, while the parameter B defines the slope (steepness) of the repulsive wall (Fig. 2.3) (Krajcinovic and Mastilovic, 1999). The interaction of particles is limited to the first-nearest neighbors.

The particle may represent a grain of ceramic, a concrete aggregate or a granule of clastic rock.[10] The average distance between two neighboring particles is, therefore, the model resolution length, and each particle is a representative of an ensemble of atoms. All features (defects) on the finer scale are smoothed out by selecting a proper

[10] The criteria for the selection of the optimal number of atoms forming a particle depend on the considered material and required resolution. For example, Kendall (1978) demonstrated analytically and experimentally that it is not possible to comminute by compression particles of polystyrene and coal smaller in diameter than approximately 5 mm. Therefore, a lattice formed by continuum particles of 5mm in diameter could approximate these materials.

distribution of link properties. As an example, the size of grains and strength of grain boundaries in a polycrystalline ceramics may vary substantially. The strength of a grain boundary is affected by residual stresses (Curtin and Scher, 1990), twist and tilt angles, dislocations, and other imperfections such as second-phase particles. All of these defects are randomly distributed. Similarly, the lattice representation may be useful for rocks comprised of relatively stiff grains joined by cementitious materials of variable, but inferior, stiffness into a composite of inferior tensile strength.

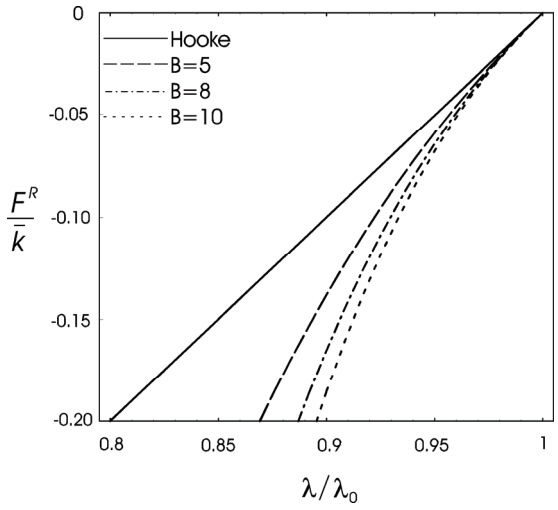

Fig. 2.3. Repulsive force vs. link compression for three repulsive wall parameters *B*.

The natural manner in which the random texture of the material, random location, sizes and shapes of microcracks, are modeled is a significant advantage of lattices (Krajcinovic and Mastilovic, 1999). The disorder can be either quenched (frozen into lattice) or annealed (attributed to external actions). In the pristine state all lattices in this study are topologically ordered by selecting the coordination number of all bulk-particles (except of those at lattice boundaries) to be equal six. The lattice is geometrically disordered since the equilibrium distances between particles (initial link lengths $\equiv\lambda_0$) are sampled from the normal distribution within the range $\alpha_l\bar{\lambda} \le \lambda_0 \le (2-\alpha_l)\bar{\lambda}$, (Fig. 2.4a). The geometrical-order parameter α_l, $(0 < \alpha_l \le 1)$, characterizes, for example, the distribution of grain sizes. If all grains are perfect hexagons $(\alpha_l = 1)$ the lattice is perfectly periodic triangular network (Fig. 2.5a). The lattice is also structurally disordered due to the random distribution of link strengths and stiffnesses. The link stiffnesses are uniformly distributed within the range $\beta_l\bar{k} \le k \le (2-\beta_l)\bar{k}$, (Fig. 2.4b), where the structural-disorder parameter β_l,

$(0 \le \beta_l \le 1)$, characterizes the stiffness distribution, and $\bar{k} = 8E_0/5\sqrt{3}$ mean link stiffness related to the modulus of elasticity of the pristine material, E_0 (Monette and Anderson, 1994).

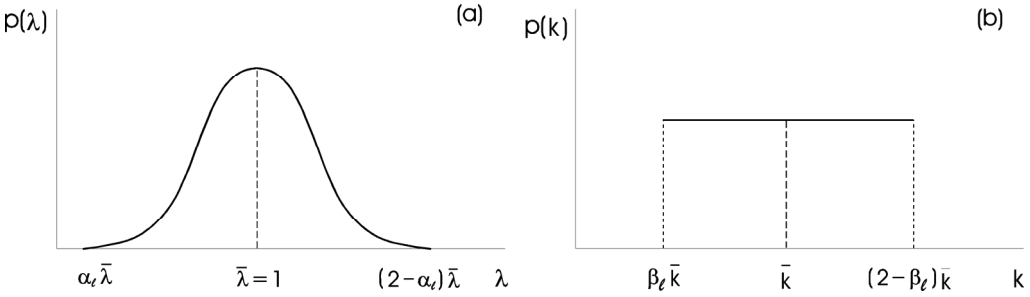

Fig. 2.4. Distribution of: (a) link lengths, and (b) link stiffnesses.

The link-rupture criterion is defined in terms of the critical link elongation, i.e. the link between particles *i* and *j* ruptures (as its force carrying capacity in tension is permanently lost) when the link elongation reaches the critical value $\varepsilon_{ij} = \Delta\lambda_{ij} / \lambda_{0ij} = \varepsilon_{cr} = const.$ The critical link elongation, ε_{cr}, is the model parameter related to the uniaxial tensile strength of the material.

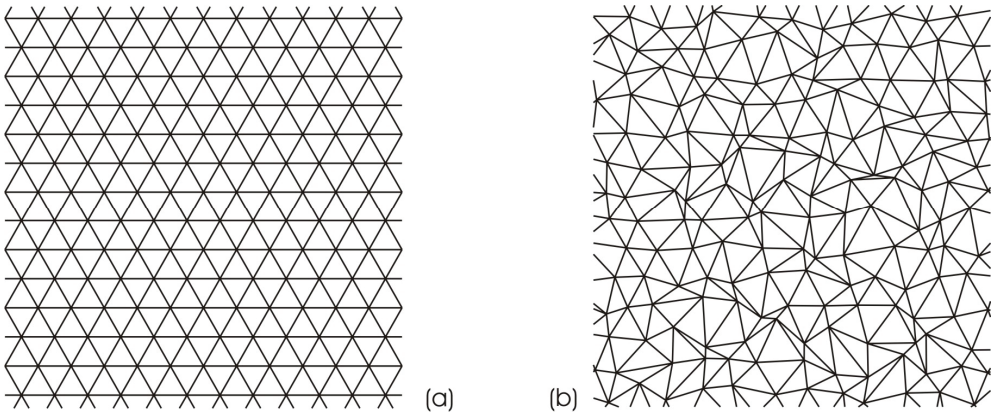

Fig. 2.5. Triangular lattice; (a) $\alpha_l = 1$, (b) $\alpha_l = 0.01$.

The selected model recognizes two different types of interaction between particles: chemical and mechanical (Mastilovic and Krajcinovic, 2005). The chemical interaction is both tensile and compressive, and is limited to the first-nearest neighbors. The mechanical interaction is strictly compressive, but the number of

involved particles is not limited. It can be established between particles that were either initially not connected or re-established between particles that were previously separated by the link rupture. In the former case the mechanical link is established when the initial distance between particles shrinks below the average link length $\bar{\lambda}$ (Fig. 2.6b). In the latter case the repulsive interaction is re-established when the distance between particles reduces to $\lambda_{ij} \leq \lambda_{0ij}$ (Fig. 2.6a).[11] The formation of the mechanical (repulsive) force between the particles that were not connected by cohesive forces is essential to model the flow of the comminuted phase.

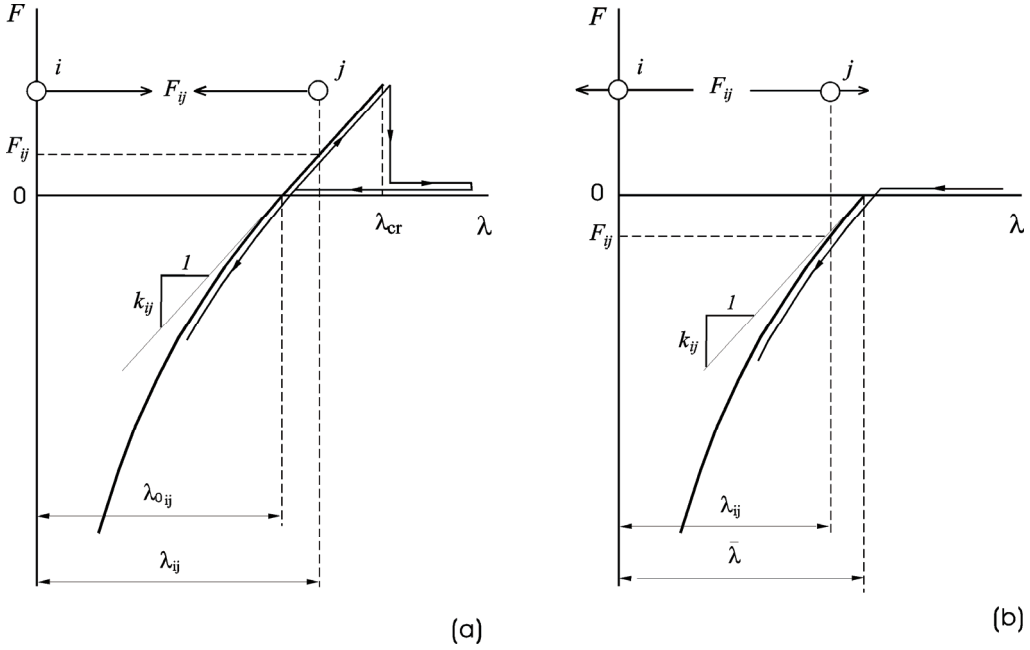

Fig. 2.6. Nonlinear relation between link force and elongation. Interaction between particles that (a) are or were originally the first-naerest neighbors (b) were not originally the first-nearest neighbors.

The adopted lattice can also be interpreted as being a Delaunay network dual to the Voronoi tessellation of grain boundaries of a ceramics (or the petrofabric of a rock or the aggregats of concrete, etc). In this case the strength and stiffness of a link is related to the corresponding properties of the grain boundary or cementitious binder. The link rupture is equivalent to the failure of the corresponding grain facet. The

[11] Preventing the transmission of tensile force by mechanical contact (Figure 2.6b) is tantamount to assuming that a ruptured bond cannot heal.

effect of residual stresses along the grain boundaries is reflected in the unequal tensile strengths and stiffnesses of links (Krajcinovic, 1996; Raiser et al., 1990). The microcracks smaller than the grain boundary are introduced through the link strength distribution. Since the resolution length is equal to the grain facet the growth of these microcracks from their initial length to the length of the grain boundary facet is assumed to be instantaneous.

CHAPTER 3

NUMERICAL SIMULATIONS

The molecular and particle dynamics simulation techniques described in Chapter 2 matured over the last two-three decades into useful solid mechanics tools. Despite a growing consensus that these numerical simulation methods provide reasonable estimates of deformation trends and damage evolution modes on their spatial scales it is often considered that the agreement between the virtual and the actual laboratory experimental data is primarily qualitative in nature. However, the simulation results must agree quantitatively with the measurements data recorded in simple experiments in order for these numerical simulations to be useful for formulation of analytical models and, ultimately, to become engineering design tools. Many simulations presented in this review were performed in the early 1990's when these two numerical techniques, especially the particle dynamics, were relatively novel in solid mechanics. Therefore, to gain confidence in the proposed approach it was considered necessary to simulate:

(*i*) Taylor (rigid anvil) test,
(*ii*) Planar (plate) impact test, and
(*iii*) Tension (quasi-static and dynamic) test

which are traditionally used in impact and penetration mechanics. These three tests are also useful to illustrate, for epistemic reasons, the main features of dynamic behavior of materials, which distinguish this field from classical solid mechanics. Finally, the simulation of the cylindrical cavity expansion was perfomed to provide a pathway for analytic modelling by identifying parameters governing of the target resistance during the high-velocity penetration.

Thus, the initial scope of these simulations was unpretentiously limited to capturing the most dominant features of enumerated phenomena, such as the damage evolution pattern and the velocity and stress profiles for dynamic experiments (*i, ii*) or the fracture pattern and the form of the stress-strain relationship in the case of the quasi-static and dynamic test (*iii*). Having in mind the simplicity of the selected models (reflected by relatively small samples, pairwise interatomic potentials, and

first-nearest neighbors approximation), the qualitative agreement with actual experimental data was very encouraging. Consequently, it was deemed appropriate to establish the quantitative relation between the simulation data and the traditional material properties such as modulus of elasticity and the velocity of elastic longitudinal wave propagation. A satisfactory match between the results of the analytical and molecular dynamics (computational) models provides both the confidence in and justification for the proposed computational method formulated and described in Chapter 2.

Additionally, the three virtual tests were also necessary as an assurance that the expressions used to define the components of the stress (2.10) and stiffness (2.11) tensors, which are rigorous only for the equilibrium thermodynamic process and in the limit of small strain rates (Vitek, 1996), provide meaningfull results compared to available experimental data. Furthermore, the determination of field properties is somewhat ambiguous due to the fact that the size of the averaging area is a compromise between the conflicting requests for the statistically meaningful sample size and the small (fine) model resolution. This compromise requires careful examinations of the data collected in the close neighborhood of discontinuity fronts. Last but not least, the presented simulations, in their various modifications, are requisite for the identification of model parameters for the pivotal cavity-expansion simulation (Section 3.4).

3.1 TAYLOR (RIGID-ANVIL) TEST

The idea of using the impact of a flat-ended projectile on a “rigid” target for the analysis of deformation at high strain rates, was originated by Taylor (1947). From then on, this classic test has become a standard procedure for the verification of the constitutive behavior of materials (Meyers, 1994) since it provides a wide range of inelastic strains and strain rates.

The molecular dynamics simulations of this study were performed on the samples of Lennard-Jones two-dimensional solid, varying in size from 2000 to 60000 atoms. The reduced (non-dimensional) form[12] of the interatomic potential parameters (2.4), $\varepsilon_{LJ} = 1$ and $r_0 = 1$, and the unit mass are used throughout this study, unless specified otherwise. The initial estimate of the non-dimensional computational time step was based on the approximate expression commonly used for the simulations on two-

[12] The non-dimensional (reduced) units are discussed at length by Allen and Tildesley (1987).

dimensional ensembles of particles interacting according to the Lennard-Jones potential $\delta t = (1/60 \div 1/30)(2\pi/\omega_E) \approx 0.01$, where $\omega_E = \sqrt{3}\omega_0$ is the Einstein frequency (Holian and Ravelo, 1995; Holian et al., 1995). In the preceding equation, $\omega_0 = C_0 / r_0$ was used to define the fundamental harmonic frequency related to the sound speed ($C_0 \approx 9.0$) and equilibrium interatomic distance ($r_0 = 1.0$).

3.1.1 Distribution of Fragment Sizes

The metals provide a poor resistance to high-velocity projectiles since their properties deteriorate at high temperature. This provides a motivation to consider ceramic shields. However, a brittle (ceramic, concrete, rock) target may be defeated by a penetrator as a result of extensive cracking due to its inferior tensile strength. This is a main reason why the catastrophic fragmentation events caused by impulsive loading attract considerable attention of physics and applied mechanics communities. The substantial literature exists in which the fundamental principles of dynamic fragmentation process were investigated experimentally and theoretically (e.g., Mott, 1947; Dienes, 1978; Grady and Kip, 1985; Chang and Redner, 1990; Miller et al., 1999). Holian and Grady (1988) were apparently first to use molecular dynamics to explore the fragmentation phenomena by simulating a homogeneous adiabatic expansion of condensed matter. According to their results the cumulative distribution of fragment masses is well represented by a bimodal-exponential distribution.

The main objective of this set of simulations was to determine whether the Holian and Grady's result remains valid for a non-homogeneous fragmentation process caused by application of a highly non-uniform transient strain rate field. The distribution of fragment sizes is studied, therefore, during the impact of a slender, deformable Lennard-Jones projectile (19×301 atoms) with a rigid target. Simulations were performed for three striking velocities: $0.22C_L$, $0.45C_L$ and $0.67C_L$, where $C_L \approx 9.0$ is the velocity of longitudinal elastic wave propagation of the Lennard-Jones solid in vacuum. The results obtained for the smallest impact velocity $v_s = 0.22C_L$ are presented in Fig. 3.1 Two other striking velocities provided qualitatively similar results. The histogram of the cumulative number of fragments and corresponding log-plot suggest the bilinear exponential distribution, which agrees with the results obtained by Holian and Grady (1988) for the homogeneous adiabatic expansion. A more pronounced bimodal character of Fig. 3.1b compared to Holian and Grady's plots may be attributed to the nonhomogeneous strain rate field and the relatively small size of the sample used in this study.

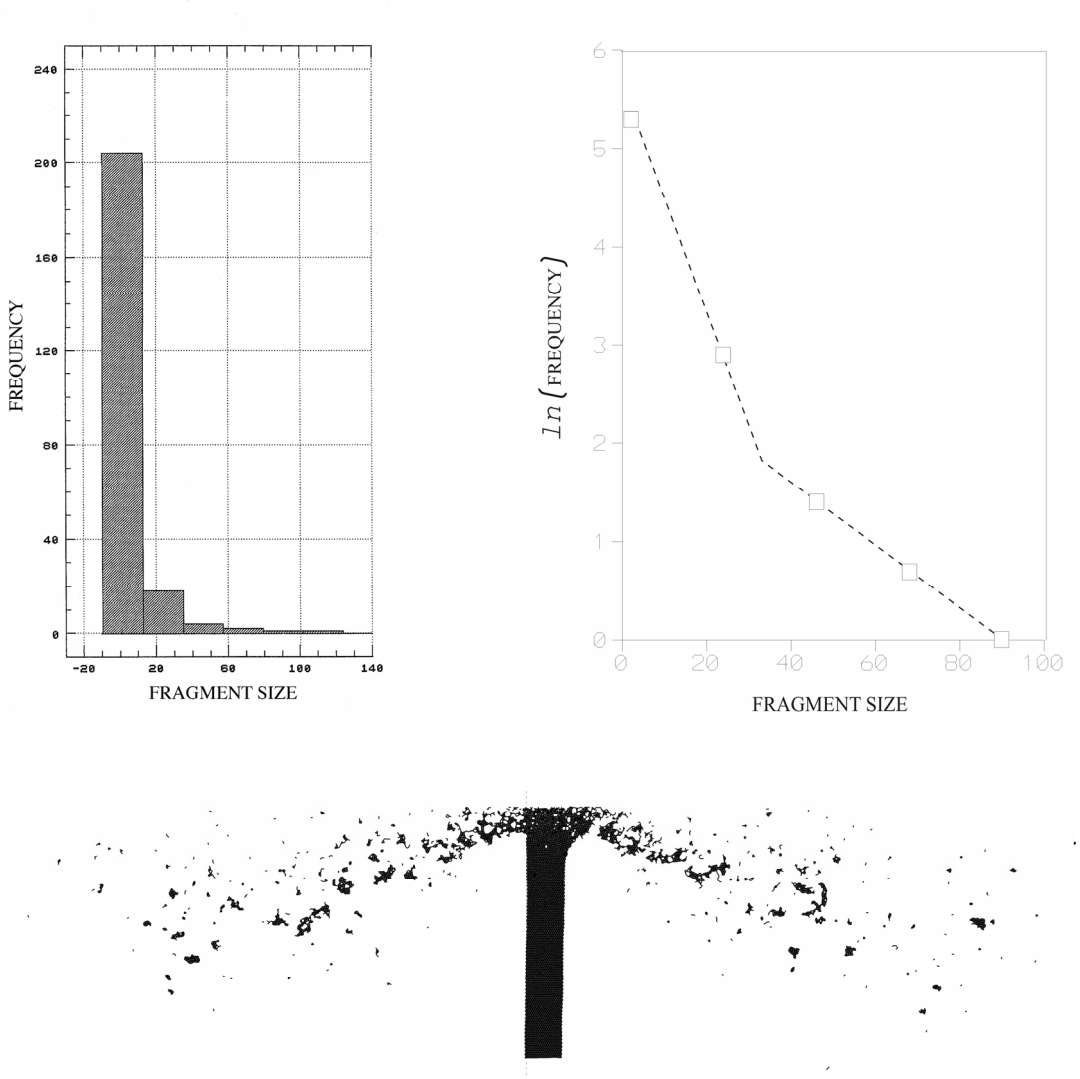

Fig. 3.1. The size distribution of fragments of a rod impacting a rigid target at high velocity (v=0.22C_L); (a) Histogram, and (b) corresponding log-plot representing fragment size distribution in (c) State at which ≈20% of the projectile is eroded.

3.1.2 Relative Shortening of the Projectile

The impact of a flat-nose projectile on a rigid boundary provides a convenient method to obtain the dynamic yield strength of the projectile material at large strains and at strain rates greater than $10^5\ s^{-1}$ (Taylor, 1947; Wilkins and Guinan, 1973). According to a refinement of the original Taylor's analysis, the relative shortening of

the projectile is

$$\frac{L_1}{L_0} = \left(1 - \frac{h_{pf}}{L_0}\right) \exp\left(-\frac{\rho_0 v}{2\sigma_{yd}}\right) + \frac{h_{pf}}{L_0} \tag{3.1}$$

In equation (3.1) L_0 and L_1 are the initial and final length of the projectile, respectively, h_{pf} distance of the plastic front from the contact zone, ρ_0 mass density of the projectile material, v striking velocity, and σ_{yd} dynamic yield strength. Wilkins and Guinan (1973) report an excellent agreement between results obtained by using (3.1) and experimental data for number of metals (aluminum, steel, tantalum).

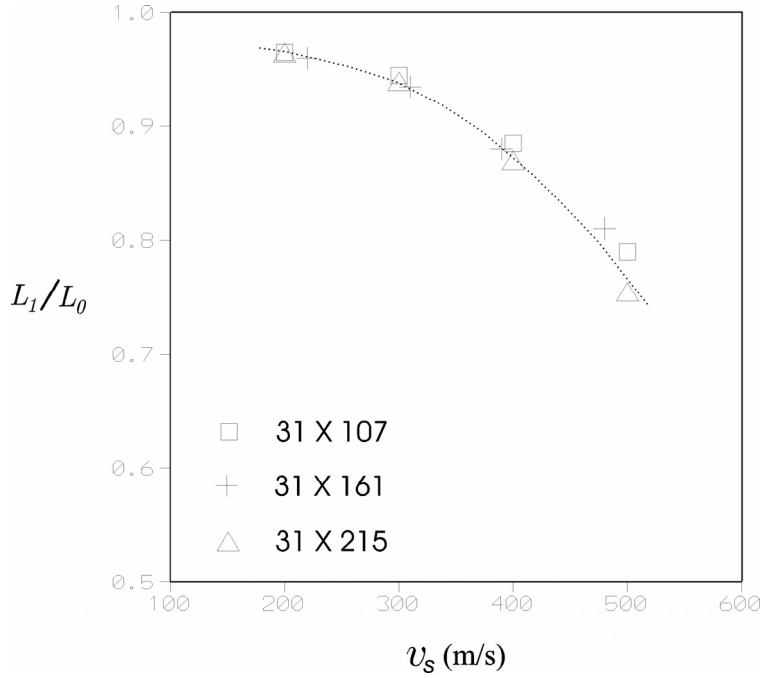

Fig. 3.2. Relative shortening of projectile as a function of striking velocity.

The shortening of the two-dimensional Lennard-Jones solid projectile during Taylor test, was analyzed as a function of the striking velocity and length-to-width (slenderness) ratio of the projectile. Twelve simulations were performed with three projectiles (31×107, 31×161, and 31×215 atoms) of different slenderness ratios ($L_0 / w_0 = 3.0, 4.6, 6.2$). The curve representing the relative shortening of the projectile as a function of the striking velocity (Fig. 3.2) is in good qualitative agreement with the experimental data (Wilkins and Guinan, 1973; Mayers, 1994). Presented simulation data confirm the well known result according to which the relative

shortening of the projectile (L_1/L_0) is independent of its slenderness ratio. The smaller values of L_1/L_0 obtained from two-dimensional molecular dynamics simulations, compared to the (three-dimensional) experimental results, were expected since within the plane strain framework, such as two-dimensional lattice simulations, a restriction is imposed on deformation in one direction.

3.1.3 Stress Wave Features and Disturbance Propagation Velocity

The measurement of inelastic wave profiles and velocities is another method used to validate constitutive models (Nicholas and Recht, 1990). This series of simulations is performed with three two-dimensional Lennard-Jones projectiles (19×301, 25×227, and 97×29 atoms) of different slenderness ratios (L_0/w_0 = 14.4, 8.16, and 0.25). Stress and velocity profiles were recorded during the impact at six measurement points (M_1–M_6) along the central axis of the projectile (Fig. 3.3). These data are, then, used to estimate the velocity of wave propagation within the projectile. The first point (M_1) is located approximately $0.1L_0$ from the nose (proximal end) of the projectile, while the last one (M_6) is positioned at the same distance form the distal end of the rod. Thus, the distance between these two measurement points is approximately $0.8L_0$, where L_0 is the initial length of the projectile (Fig. 3.3).

The average velocity of disturbance propagation is defined as the ratio between the distance separating measurement points M_1 and M_6 and the time lag between the occurrence of the signal at the second point with respect to the first one. Simulations are repeated for twenty-seven combinations of impact velocities and projectile slenderness ratios. The results of these simulations are plotted in Fig. 3.4a.

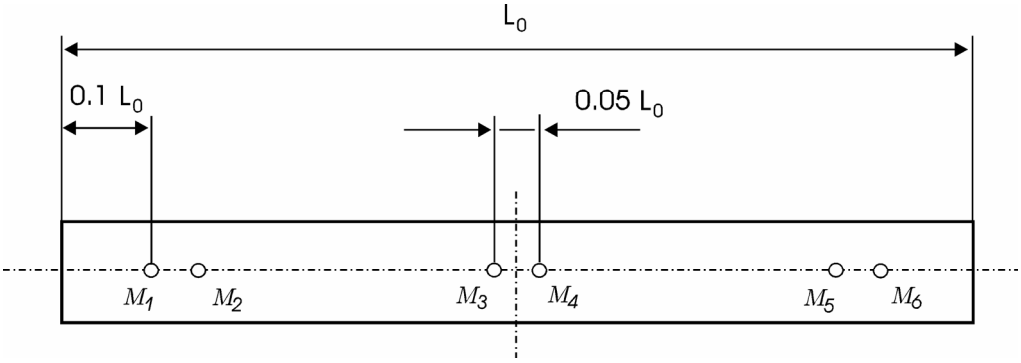

Fig. 3.3. Projectile geometry and location of the measurement points.

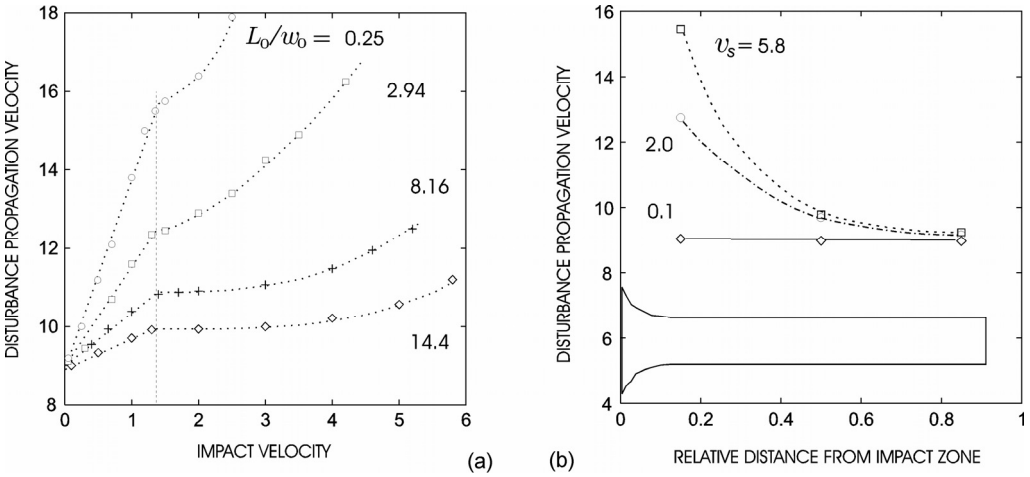

Fig. 3.4. Dependence of the change of the disturbance propagation velocity on the (a) impact velocity for various slenderness ratios, (b) relative distance from contact zone for different impact velocities.

At very small impact velocities the signal is transmitted at the longitudinal elastic wave propagation velocity C_L, irrespective of the slenderness ratio. With the increase of striking velocity, the disturbance propagation velocity initially increases linearly. The rate of increase is strongly dependent on the slenderness ratio. The linear increase of the velocity of wave propagation with the impact velocity is in agreement with the ballistic equation of state, which for most metals[13] has the linear form

$$U_S = C_L + S_1 U_p \tag{3.2}$$

where U_S is shock velocity, U_p particle velocity and S_1 empirical parameter (Mayers, 1994). The dependence of the rate (gradient) of increase of the wave propagation velocity on the slenderness ratio can be attributed to the geometrical confinement and the resulting pressure build-up. At small slenderness ratios (plate-like "projectile") the confinement of the surrounding material imposes severe constraints on the lateral motion of atoms, which may lead to a significant pressure build-up. The plastic deformation and fragmentation, which occur in the vicinity of the contact zone, evidently contribute to the complexity of presented picture (Fig. 3.4a). Inflection point, which characterizes the transition from a linear to nonlinear dependence of

[13] The linear equation of state is not applicable if the material is very porous, or if it undergoes phase transformation.

wave propagation velocity on the rate of impact (Fig. 3.4a), seems to represent a "fragmentation threshold". It is interesting that the transition takes place at the striking velocity $v_s \approx 0.13C_L$ irrespective of the slenderness ratio.

To demonstrate the influence of pressure (stress state) on the disturbance propagation velocity simulations are used to estimate the "local" velocity of wave propagation. The local velocities are measured in the vicinity of the proximal (M_1–M_2) and distal (M_5–M_6) end of the projectile, in addition to the mid-section area (M_3–M_4). The measurement distance between these pairs of points is $\approx 0.05L_0$ (except for the plate-like projectile where it has to be increased to $\approx 0.075L_0$ due to the small thickness). A trend is clearly demonstrated in Fig. 3.4b. As expected, for a very small impact velocity the disturbance propagates with velocity C_L regardless of the distance from the impact zone. The stress wave is, therefore, elastic. With the increase of the striking velocity the velocity of wave propagation changes significantly with the distance from the projectile-target interface. The notable difference between local velocities of disturbance propagation is attributed to the stress wave attenuation, and is consistent with the equation of state (3.2).

The simulations are also used to study the size effect by significantly varying the size of the projectile (5×67, 7×101, 13×201, and 19×301) while keeping the length-to-width ratio, $L_0/w_0 = 14.4$, constant. According to the simulation results are presented in Table 3.1, the convergence of estimated velocities with increase of the lattice size is very fast. The accuracy is satisfactory keeping in mind that the exact value of the velocity of elastic wave propagation in two-dimensional Lennard-Jones solid is $C_L = 9.0\sqrt{\varepsilon_{LJ}/m} = 9.0$. Thus, even for the smallest projectile (5×67) the relative error is within 5%.

Table 3.1. Convergence of the estimated velocity of disturbance propagation with the increase of lattice (projectile) size.

	C [–]			
v [–]	5×67	7×101	13×201	19×301
0.10	8.52	8.86	8.90	9.01
1.0	9.36	9.25	9.70	9.71
3.0	9.55	9.52	9.96	10.0
5.0	10.5	10.15	10.4	10.6

3.1.4 Temperature Field

The evaluation of the temperature field within both the projectile and target is far beyond the capabilities of presently available experimental methods. This is, at least, a partial reason for many unanswered questions related to the physical state of brittle solid during the shock deformation in general, and the existence of thermodynamic equilibrium in particular. Experimentally, the bulk of information related to the nature of the thermal state of the material in the course of deformation is inferred from the post-impact micrographic analyses. But, the analysis of the time history of failure is much more valuable than the simple examination of the final outcome (Espinosa and Zavattieri, 2003b). For example, the examination of the fracture surface in and near the contact zone reveals that the target material melts during penetration (Hauver et al, 1992; Strassburger and Senf, 1996). The extent of melting obviously depends on material. The objective of the present numerical simulation is to address some of the questions that arise from the consideration of high strain rate, non-homogeneous deformation process, by using molecular dynamics.

The first Taylor test is simulated to check whether the Maxwell-Boltzmann distribution of vibrational velocities (which defines local equilibrium) is established during the impact or only after the projectile comes to rest. The projectile is modelled by a two-dimensional, Lennard-Jones, triangular lattice (25×227 atoms). The impact velocity is $v_s = 0.155 C_L$. The velocity data is recorded twenty times throughout the impact simulation in the proximal area of the projectile (Fig. 3.5). The statistical test of the velocity data is performed by using the software Execustat®3.0 (Strategy Plus Inc., 1991). The tested hypothesis is that the velocity data represents a random sample from the Maxwell-Boltzmann distribution. The statistical test results (in which: - ≡ the hypothesis is rejected with 95% confidence, + ≡ the hypothesis is not rejected) are presented in Fig. 3.5 together with the plot of the time history of the average velocity of all projectile atoms. It is assumed that projectile comes to a rest when the average velocity of all projectile-atoms becomes equal to zero. From the results plotted in Fig. 3.5 it is obvious that the thermal equilibrium is established well before the impact ends. Unfortunately, it is rather difficult to state whether the Maxwell-Boltzmann distribution of velocity is established in the main part of the projectile, or only in the broken-away fragments that are no longer exposed to the external load (Mastilovic and Krajcinovic, 1999b). Therefore, while the basic questions concerning the thermodynamic equilibrium under these extreme loading conditions are left open to discussion and future work, the temperature will simply be considered as being a measure of the instantaneous vibrational kinetic energy within a certain averaging area, as discussed in Section 2.1.3.

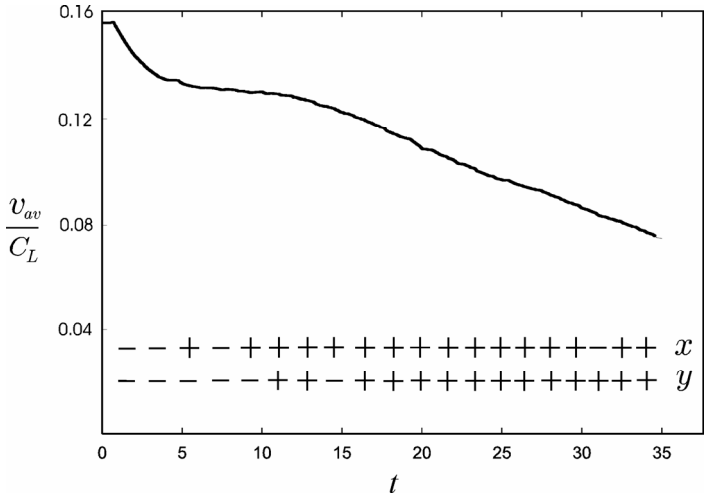

Fig. 3.5. Statistical test of the hypothesis that the velocity data, obtained from an area in the proximal end of the projectile during the Taylor test, represents a random sample corresponding to Maxwell-Boltzmann distribution of vibrational velocities.

The next series of simulations is performed with the projectile (25×227) made of Lennard-Jones two-dimensional solid, defined by (2.4). In contrast to the previously performed simulations with non-dimensional model parameters, in the present set of simulations the model parameters were estimated to match, as close as possible, the physical properties of tungsten (W). The mass of all atoms is $m_i = 3\times10^{-25}\,kg$ (atomic mass 183.85 g/mol) and the equilibrium Interatomic distance $r_0 \approx 2.8\times10^{-10}\,m$ (atomic radius $1.41\times10^{-10}\,m$) (Weast, 1976). The depth of the potential well in (2.4) is roughly estimated to be $\varepsilon_{LJ} \approx 8\times10^{-20}\,J$ based on the sublimation energy.

At a low impact velocity, $v_s = 100$ *m/s*, the thermal wave of gradually decaying amplitude propagates along the axis of the slightly deformed projectile (Fig. 3.6). The temperatures labeled on the isothermal contours represent the increase in temperature (in degrees Kelvin, *K*) attributed to the vibrations of atoms caused by the impact. At a higher impact velocity, $v_s = 700$ *m/s*, the zone of the highest thermal activities is, as expected, localized near the contact zone (Fig. 3.7) (Mastilovic and Krajcinovic, 1999b).

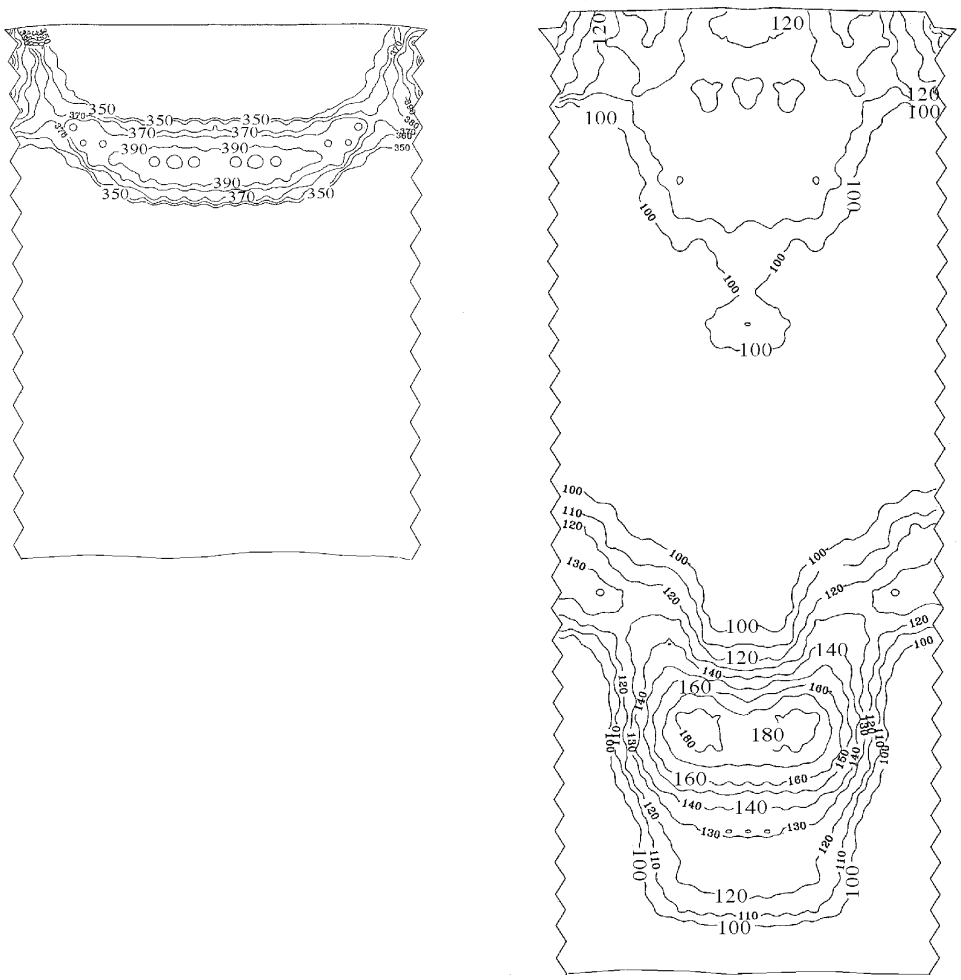

Fig. 3.6. Temperature field in a projectile during a low-velocity impact at two consecutive instants of time; (a) $t = t_1$, and (b) $t = t_2 > t_1$.

The relatively high temperature, of the order of 4000 *K*, obtained at a moderate striking velocity can be partially attributed to the rigid target. In the case of impact into deformable target the temperature is, according to these simulations, significantly lower. In the case of collision with a rigid target the entire kinetic energy of the projectile transforms into the vibrational particle velocity. The temperature is proportional to a second degree of that velocity (2.8). According to Fig. 3.7, the projectile will apparently melt within a thin region in the vicinity of the contact zone, since the melting point of tungsten is 3695 *K*.

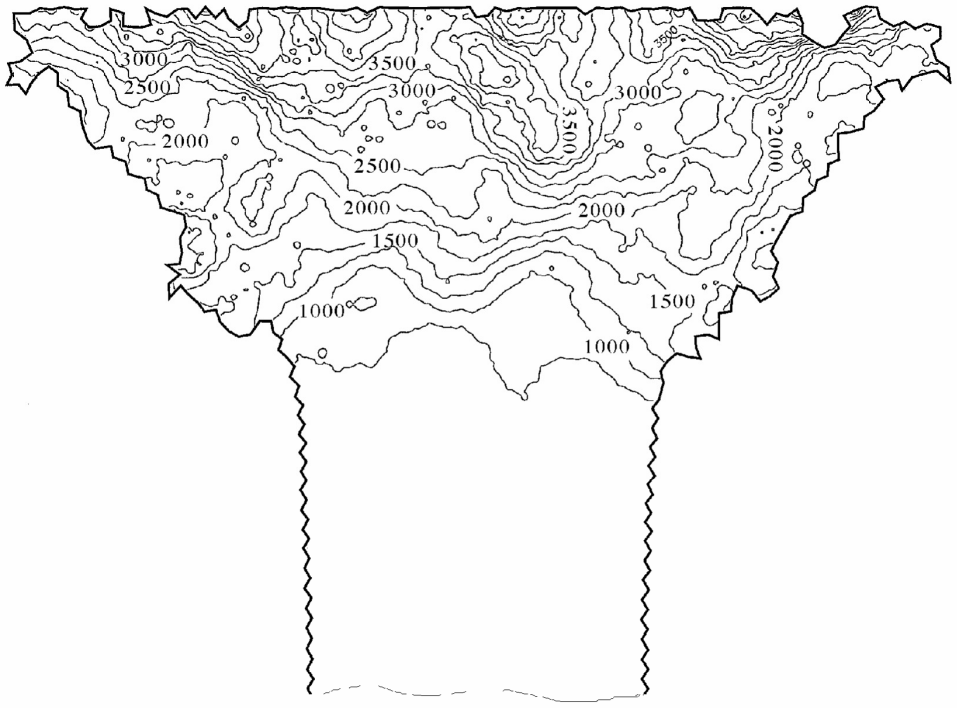

Fig. 3.7. Temperature field in a projectile during moderate-velocity impact.

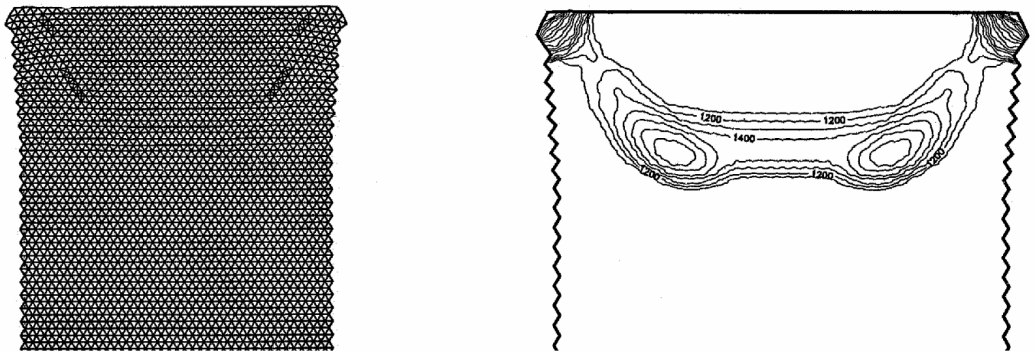

Fig. 3.8. Temperature concentration around the two pairs of dislocations emitted from the corners of a flat-nosed projectile following its impact on a rigid target; (a) deformed lattice, and (b) corresponding temperature field.

In the initial stage of the moderate-velocity impact ($v_s = 700\ m/s$) two pairs of dislocations are emitted from the corners of the flat-ended projectile nose (Fig. 3.8a).

The concentration of temperature accompanying the propagating dislocations is demonstrated in Fig. 3.8b (Mastilovic and Krajcinovic, 1999b). This observation is consistent with the general notion that "the moving dislocations acquire a large kinetic energy that is released when the dislocation is stopped" (Nabarro, 1987).

As already mentioned, the choice of the size of the averaging region (Fig. 2.2) is somewhat arbitrary. It is supposed to be large enough to provide a meaningful statistical ensemble over which the averaging is performed, and to be, simultaneously, fine enough to provide a reasonable resolution for the evaluation of particular field parameter (in this case temperature). The large size of the averaging area, also, increases the program execution time. Three Taylor test simulations, characterized by different radii of averaging region, were performed in order to make an optimal choice. The center of the region was located at a distance $0.2L_0$ from the proximal end of the projectile (of the initial length L_0).

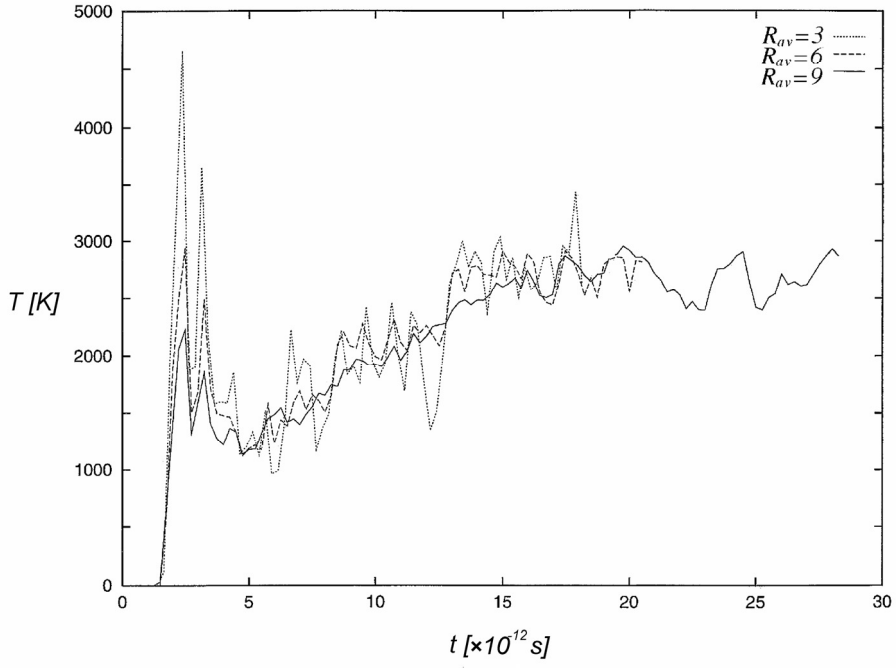

Fig. 3.9. Transient temperature evolution for three sizes of the averaging region.

The considered radii are: $R_{\text{av}} = 3r_0$, $6r_0$, and $9r_0$, where r_0 is the equilibrium interatomic distance. The transient temperature evolutions, for the three radii are plotted in Fig. 3.9. The convergence of the temperature profile is relatively fast. The largest radius of averaging region is, therefore, used consistently throughout the present study.

3.2 PLANAR IMPACT

The planar impact experiment is one of the primary sources of data needed for the formulation of the equation of state and for determination of various dynamic material parameters including the dynamic tensile fracture characteristics. Under planar impact at high velocities, materials are subjected to a state of uniaxial strain since no lateral motion can occur until release waves arrive from the edges of the plate.

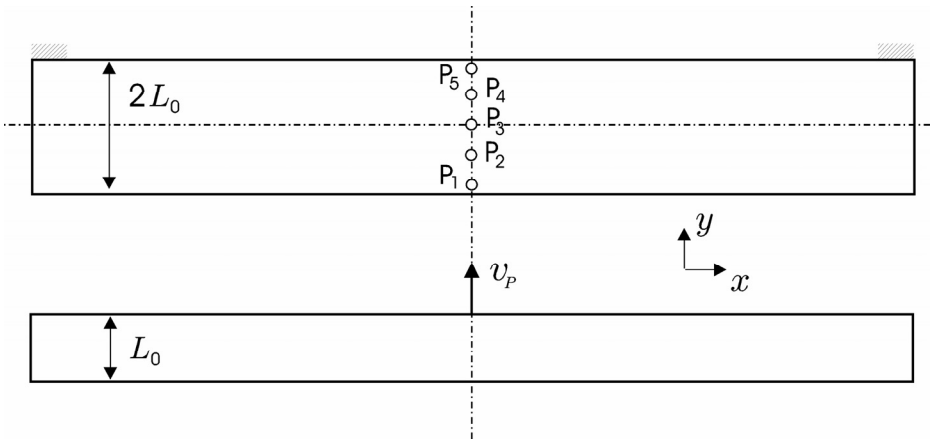

Fig. 3.10. Schematic representation of a planar impact set-up.

The first plate-impact test was simulated approximating the flyer plate by a two-dimensional ensemble of 351×21 atoms moving in the vertical (y-) direction with velocity of 700 *m/s* ($0.175C_L$) towards a stationary target plate approximated by an ensemble of 351×41 atoms. The target plate supports were introduced by constraining the motion of the upper left and right corner atoms in the direction of impact (shaded parts of the plate boundary in Fig. 3.10). All other atoms forming other surfaces of both plates were free to move in both directions. Both flyer and target plate were approximated by the two-dimensional Lennard-Jones solid, defined by (2.4). The model parameters were estimated to match, as close as possible, the physical properties of tungsten, as discussed in Section 3.1.4. The transient stress wave evolution in the target plate was measured by recording the normal stress in the direction of y-axis at five points on the vertical symmetry axis (Fig. 3.10). The generic stress profiles for both low- and high-velocity impact recorded at point P_3, closest to the middle of the plate where spalling was expected to take place, are plotted in Fig. 3.11.

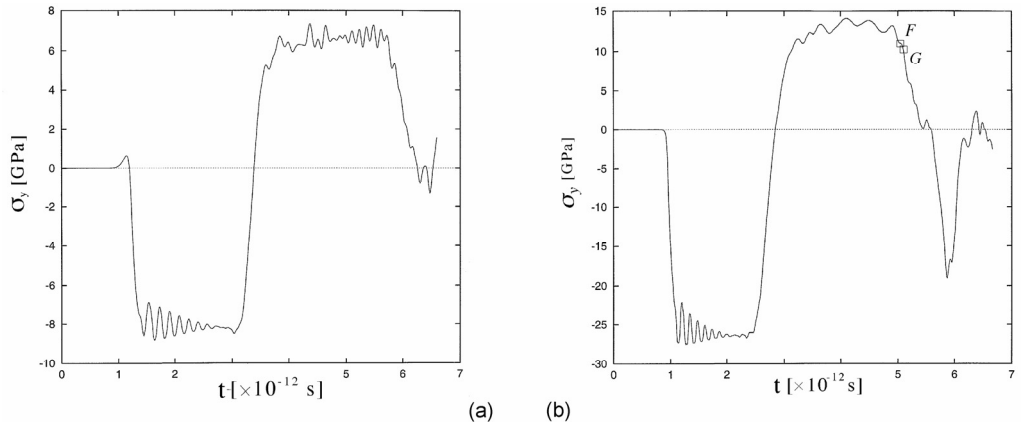

Fig. 3.11. Wave profiles obtained from the planar impact simulation; (a) low-velocity impact, (b) high-velocity impact.

The low-velocity plate-impact is characterized by absence of a significant damage in general, and the spalling fracture in particular. This is reflected by the corresponding stress wave profile presented in Fig. 3.11a. Upon impact, the elastic stress waves are emitted from the contact surface into the flier and target plates (Fig. 3.12). These compression waves reflect off the free surfaces as release (rarefraction) waves and propagate back through the compressed material. The magnitudes of compressive and reflected tensile pulses are almost the same, which suggest that the stress wave propagation is not accompanied by significant damage (Meyers and Aimone, 1983). The peculiar increase of stress preceding the compression wave is characteristic of the molecular dynamics simulations of low-velocity plate-impact. This stress peak is attributed to the attractive forces initially exerted between the surface-atoms of two approaching plates. The repulsive interaction takes place as soon as the distance between these two rows of atoms, facing each other, falls below the equilibrium interatomic distance, r_0.

In the case of the high-velocity impact the transient stress waves emanate from the contact surface and start propagating in the opposite directions towards the free edges of the two plates (Fig. 3.12). As the compression waves encounter the free surfaces of the flyer and target plate they reflect and propagate back, broadened by nonlinear effects (Wagner et al., 1992). Assuming that the wave propagation velocities are constant, the reflected tension waves meet, defining the spall plane, at a distance equal to the thickness of the flyer plate measured from the free surface of the target. If both the amplitude and duration of the reflected tensile pulse are sufficiently large, the spalling initiates causing the release waves to emanate from the newly created free surfaces and decrease the tensile stresses (Meyers and Aimone, 1983). All described

features are clearly recognizable from the obtained simulation data. The snapshots of the two plates in Fig. 3.13 taken immediately before, (a), and after, (b), the spall fracture takes place, correspond to the points *F* and *G* of the stress wave profile Fig. 3.11b.

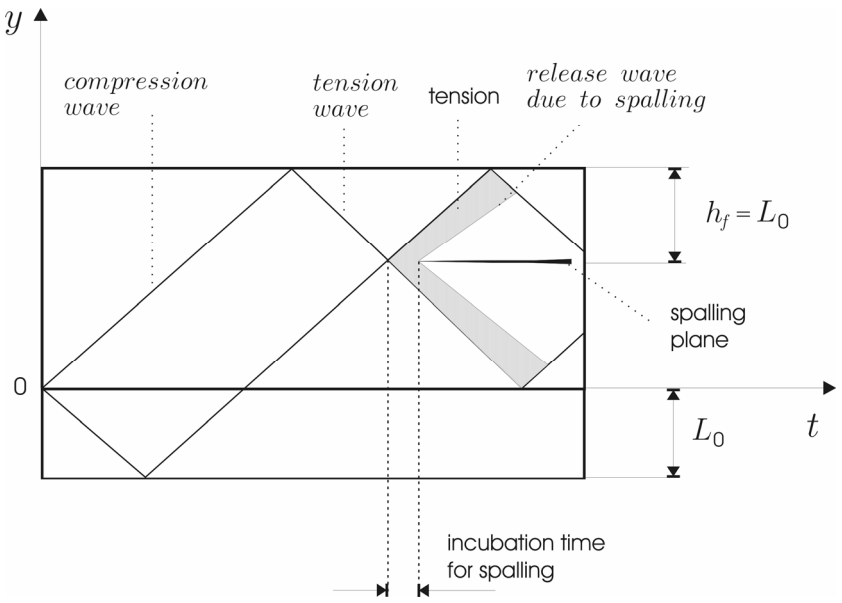

Fig. 3.12. Schematic position-time profile of stress wave propagation during planar impact.

In this analysis the shock wave pressure is related to a mean normal stress by using the fact that the two-dimensional triangular lattice is equivalent to three-dimensional continuum under a plane strain condition (Monette and Anderson, 1994). According to simulation results, the stress component in the lateral direction (perpendicular to the impact direction) is $\sigma_x = \upsilon\sigma_y$, where υ is the Poisson's ratio. This is a consequence of the inability of particles to relax laterally fast enough, at high strain rates of loading, due to inertia. The stress component in the direction perpendicular to the lattice plane is $\sigma_z = \upsilon\ (\sigma_x + \sigma_y)$. Therefore, the mean normal stress, corresponding to $\sigma_y = 27\ GPa$, is $p_m = (1+\upsilon)^2\ \sigma_y/3 = 16$ GPa (Meyers, 1994).

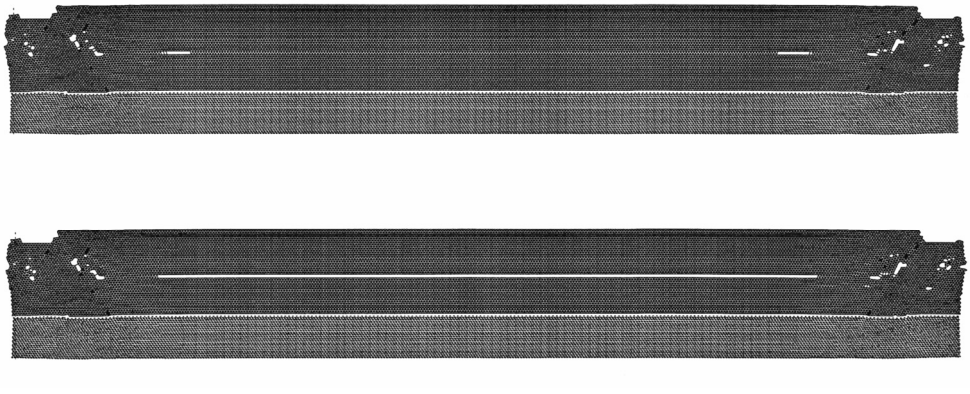

Fig. 3.13. Snapshots of the flyer and target plate immediately before (a) and after the spalling fracture.

Hence, the estimated velocity of disturbance propagation, $C_S = 5500\ m/s$, is in reasonably good agreement with the experimental shock wave data for tungsten, $C_S = 4300\ m/s$ at a corresponding pressure of $p = 16\ GPa$, keeping in mind the simplicity of the model, rough estimate of model parameters (especially ε_{LJ}), and a coarse resolution of the velocity measurement due to the small thickness ($20\sqrt{3}\,r_0$) of the plate. It is worthwile to emphasize that no attempt was made to improve the agreement of the results by modification of input parameters.

For the second plate-impact simulation the geometry of the plates and the impact velocity were changed. The flyer plate (731×7 atoms) moving in the vertical direction with a velocity of 900 *m/s* ($0.22C_L$) collides with the stationary target plate of approximately twelve times larger thickness (731×75 atoms). The total number of atoms is ≈ 60000. As expected, the spalling plane was located at the distance h_f, equal to the thickness of the flyer plate, from the free surface of the target plate (Figs. 3.12 and 3.14).

Fig. 3.14. Snapshot of a planar impact with relatively thin flyer plate (a detail).

The stress wave profiles recorded at five measurement points, P_1–P_5 (Fig. 3.10), along the vertical axis of symmetry of the target plate are plotted in Fig. 3.15 (the solid line corresponds to the point P_1 closest to the contact zone). This stress curves in

Fig. 3.15 provide a detailed insight into the wave evolution (attenuation, interaction, reflection), and can be used to estimate several important physical characteristics of the dynamic behavior of material (such as the velocity of wave propagation or the spall strength[14]).

At higher impact velocities the shock wave tends to attenuate. The increase of the amplitude of the stress wave from 27 *GPa* to 37 *GPa* (in two simulations), is proportional to the increase of the impact velocity from 700 *m/s* to 900 *m/s*. This suggests that the ballistic equation of state is linear which is in agreement with the experimental shock data for metals (Meyers, 1994). The estimated velocity of shock wave propagation was $C_S = 5550$ *m/s* compared with the experimental value of $C_S = 4400$ *m/s* at $p = 22$ *GPa* (which corresponds to $\sigma_y = 37$ *GPa*). The stress wave profiles presented in Fig. 3.15 clearly demonstrate a stress wave attenuation, i.e. decay of the stress pulse as it progresses through the target plate. This decay is attributed to the energy dissipation that accompanies the shock wave propagation. Indeed, it is observed that "the inherent irreversibility of the process is such that the energy carried by shock pulse continuously decreases" (Meyers and Aimone, 1983). Most of the dissipated energy is transformed into heat and somewhat less on the formation of defects (i.e. internal surfaces). The energy dissipation is manifested by the change of the shape and magnitude of the stress pulse as it travels through the target plate.

The previously described plate-impact simulations have two major disadvantages. First, it is obvious from the snapshots (Fig. 3.13) that the target-plate supports, no matter how small, disrupt the uniform state of deformation in their vicinity. Since the length-to-width ratio of the plate is relatively small ($L_0/w_0 = 0.088$) this may not have a significant effect on the measurements performed at the symmetry axis. Nonetheless, this problem can be easily solved by assigning the initial velocities to both plates in such a way that upon collision the velocity of their center of mass is zero (Holian et al., 1992). Secondly, the periodic boundary conditions can be introduced in the lateral direction making the simulations much more computationally efficient. Both improvements were introduced in the last plate-impact simulation.

The third simulation was performed using the particle dynamics model (Section 2.2). The model consists of the flyer plate of mass m_P (81×79 particles) moving with velocity $2v_P/3$ in vertical direction, and the target plate of mass $2\,m_P$ (81×157 particles) moving in opposite direction with velocity $-v_P/3$. Thus, the magnitude of the resulting impact velocity is v_P (Fig. 3.16). After the collision the velocity of the center of mass of this system of two plates is equal to zero. The system is infinitely extended in the lateral direction using the periodic boundary conditions in the planes with normals parallel to the *x*- axis.

---

[14] The dynamic tensile strength under uniaxial strain.

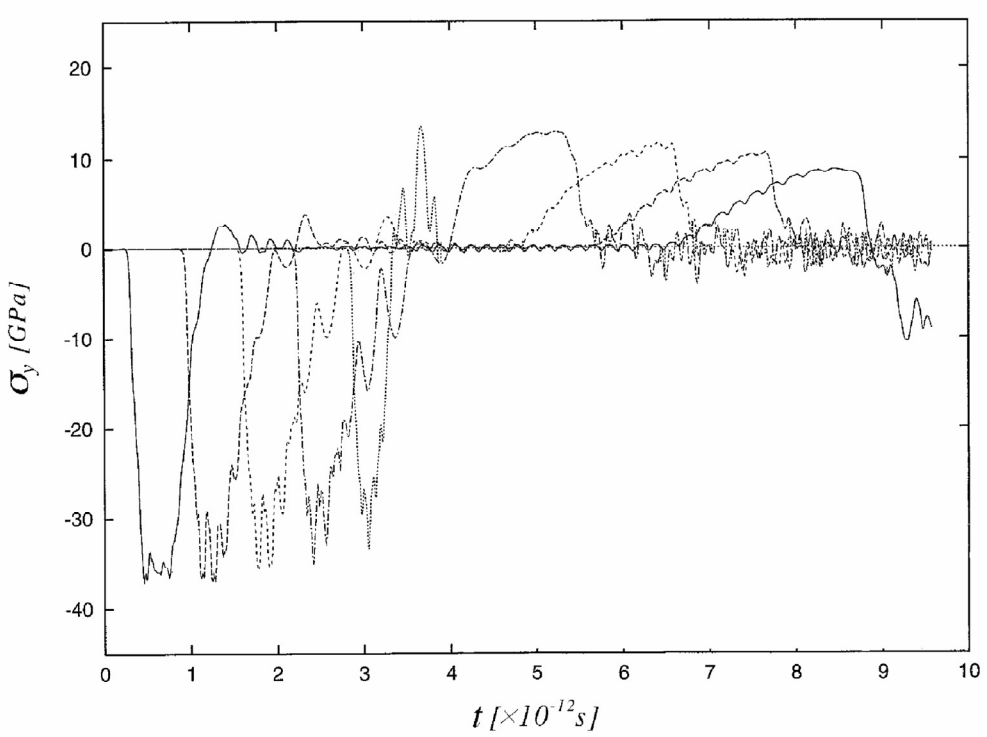

Fig. 3.15. Shock wave attenuation during the plate impact.

These changes enable the increase of the target plate thickness to $L_0 = 86\sqrt{3}\,\bar{\lambda}$ even though the total number of particles (≈ 19000) is smaller then in the previously discussed molecular dynamics models. The geometrical and structural parameters of the simulation model are as follows: the average link stiffness $\bar{k} = 50$, mean bond length (resolution length) $\bar{\lambda} = 1$, critical link elongation $\varepsilon_{cr} = 0.1\%$, geometrical disorder parameter $\alpha_l = 0.2$, and stiffness distribution parameter $\beta_l = 0.6$. The most important differences between the present material model and the one used for the cavity-expansion simulation in Section 3.4, are: (*i*) force-elongation relation is completely linear (Hookean), and (*ii*) superior-stiffness aggregates ($k_a = 14\bar{k}$) are embedded into the brittle matrix (motivated by the aggregates and cement paste in concrete). The area fraction of the aggregates is approximately 0.5 (Fig. 3.16b).

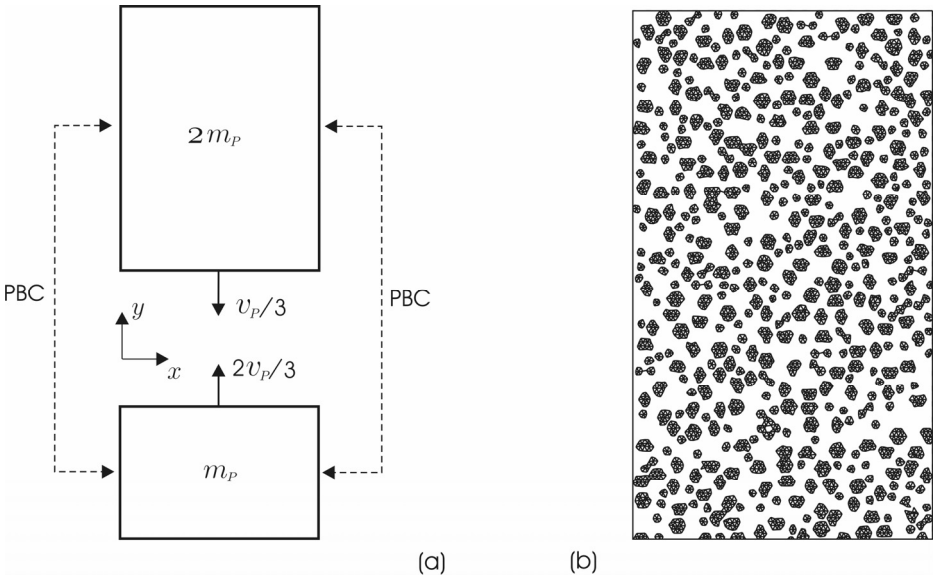

Fig. 3.16. Planar-impact set-up for a “concrete” specimen with the periodic boundary conditions (PBC) and both flyer and target plate in motion; (a) schematics of the system, (b) distribution of stiff aggregates within a softer matrix.

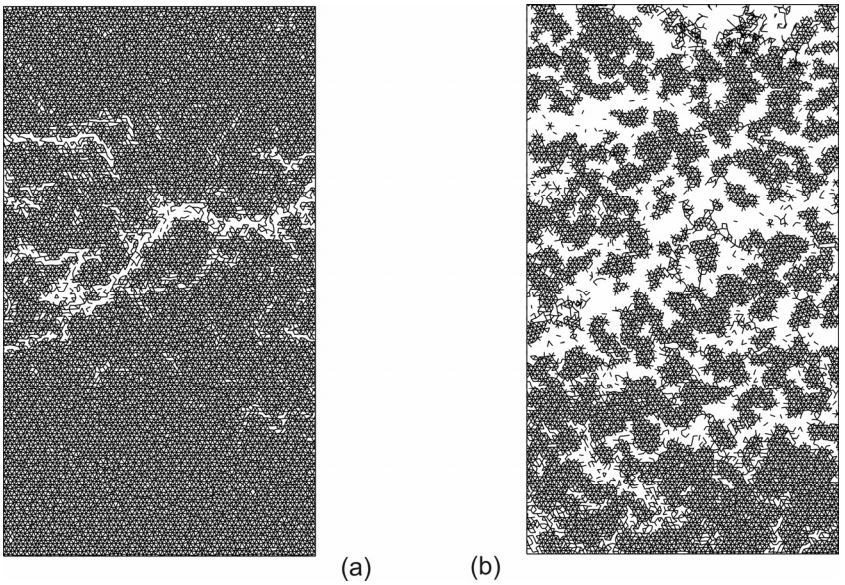

Fig. 3.17. Dependence of the damage evolution pattern and failure mode of a “concrete” plate on the impact velocity; (a) low- and (b) high-impact velocity.

The kinetic energy of the flyer and target plates imparted by collision is converted into the kinetic and deformation (potential) energy of the entire system. Some of the energy is consumed in the process of the formation of defects, i.e. the rupture of links. The dependence of the damage patterns on the impact velocity is demonstrated in Fig. 3.17. The spalling failure is characterized by a single crack transecting the target plate that occurs at moderate impact velocities. The snapshot of the target plate presented in Fig. 3.17a corresponds to the impact velocity $v_P = 0.04\ C_L$, where C_L is the velocity of longitudinal elastic waves. The damage is confined (localized) within a small part of the specimen. The rest of material is not affected.

When the impact velocity is increased by a factor of six, a large fraction of the imparted energy is consumed on the crushing of the target plate, i.e. relatively uniformly distributed microcrack nucleation (Fig. 3.17b). In this case most of the material is transformed or comminuted into a granular phase. The energy used to rupture links (increase damage) is larger than in the previous case. The fracture takes place mainly in the cement paste due to its inferior tensile strength compared to the aggregates. Using the language of rock mechanics these two examples provide an illustration of the inherent brittle to quasi-brittle transition and its dependence on the strain rate (Mastilovic et al., 1996).

3.3 TENSION TEST

The study of rate effects and identification of parameters for cavity-expansion model is the primary motivation for the particle dynamics simulations of the uniaxial and biaxially loaded specimen of a brittle material with disordered microstructure.

As already discussed in Section 1.1, in contrast to the laboratory experiments the vitual experiments (computer simulation tests) are distinguished by practicaly unlimited control over the test conditions. This is of particular importance when studying the material behavior at high strain rates since the establishment of uniform deformation and stress fields within the sample, and the measurement of strains and damage may become an insurmountable problem. A fundamental difference between a high strain rate test and a quasi-static test is in the essential role of inertia and wave propagation in the former. A typical example of the problems inherent to the high-strain rate testing is the formation of a homogeneous strain rate within a sample. The uniform strain-rate field requirement causes considerable difficulties at the upper range of applicability of conventional (high-velocity hydraulic and pneumatic) test machines ($100\ s^{-1}$) due to the non-uniformity induced by the loading conditions. The test data in the range of strain rates extending from $100\ s^{-1}$ to $10^4\ s^{-1}$ are provided usually by Hopkinson bar experiments. It is generally accepted that these experiments will provide valid stress-strain data as long as the stress wave sweeps over the entire specimen at least four times before failure takes place (Ravichandran and Subhash, 1994). Accordingly, the use of average stress and strain is not justified if less than four wave reflections occur before the sample fails, which is common for the very high strain rates. Therefore, the Hopkinson bar experiment has to be carefully designed for a specimen to achieve the uniform, one-dimensional state of stress (Follansbee, 1985; Lok et al, 2002). The arguments related to the uniform deformation apply also to the planar impact experiments. Moreover, the strain history, during these high strain-rate tests ($\dot{\varepsilon} > 10^5 s^{-1}$), can be inferred only by using highly specialized testing techniques. Most of the time that involves the wave propagation analysis, which entails the assumption of the material constitutive behavior. Consequently, the "unique solutions cannot be guaranteed, because some other constitutive model may conceivably provide similar results in a particular wave propagation problem" (Nicholas and Bless, 1985).

The displacement-controlled uniaxial tension test, which overcomes strain-rate limitation of the natural simulation setup, is schematically described in Fig. 3.18. This homogeneous lattice simulation setup is designed by Krajcinovic and Mastilovic

(1999) to ensure uniform distribution of load within a sample by imposing an initial velocity field to all lattice nodes:

$$\dot{x}(t=0) = -\upsilon_0^{(\varepsilon)}\,\dot{\varepsilon}_y\; x \tag{3.3a}$$

$$\dot{y}(t=0) = \dot{\varepsilon}_y\; y \tag{3.3b}$$

defined in the terms of the prescribed strain rate, $\dot{\varepsilon}_y = \dot{L}/L$, and the Poisson's ratio, $\upsilon_0^{(\varepsilon)} = 1/3$, that is characteristic of the two-dimensional triangular lattice, and corresponds to the Poisson's ratio $\upsilon_0 = 1/4$ of a pristine material (Fig. 3.18a). The similar approach was used by Holian et al. (1991) to model the adiabatic expansion.

Subsequently, at $t > 0$, only velocity of the particles located at the specimen longitudinal boundaries ($y = \pm L/2$) boundary is controlled

$$\dot{y} = \pm\,\dot{\varepsilon}_y\; L/2 \tag{3.4}$$

as depicted in Fig. 3.18b. The motion of all other particles is governed by Newton's equation of motion (2.2).

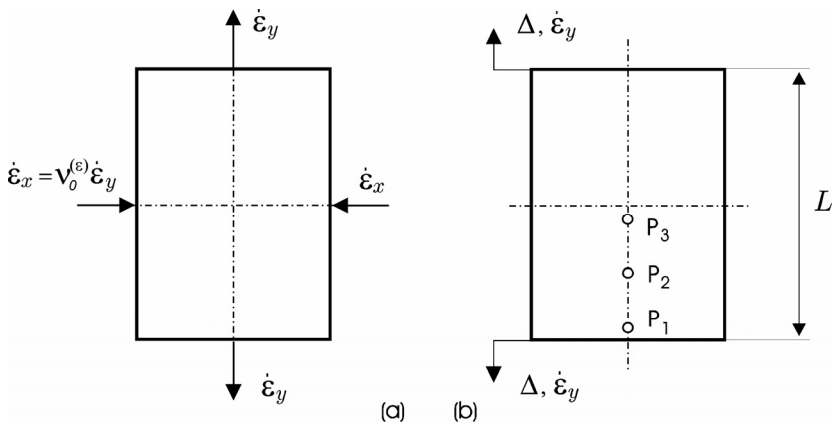

Fig. 3.18. Schematic representation of an uniaxial test set-up; (a) application of the initial strain rate fields, (b) displacement-controlled longitudinal tension.

As a consequence of this initial velocity (strain rate) field applied perpendicular to the loading (y-) direction, the stress in the lateral (x-) direction is fixed to zero regardless of the strain rate of the external load applied in longitudinal direction (Fig. 3.19).

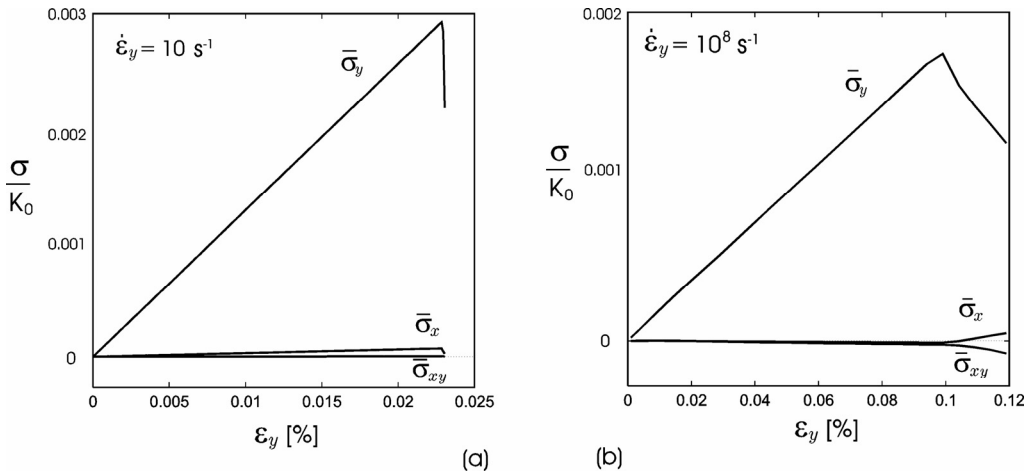

Fig. 3.19. Stress components vs. longitudinal strain; (a) low, and (b) high strain rate.

The effectiveness of this loading procedure is illustrated by two symmetric uniaxial-tension simulations. The first, molecular dynamics, simulation is performed on a relatively small, regular triangular lattice (17 × 67) representing a specimen made of the two-dimensional Lennard-Jones solid. The parameters of the interatomic potential are the same selected in Section 3.2 to match, as close as possible, the material properties of tungsten. The controlled displacement is applied at both the top and bottom surface of the model, at the constant loading rate $\dot{\varepsilon} = 1 \times 10^8 s^{-1}$. The strain in the longitudinal direction is plotted vs. time in Fig. 3.20. The "local" strains recorded at points P_1 and P_3 along the symmetry axis (Fig. 3.18b) are represented, in Fig. 3.20a, by two dashed lines. These strains are analogous to the local strains measured, in laboratory experiments, with electrical-resistance strain gages, which length is small compared to the length of the specimen. The solid line represents the average ("global") strain in the sample, defined as the ratio of the change of length and the original length in the loading direction, $\varepsilon_y = \Delta L/L$. The curves representing the evolutions of the local strains are of the staircase form. Each step marks one complete wave transit through the sample. A qualitatively identical behavior is observed during the Hopkinson bar experiments (Nicholas and Bless, 1985). If only few wave transits (the threshold is conventionally set at four) occur before the specimen fails the stress state within the sample is not uniform and the volume averaging of the stress and strain is not appropriate. On the other hand, if a previously described initial velocity fields are imparted to the lattice at $t = 0$, the local values of both strain and strain rate are almost the same as the value obtained by averaging over the entire volume of the sample (Fig. 3.20b).

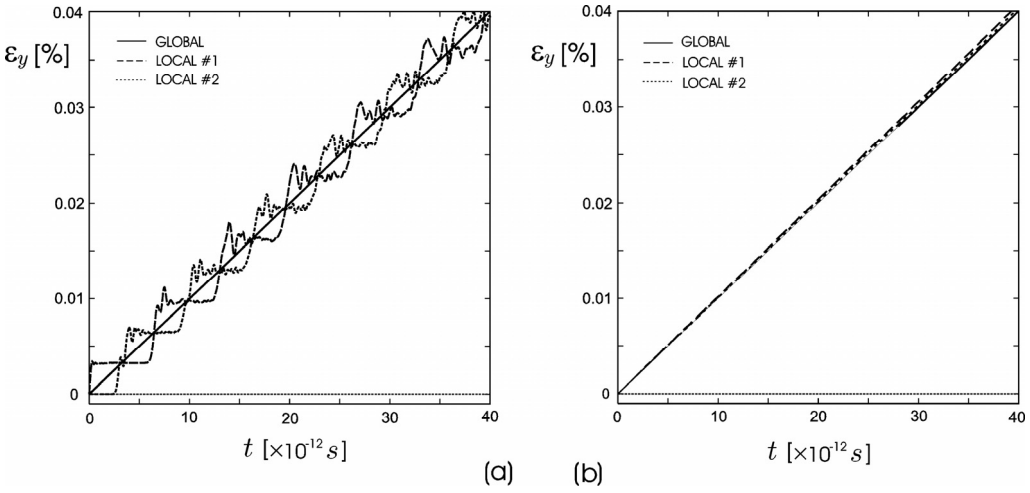

Fig. 3.20. The effect of initially applied strain rate fields on transient, local and global (averaged), strain evolution during the molecular dynamics simulation of an uniaxial tension test; (a) without, and (b) with application of initial strain rate fields.

The second symmetric, uniaxial-tension simulation is performed within the particle dynamics framework. The dicrete model comprised of 85 × 243 particles is defined with following geometric and structural parameters: the average (mean) link stiffness $\bar{k} = 50$, average equilibrium distance between particles $\bar{\lambda} = 1$, geometrical-disorder parameter $\alpha_l = 0.01$, structural-disorder parameter $\beta_l = 0.6$, repulsive wall parameter $B = 5$, and critical strain of the link $\varepsilon_{cr} = 0.1\%$ (see Section 2.2 for details). It seems appropriate to emphasize that the mean link stiffness $\bar{k} = 8E_0 / 5\sqrt{3}$ and critical strain of the link ε_{cr} are directly related to the measurable macroscopic properties of the material, namely modulus of elasticity and the failure strain, respectively. The repulsive wall parameter B is related to the empirical parameter S_1 in the ballistic equation of state (3.2). Its identification, therefore, requires a combination of the experimental and simulation data (Fig. 3.31). The disorder parameters α_l and β_l had to be arbitrarily selected, due to an almost total absence of micrographic data at the time the simulations were performed.

The external load is applied in the same way as in the preceding molecular dynamics simulation. The simulation is terminated when the specimen fails. Contrary to the molecular dynamics simulation, the particle dynamics simulation of the uniaxial tension test cannot be performed at all, at high strain rates, unless the initial velocity (strain rate) field is applied. The reason for this is that, in the present particle dynamics model, the fracture criterion is defined in terms of a relatively small critical

link extension $\varepsilon_{cr} = 0.1\%$. Hence, at extremely high loading rates the top- and bottom-boundary particles, to which the prescribed displacement is directly applied, separate (sooner or later depending on the strain rate and computational time step) from the rest of the lattice. On the other hand, if the appropriate initial strain rate fields are applied, the strain and strain rate are uniformly distributed within the sample.

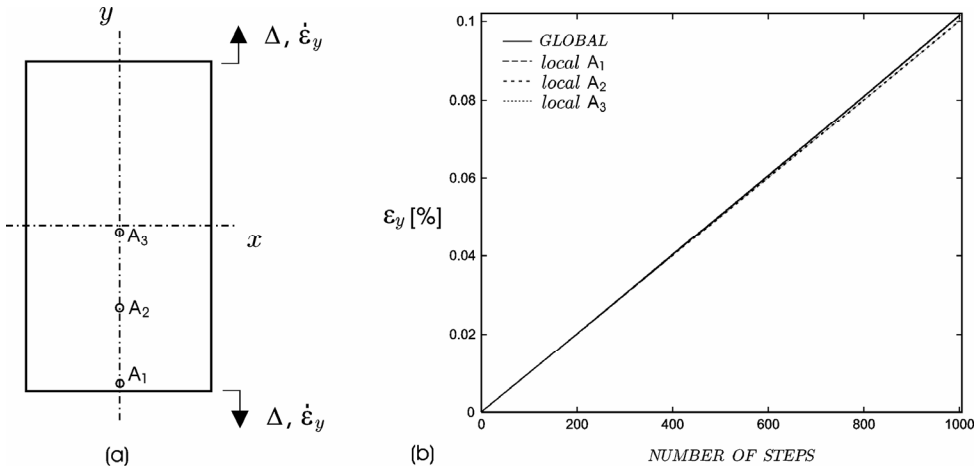

Fig. 3.21. Particle dynamics simulation of uniaxial tension test; (a) a schematic representation of test set-up, and (b) evolution of global (averaged) and local strains within the sample.

The effect of initial strain rate fields is illustrated in Fig. 3.21b in which four strains (one global and three local) are plotted vs. the number of time steps (i.e., time). The local strains, recorded in the measurement points A_1, A_2, and A_3 (Fig. 3.21a), are represented by the dashed lines while the global (average) strain is represented by the solid line. The two local strains, that are measured within the bulk of material, are identical to the global strain. The local strain recorded at the edge of the sample is slightly larger.

The two presented examples demonstrate that the uniform distribution of both strain and strain rate within a sample can be enforced by applying the initial strain rate (velocity) fields in the manner described by (3.3).

Contrary to the conventional molecular dynamics, in which the relations between reduced and physical units are defined by closed-form expressions (Allen and Tildesley, 1987), within particle dynamics framework the conversion of non-dimensional (reduced) units into the physical (*SI*) units is not straightforward. For instance, the strain rates presented in Figs. 3.23 and 3.24 correspond to alumina

(Al_2O_3), with average grain diameter $D = l_c = 10\ \mu m$ and velocity of longitudinal wave propagation $C_L \approx 10\ km/s$ (Grady, 1995a). The ratio $\Delta t/\Delta t^* = l_c\left(C_L^*/C_L\right) \approx 10^{-8}\ s$ between the time interval (Δt) in *SI* unit and corresponding non-dimensional time interval (Δt^*) is, then, defined in terms of the physical (l_c, C_L) and non-dimensional ($l_c^* = 1, C_L^* = 7.5$) material properties. The ratio $\dot{\varepsilon}/\dot{\varepsilon}^* = \Delta t^*/\Delta t \approx 10^8\ s^{-1}$ between the strain rate in *SI* unit and non-dimensional strain rate is inversely proportional to the corresponding time interval ratio.

3.3.1 Uniaxial Tension Test

The particle dynamics simulations of the symmetric uniaxial-tension test were performed on the lattice (85 × 243 particles) with already defined parameters; it is noteworthy that the identical model parameters were used subsequently in the cavity expansion simulations (Section 3.4). The initial strain rate (velocity) fields are imposed on the lattice at $t = 0$. Afterwards, the controlled displacement is applied at the prescribed strain rate on the top and bottom edge of the lattice. The motion of all other particles is governed by Newton's equation of motion (2.2).

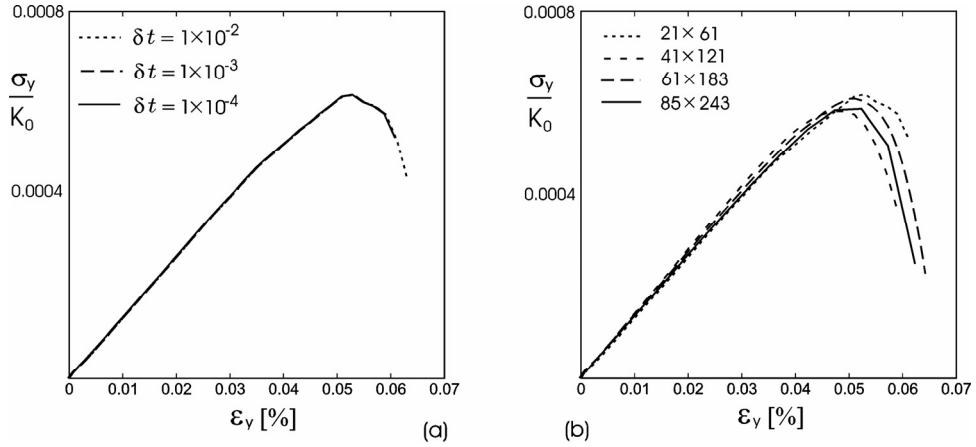

Fig. 3.22. Stress-strain curves recorded in the dynamic uniaxial test; (a) three different computational time steps, and (b) four sizes of the lattice (sample).

The initial estimate of the non-dimensional computational time step was based on the approximate expression used for the two-dimensional molecular dynamics simulations with Lennard-Jones potential $\delta t = 0.01$ (see Section 3.1). This initial

estimate of the non-dimensional computational time step is then reduced twice by an order of magnitude (i.e. to 0.001 and 0.0001) to check the objectivity of simulation results. The stress-strain curves recorded for all three computational time steps during the uniaxial tension test at a strain rate $\dot{\varepsilon} = 1 \times 10^4 s^{-1}$ are plotted in Fig. 3.22a. The three curves are practically identical. Hence, the computational time step $\delta t = 0.001$ is consistently used throughout this study. The only exceptions are the simulations at extremely high strain rates $\left(\dot{\varepsilon} = 1 \times 10^8, 1 \times 10^7, 1 \times 10^6, 6.7 \times 10^5 s^{-1}\right)$ where a smaller non-dimensional time step $\delta t = 0.0001$ must be used in order to obtain a sufficient number of data points prior to the sample failure.

The effect of the lattice size on the simulation results is studied by performing particle dynamics simulations on four sample sizes (21×61, 41×121, 61×183, and 85×243 particles) subjected to a controlled displacement applied at a strain rate $\dot{\varepsilon} = 1 \times 10^4 s^{-1}$. The stress-strain curves, plotted in Fig. 3.22b, exhibit the expected trend of strength decrease with the increase of specimen size. The ≈ 5% differences of the results are acceptable in view of widely different lattice sizes and consideration of a single physical realization. As expected, the differences are larger in the softening regime within which the lattice is not statistically homogeneous (Hansen et al., 1989; Krajcinovic and Basista, 1991). All of the following dynamic uniaxial-tension simulations are performed on the largest sample size (85×243) unless indicated otherwise.

The stress curves $\bar{\sigma}_y = f\left(\varepsilon_y\right)$ that sumarize results of 10 uniaxial tensile simulations during which the strain is applied at rates in the range $\left[10 s^{-1}, 1 \times 10^8 s^{-1}\right]$ are plotted in Fig. 3.23. Each curve corresponds to a single physical realization. The lateral stress component σ_x is equal to zero for all strain rates using the strategy explained in connection with Fig. 3.19. The out-of-plane normal stress in a three-dimensional isotropic continuum under the plane strain conditions , which corresponds to the two-dimensional triangular lattice used in these simulations, is $\sigma_z = \upsilon\left(\sigma_y + \sigma_x\right) = \upsilon\,\sigma_y$. The slope

$$E_0^{(\varepsilon)} = \frac{\sigma_y}{\varepsilon_y} = \frac{E_0}{1 - \upsilon_0^2} \tag{3.5}$$

of the $\sigma_y = f(\varepsilon_y)$ curve represents the modulus of elasticity of the two-dimensional plane-strain lattice (Monnete and Anderson, 1994). In (3.5) the traditional "three-dimensional" modulus of elasticity and Poisson's ratio, E_0 and υ_0, are the mechanical properties of pristine material. The perplexing change of modulus of elasticity, evident in Fig. 3.23, is an artifact of the extreme geometrical and, to a lesser extent, structural

disorder “quenched” in the lattice (Mastilovic, 2008, accepted) is not of primary importance for the present analysis (see Appendix D for details).

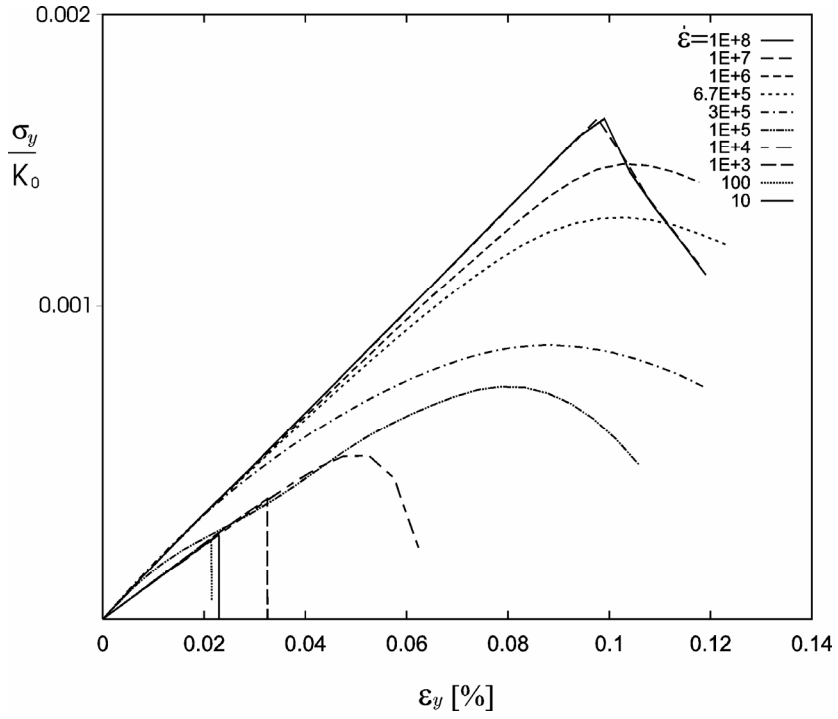

Fig. 3.23. Longitudinal stress plotted vs. longitudinal strain for 10 different strain rates.

According to Fig. 3.23 at very high strain rates ($1\times10^6 - 1\times10^8\ s^{-1}$) the strain at lattice failure is approximately equal to the bond failure strain $\varepsilon_{cr} = 0.1\%$. A reasonable interpretation of this phenomenon is that beyond a certain strain rate threshold the weak links (surfaces of inferior fracture resistance) do not have a significant influence on the material behavior. In other words, the material achieves its upper limit of strength determined entirely by the forces necessary to overcome its molecular cohesive energy. This intuitively appealing explanation, according to which the flaw-structure sensitivity of material depends on the rate of loading, is supported by the experimentally observed change of the fracture mode in alumina-based ceramics, which changes from intergranular to mixed intergranular and transgranular with the decrease of distance from principal spall plane (Louro and Meyers, 1989). Bao and Jin (1994) also concluded that if the “loading speed is quicker than the velocity of crack extension there will be no crack extension zone in fracture, and the effect of defects reaches the minimum. The fracture strength in this case is the upper

limit of the strength, which can be considered as the inherent strength, under the condition of admitting the existence of defects." However, it is well documented in the literature that the experimentally observed spall strengths of engineering ceramics are about two orders of magnitude lower than the theoretical strengths "indicating that the inherent or induced flaw structure of the material is crucial in determining the dynamic tensile strength of ceramics" (Grady, 1995a). One explanation for the lack of test measurements of the theoretical strength threshold is that the presently available experimental methods cannot produce a homogeneous strain rate of required magnitude.

3.3.1.1. Damage Evolution

The micro-mechanisms of damage evolution observed in the present simulations are the nucleation, propagation, and clustering of microcracks. As the damage evolves the effective macro-stiffness reduces. The rate of the effective-stiffness reduction, the level of the effective stiffness at failure, and the primacy of a particular damage micro-mechanism, are closely connected characteristics of material behavior that are strongly strain-rate dependent.

Four typical damage patterns are presented in Fig. 3.24. The damage patterns at high loading rates—represented by $\dot{\varepsilon} = 1 \times 10^8 \, s^{-1}$ in Fig. 3.24a—are characterized by a uniform microcrack distribution. (Note that the small lines represent the broken links.) The preferable microcrack surface orientation is, as expected, perpendicular to the loading direction. The typical microcrack cluster, at the onset of softening phase, consists of only a couple of broken links (e.g., from one to five), which are uniformly distributed throughout the sample. At that time, the characteristic distance between the clusters is commensurate with their size (Mastilovic et al., 2008). The final sample rupture is preceded by a relatively protracted softening phase (not discernable in Fig. 3.23, see Mastilovic et al. (2008) for details). The sample's load-carrying capacity is reduced to zero ($\varepsilon = 0$ and $\dot{\sigma} < 0$) after a period of time that is a couple of times longer than the duration of the hardening phase. (This inelastic behavior is a contrast to the low-strain-rate failure (Fig 3.24c) that is characterized by almost complete absence of the softening phase as evident in Fig. 3.23.) The fraction of broken links at the time of the sample failure asymptotically approaches the total fraction of links that are loaded in tension; this, within the limitations of the present model, resembles pulverization (comminution) of the material (Section 4.1). The kinetic energy of the sample, at this loading rate level, exceeds its potential energy by a few orders of magnitude (Mastilovic et al., 2008). The snapshot presented in Fig. 3.34a and the observation that the externally supplied energy overwhelms the cohesive energy of the

material, suggest that: (*i*) the dominant mechanism of damage evolution is the microcrack nucleation resulting in pulverization, and (*ii*) the role of cooperative phenomena in the damage evolution is unimportant (Mastilovic et al., 2008).

The change in the $\dot{\varepsilon} = 1 \times 10^4\ s^{-1}$ damage pattern (Fig. 3.34b), compared to the high strain-rate results presented in Fig. 3.34a, can be interpreted by an increasing influence of the microstructural disorder (the initial and induced flaw microstructure of the material) on the macroscopic material response. The microcrack clouds, which dominate the damage patterns at the end of softening phase of the $\dot{\varepsilon} = 1 \times 10^4\ s^{-1}$ simulation, consist of a large number of broken links. The clusters are elongated predominantly perpendicular to the loading direction; their length, in that direction, is typically between $(30 \div 40)\, l_c$ (Mastilovic et al., 2008). The clusters are uniformly distributed throughout the sample. The mutual distance between the largest clusters is commensurate to their size. This cluster map suggests the typical fragment size, which is larger substantially that the one corresponding to the $\dot{\varepsilon} = 1 \times 10^8\ s^{-1}$ simulation. This observation is in agreement with the prediction by Grady and Kipp (Grady, 1982) regarding the fragment size dependence on the strain rate (see also, Sarva and Nemat-Nasser, 2001). With the further reduction of the loading rate the number and size of, and mutual distance between, the dominant microcrack clouds reduces as well, implying further reduction of the fragment size. For example, for the $\dot{\varepsilon} = 1 \times 10^3\ s^{-1}$ simulation, the size of the dominant clusters is barely smaller for the damage patterns at the end of the relatively precipitous softening phase (at the onset of failure) from their $\dot{\varepsilon} = 1 \times 10^4\ s^{-1}$ counterparts, but the mutual distance between the clusters is increased substantially. The cooperative phenomena (reflected by the growth and coalescence of microcrack clouds) play an essential role in the fracture process and, ultimately, the sample disintegration mode (Krajcinovic and Mastilovic, 2001b).

With further reduction of the input energy (that is, further decrease of the loading power) the dynamic response of the material is distinguished by the localization of microcracks in only a handful of clusters; in the quasi-static case – in a single dominant cluster (Fig. 3.24c). The quasi-static tensile strength is, thus, controlled by a critical weak link (flaw, defect), and the failure macro-strain is a couple of times smaller than the critical micro-strain ($\varepsilon_{cr} = 0.1\%$); the difference being strongly dependent on the randomness of material microstructure. The material behavior and fracture is completely elastic-brittle, without a notable softening regime (Fig. 3.23). This marks transition from deterministic to random damage evolution patterns.

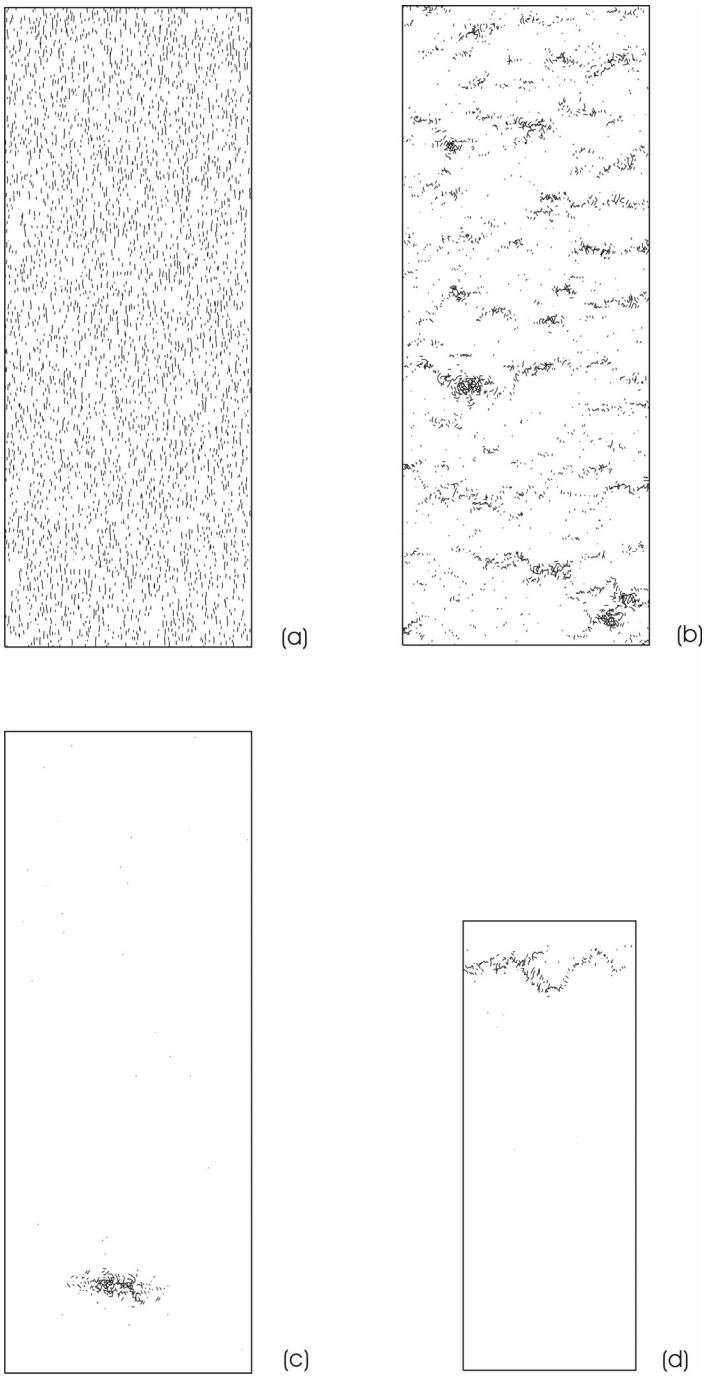

Fig. 3.24. Change of damage patterns with strain rate; (a) $\dot{\varepsilon} = 1 \times 10^{8} s^{-1}$, (b) $\dot{\varepsilon} = 1 \times 10^{4} s^{-1}$, (c) $\dot{\varepsilon} = 100 s^{-1}$ and (d) static loading.

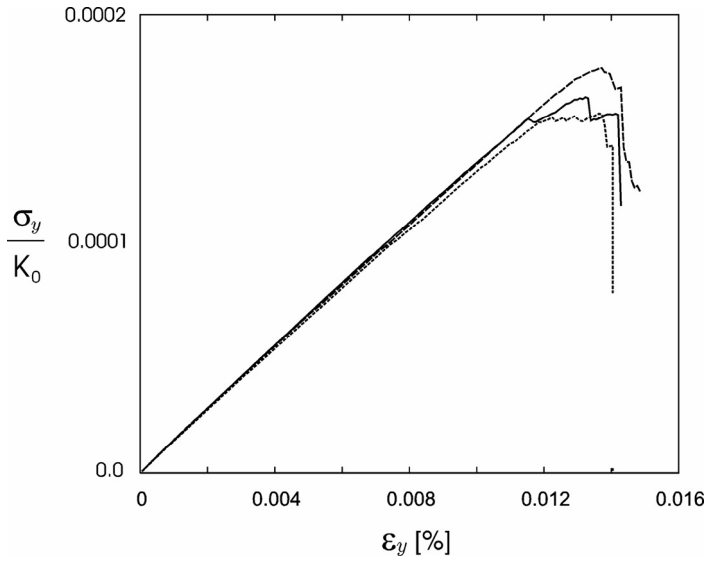

Fig. 3.25. Static stress-strain curves for three physical realizations of the same statistics

The static simulations are performed on a smaller lattice (59 × 143 particles) for the economy in computation (Mastilovic and Krajcinovic, 1999b). the material is statistically homogeneous through most of the hardening regime. The loss of statistical homogeneity, or transition from short- to long-range correlation length corresponds to the strain localization due to formation of a band characterized by a large density of ruptured links (Fig. 3.24d) (Rice, 1976; Lockner et al., 1991; Krajcinovic, 1996; Krajcinovic and Vujosevic, 1998). The first signs of the loss of homogeneity become visible before the peak of the stress-strain curve is reached (Van Mier, 1997). The resulting "evolution of microstructural disorder is a nonliner, nonlocal and non-deterministic process" (Vujosevic, 1996). In contrast to the high strain rate loading, the damage evolution modes during a static loading depend strongly on the microstructural disorder (weak links and stress concentrations). Consequently, the stress corresponding to the peak of the stress-strain curve is a random variable (Section 3.3.1.2) and the estimate of uniaxial tensile strength, $\sigma_m / K_0 = 1.67 \times 10^{-4}$ (Fig. 3.25), naturally involves a certain degree of arbitrariness (Mastilovic and Krajcinovic, 1999b).

Finally, the two phases of the damage accumulation, hardening and softening, are reflections of the primary mechanism of damage growth (Mastilovic et al., 2008). In the hardening phase the specimen is statistically homogeneous regardless of the

loading rate. The nucleation of microcracks at weak links (and hot spots, in general) is the paramount mechanism of damage evolution; the distances among microcracks are unlikely to be small, and the amplifying interaction effect of microcracks is insignificant. In the softening phase the specimen is, with notable exception of the upper-plateau loading rates, random heterogeneous. The damage process depends on the formation and interaction of large clusters, which is driven by the loading power. Signatures of the phase transition, close to the peak of the stress-strain curve, are the damage localization and the reduction of effective stiffness.

3.3.1.2. Dynamic Strength and Ordering Effect of Kinetic Energy

The strain rate dependence of the dynamic tensile strength, obtained from uniaxial tension simulations, is illustrated in Fig. 3.26. The simulation results are consistent with the experimental observations that suggest that at lower strain rates the strength is governed by the onset of fracture with modest strain rate sensitivity (Blanton, 1981). The steep ascent of strength with the increase of strain rate coincides with the transition of the fracture pattern from a single dominant macrocrack to the uniformly distributed microcrack clusters (Fig. 3.24). The high-strength plateau corresponds to a completely uniform distribution of microcracks.

A qualitatively similar "strain-rate strengthening" is experimentally observed in all brittle materials with disordered microstructure, namely in rocks (Brace and Jones, 1971; Green and Perkins, 1972), concrete (Ross et al., 1996) and ceramics (Lankford, 1981; Grady, 1995a). The existence of a high-strength plateau is discussed by Grady (1995a, b) in the context of the spall behavior inferred from energy-based theories on tensile failure of brittle solids. The increase of strength is related to the change in failure-damage mechanisms. The controversial nature of Hopkinson bar data at high strain rate loading, and the mixing of the uniaxial stress (Hopkinson bar) and uniaxial strain (planar impact) data renders the comparison difficult and the corresponding conclusions uncertain. The importance of the presented virtual experiment data is inherent to the fact that they are obtained under the same loading conditions, characterized by the vanishing lateral stress (Fig. 3.19), regardless of the applied strain rate.

Three qualitative observations can be made based on the stress-strain curves obtained for 30 realizations at low (1 s^{-1}) and high strain rates (1×10^{7} s^{-1}) (Mastilovic et al., 2008),

- the response is nearly linear up to failure for the low and the high strain rates, but not for the transient strain rates characterized by the rapid strength increase,

- the strain rate increase results in ascent of the dynamic tensile strength (σ_m),
- the strain rate increase results in diminished strength dispersion.

Table 3.1 presents statistics of the dynamic tensile strength describing these qualitative observations. The increase of the dynamic strength over the seven decades of the strain rate is sixteen times[15]. This general trend is well documented for wide range of engineering materials over the past three decades (e.g., Klopp et al., 1985; Zhou and Clifton, 1997; Grady, 1998; Sarva and Nemat-Nasser, 2001; Brara et al., 2001). Additionally, the strength increase is qualitatively similar to the strain-rate dependence of both the upper yield strength (calculated for ductile metals by Gillis (Gilman, 1969)) and the failure stress (modeled for ceramics under compression by Nemat-Nasser and Deng, 1994). It is interesting to note that, although the simplicity of the present model makes any quantitative comparison with experimental results a tentative undertaking, the ratio of the dynamic strength and the modulus of elasticity for the high loading rates $\sigma_m/E_0 \approx 1\times10^{-3}$ agree well with the ratio of the spall strength and the modulus of elasticity $\sigma_{sp}/E_0 \approx 1/1500–1/500$ compiled by Grady (1998) for several ceramic materials.

Table 3.1. Statistics of the dynamic tensile strength at four different loading rates[16]

$\dot{\varepsilon}$ [1/s]		1	10	1×10^3	1×10^5	1×10^7
σ_m/E_0 [$\times10^{-3}$]	MEAN	0.0649	0.0887	0.235	0.482	1.07
	STAND. DEVIATION	0.0147	0.0155	0.0115	0.00209	0.00185
	MAXIMUM	0.0975	0.112	0.252	0.487	1.07
	MINIMUM	0.0409	0.0615	0.204	0.478	1.07
	MAXIMUM / MINIMUM	2.55	1.94	1.32	1.08	1.07

The most important observation that can be made from Table 3.1 is the ordering effect of the kinetic energy on structure-sensitive properties, such as the dynamic strength (Mastilovic et al., 2008). Specifically, the standard deviation of the dynamic strength, as a measure of the data scatter, reduces almost by an order of magnitude

15 The strength increase is also dependent strongly on the level of microstructural disorder and the degree of nonlinearity of the link force under compression. The increase of β_l and γ_l reduces the ratio between the upper- and lower-strength asymptotes, and so does the reduction of the repulsive wall steepness (see Mastilovic and Krajcinovic, 1999; Mastilovic et al., 2008).

16 It should be emphasized that the strength scatter is dependent strongly on the level of microstructural disorder that Mastilovic et al. (2008) arbitrarily selected to be rather pronounced. The reduction of the microstructural disorder reduces the data scatter.

from 1 s^{-1} to 1×10^{7} s^{-1}. This observation again suggests that level of influence of the flaw structure of the brittle material on its dynamic behavior depends on the loading rate. In other words, the ordering effect of kinetic energy implies reduction of the microstructural sensitivity with the increase of the loading rate.

The dynamic tensile strengths are presented in Fig. 3.26; they correspond to the stress-strain curves obtained at 13 loading rates for the same statistical realization (i.e., for the same pseudo-random number generator seed) (Mastilovic et al., 2008). It is obvious from Fig. 3.23 that the dynamic strength approaches an upper asymptote for $\dot{\varepsilon} \approx 1\times10^{7}\ s^{-1}$. Indicatively, the ultimate tensile strength ($\sigma_m/E_0 \approx 1\times10^{-3}$) corresponds to the macro-strain of 0.1% that is identical to the failure micro-strain (i.e., the critical link extension, $\varepsilon_{cr} = 0.1\%$). Obviously, the more appropriate choice of the critical link extension (i.e., $\varepsilon_{cr} > 0.1\%$) would result in increase of failure macro-strains.

The scatter of the strength data for the five loading rates, presented in Table 3.1, is depicted by rectangular boxes in Fig. 3.26 (Mastilovic et al., 2008). The scatter box for $\dot{\varepsilon} = 1\times10^{7}\ s^{-1}$ is transformed into a horizontal dash, which is indicative of the substantial reduction of the dynamic-strength scatter at the high loading rates. This suggests that the theoretical strength, defining the upper limit strength, is a deterministic property defined primarily by the chemical bonding and relatively insensitive to the subtle features of the material texture.

The bilinear log-log plot presented in Fig. 3.26b is obtained by mapping the simulation data from Fig. 3.26a. The first linear region, corresponding to data points preceding the upper plateau (the upper strength asymptote), is described by the following scaling relationship between the uniaxial dynamic strength and the strain rate, $\sigma_m \propto \dot{\varepsilon}^{\zeta}$, where $\zeta = \Phi - \xi$, and Φ and ξ are parameters defined in Fig. 3.26b.

The results reveal the ordering effect of the kinetic energy on the dynamic response of the idealized brittle material reflected by transition from the random to deterministic behavior. This transition is evident in the reduction of the strength dispersion (Fig. 3.27) and damage evolution patterns discussed in Section 3.3.1.1. The schematic representation in Fig 3.37 indicates that the decrease in randomness of microstructure (either geometrical or structural) of brittle material results in increase in randomness of the material dynamic response reflected by the tensile strength scatter. This behavior can be explained by the increase of importance of complex interplay of microstructural features in the case of relatively narrow range of microstructural disorder.

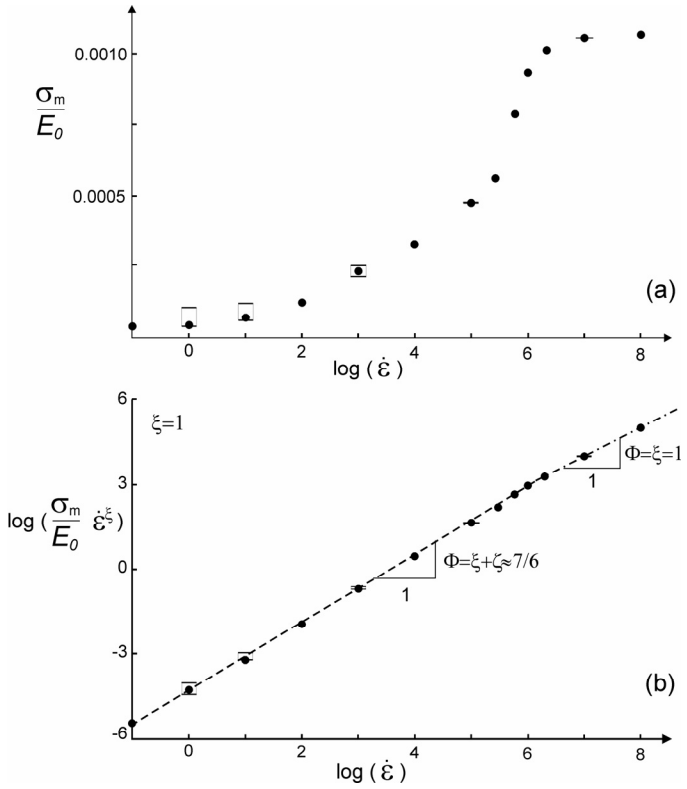

Fig. 3.26. Dynamic tensile strength vs. strain rate: (a) original plot, (b) scaled plot.

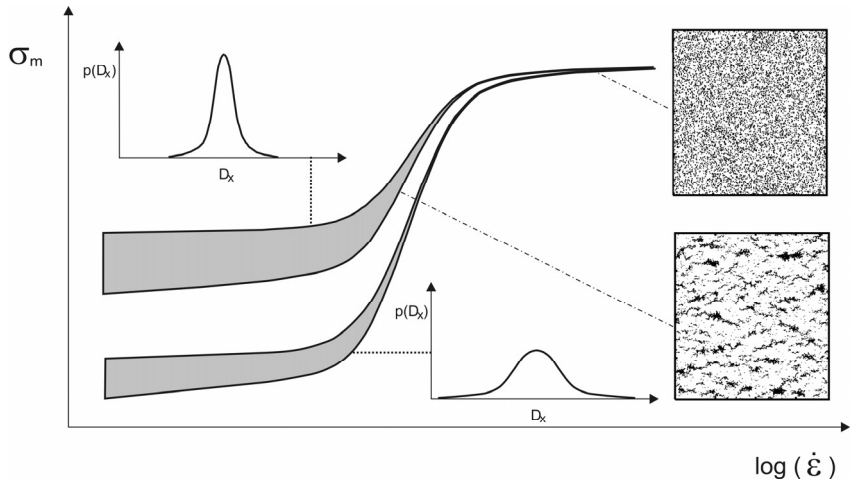

Fig. 3.27. Schematic representation of the dynamic strength dependence on the strain rate indicating the ordering effect of kinetic energy.

3.3.2 Biaxial Test

The simulation of a biaxial test is an extension of the previously discussed simulation of uniaxial tension. All biaxial simulations are performed within the particle dynamics framework. The narrow objective is to estimate the failure criterion parameters, namely the zero-pressure shear strength, τ_0, and pressure-shear coefficient, m_0, that are necessary input for the particle-dynamics model of a cavity expanding in an infinite elastic-brittle material (Section 4.1).

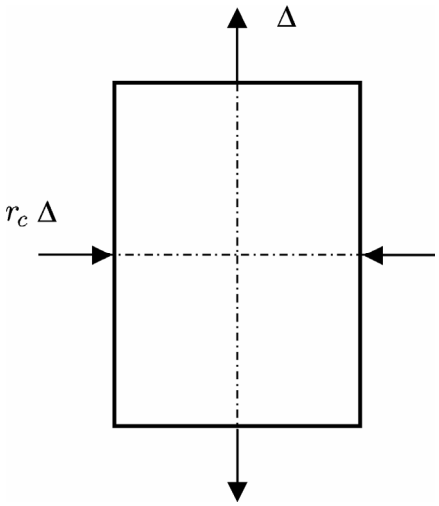

Fig. 3.28. Schematic representation of biaxial test set-up.

The rectangular two-dimensional specimen (101 × 117 particles) is subjected to the longitudinal elongation Δ combined with lateral contraction $r_c\Delta$ at prescribed strain rate (Fig. 3.28). Varying the contraction ratio r_c can enact any combination of pressure p and shear τ. Focusing on the determination of the initial damage surface $\tau_f = \varphi(p_f)$, i.e., the locus of points (p_f, τ_f) at which the first bond is broken in a pristine specimen, simulations are terminated when the first bond is broken. The damage surface deduced from these simulations, in the form of a slightly curved line in the shear-pressure space (Fig. 3.29a), is in good agreement with the tests performed on rocks (Paterson, 1978) and concrete (Van Mier, 1997). The degree of nonlinearity is dependent on the slope of the repulsive wall (parameter B in equation 2.16) but was, for all considered relations between link force and contraction, almost linear in the pressure range of interest. The damage surface turns out to be a straight line (solid line in Fig. 3.29b) for the assumed force-contraction relation ($B = 5$). The zero-pressure

shear strength and shear-pressure coefficient are estimated to be $\tau_0 = K_0/1000$ and $m_0 = 0.4$, respectively (Fig. 3.29b).

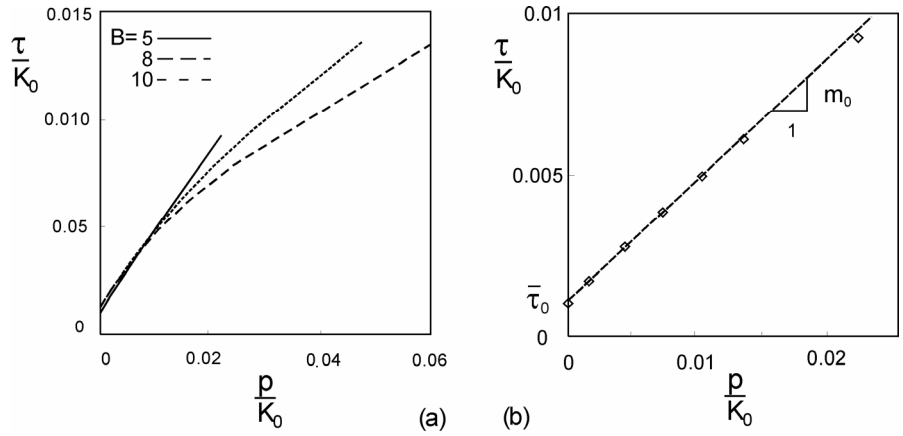

Fig. 3.29. Shear plotted vs. pressure; (a) for three different repulsive wall parameters, B, (b) estimate of failure parameters for $B = 5$.

Another set of biaxial test simulations is performed with objective to estimate the change of failure parameters across the interface separating the elastic and process regions (Section 4.1). The damage accumulated during this material transition across the interface, averaged over all regions, is estimated to be $n/N \approx 0.3$, where n is the number of ruptured links and N total number of links. The biaxial simulations are, therefore, performed on the specimen characterized by the same accumulation of the initial damage. The zero-pressure shear strength and shear-pressure coefficient are, under these conditions, estimated to be $\tau_0 = K_0/1240$ and $m_0 = 0.42$, respectively. Consequently, the change of the zero-pressure shear strength, corresponding to the initial damage $(n/N)_0 \approx 0.3$, is approximately 20%, while the shear-pressure coefficient is considered to be unchanged.

3.4 EXPANSION OF CYLINDRICAL CAVITY

The lattice simulations of a cylindrical cavity expansion are conceptually very simple. The cavity is nucleated by removing a single particle in the middle of the lattice. After the cavity is formed all particles that are located along the cavity perimeter are pushed away in radial direction at a desired (controlled) expansion rate $\dot{a}$. In this study the expansion rate $\dot{a}$ was fixed during the simulation. To eliminate the boundary effects as the cavity expands within an infinite medium, the simulation is interrupted when longitudinal elastic wave reaches the plate boundary.

The original lattice is divided into five annular regions of equal width (marked by letters *A* to *E* on Fig. 3.30) over which a particular field parameter or property are averaged. As the cavity expands the absolute widths of the annular regions shrink, but the relative widths are unchanged.

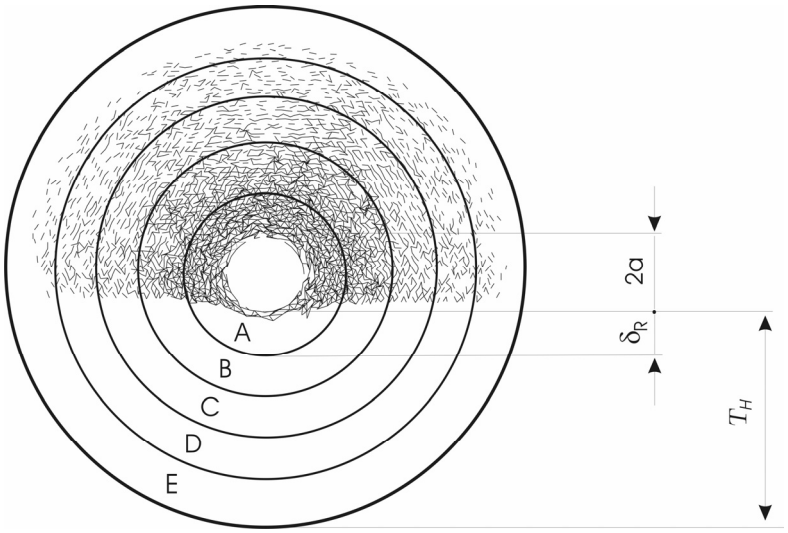

Fig. 3.30. Annular averaging regions for the evaluation of the field parameters in the particle dynamics simulations of the cylindrical cavity expansion within an infinite material.

The parameters recorded throughout the entire simulation within each annular region are: the position and velocity of each particle, the number of ruptured links, and the force in each link. The density of the isotropic damage is defined by the fraction of broken bonds *n/N*, where *n* is the number of broken bonds and *N* the total

number of bonds. Calculation of potential and kinetic energies in each annular region knowing the position and velocity of each particle is straightforward. In the case of kinetic energy summation is performed over all particles within the corresponding averaging area, $\mathcal{E}_{\mathrm{K}} = \sum m\left(v_x^2 + v_y^2\right)/2$, while for the calculation of the potential energy only non-broken bonds belonging to the annular region are taken into account $\mathcal{E}_{\mathrm{P}} = \sum F_{ij}\Delta\lambda_{ij}/2$. The cohesive or rupture energy, $\mathcal{E}_{\mathrm{D}} = (1/2)\sum k\lambda_0^2\varepsilon_{cr}^2$ is released during link ruptures.

The statistical mechanics expressions for the components of the stress (2.10) and effective stiffness (2.11) tensors are adopted from the conventional molecular dynamics. It is demonstrated henceforth that the agreement between the simulation results and available analytical solutions is reasonably good, although, in general, details of the data may be questionable for the non-equilibrium processes.

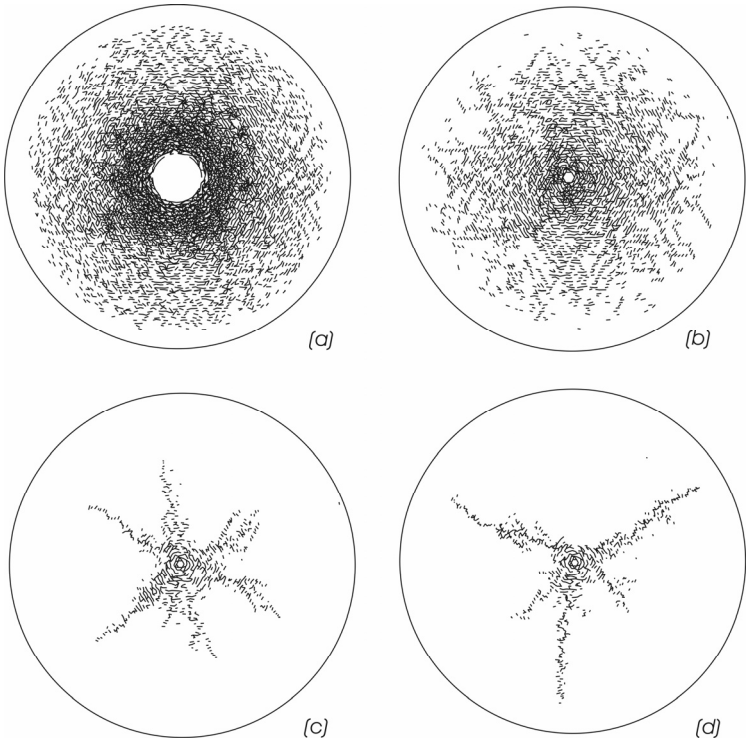

Fig. 3.31. Dependence of the damage evolution pattern on the cavity-expansion rate; (a) $\dot{a} = 0.135\,C_L$, (b) $\dot{a} = 0.0135\,C_L$, (c) $\dot{a} = 0.00135\,C_L$ and (d) $\dot{a} = 0.000135\,C_L$.

The simulations are performed for seven different cavity expansion velocities $\dot{a} = \varpi C_L$, where $\varpi =$ 0.135, 0.08, 0.04, 0.022, 0.0135, 0.007, 0.00135, while C_L is the velocity of longitudinal elastic wave propagation. The lattice model (101 × 117 particles) is defined by the same parameters used previously in Section 3.3.

The experimental observations (Strassburger and Senf, 1995) and simulations performed in this study indicate that the cracking pattern (damage evolution mode) is strongly dependent on the loading power. When the cavity expansion rate is below a critical magnitude (and the externally imparted energy is modest) the microcracks tend to localize into few macrocracks propagating in a radial direction away from the cavity (Fig. 3.31c,d). At cavity expansion rates in excess of the critical magnitude the material near the hole is shattered by the overwhelming imparted energy (Fig. 3.31a). It is obvious that the two deformation modes must be considered separately.

3.4.1 High-Velocity Cavity Expansion

The energy imparted to the target during the cavity expansion at high strain rate is so overwhelming that the force in each link exceeds the link strength. The energy consumed by rupture of links, distributed relatively homogeneously over large regions, is negligible compared to the imparted energy. The two most important features of the high-velocity cavity expansion are a rather large annular region of distributed damage, and the absence of the localization of damage into the well defined radial macrocracks. The entire surface of the plate, behind the elastic wave, can be divided into three regions: (*i*) comminuted (transformed or crushed) region closest to the expanding cavity, (*ii*) process region in the middle, and (*iii*) elastic region farthest away from the cavity (Fig. 3.31a).

Within the transformed (crushed or comminuted) region the damage is isotropic. The damage density tends to the limit of $n/N = 1$ (Fig. 3.36). According to the simulation results, the rate at which the front of this region propagates is (0.25 – 0.3) C_L, at the considered cavity expansion rate ($\dot{a} = 0.135\ C_L$).

The fraction of ruptured links, n/N, in the process region varies from 1 (at the interface between the transformed and process regions) to a zero (at the interface with the elastic region). The observed velocity of damaged-elastic interface propagation, (0.8-0.9) C_L, is in agreement with the reported experimental data related to the fracture in impacted sapphire (Senf and Winkler, 1997). The effective stiffness in circumferential direction degrades much more rapidly then that in the radial direction

(Fig. 3.32a)[17] since most of the damage is in this region attributable to radial microcracks. The rate of the radial stiffness reduction strongly depends on the radial distance from the cavity, while the circumferential stiffness degradation is characterized by two distinctive different rates that appear to be independent of the distance.

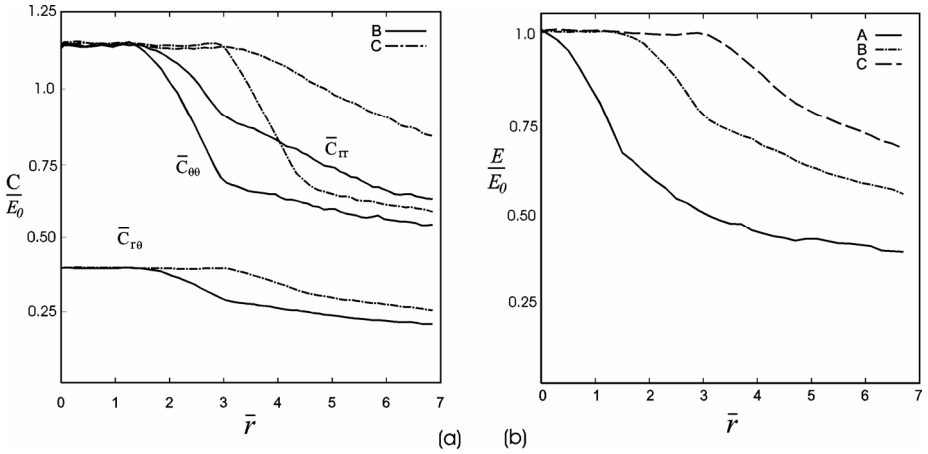

Fig. 3.32. Evolution of effective material properties; (a) stiffness components in annular regions *B* and *C*, and (b) Modulus of elasticity in annular regions A, B and C.

The deformation and damage patterns, in the case of a high velocity cavity expansion, reflect the ratio between the externally imparted energy and the cohesive energy of the links. The fraction of energy that is released during damage evolution (breaking of links) is negligible compared to the potential and kinetic energy. Hence, the imparted energy is balanced primarily by the kinetic energy of the transported material and the potential energy resisting the mass transport away from cavity (Fig. 3.33a). It is important to note the change in the relative contribution of the kinetic and potential energy with the change of the cavity expansion rate (Fig. 3.33).

[17] All figures in this section pertain to the largest velocity $\dot{a} = 0.135\, C_L$ unless specified otherwise. The presented results are average of ten physical realizations.

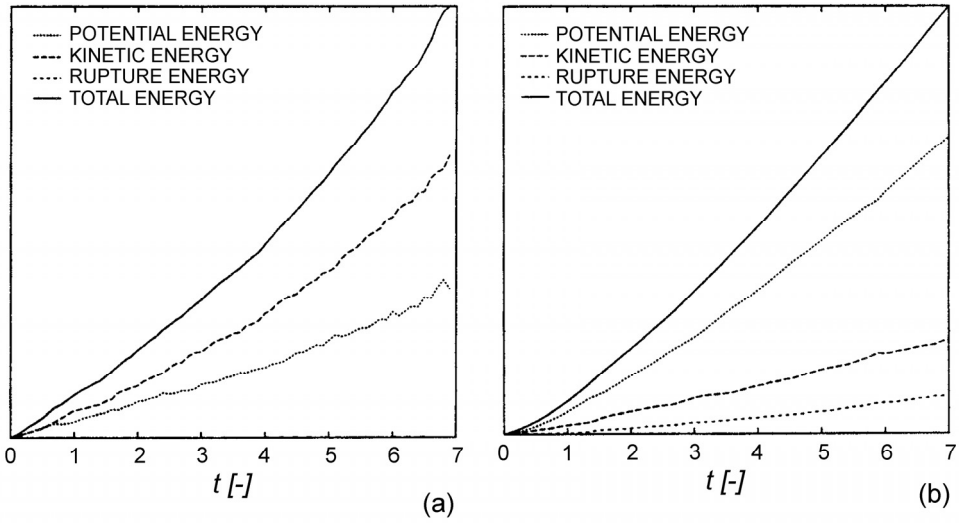

Fig. 3.33. Total, potential, kinetic and rupture energies during the high- and low-velocity cavity expansion; (a) $\dot{a} = 0.135\, C_L$ and (b) $\dot{a} = 0.00135\, C_L$.

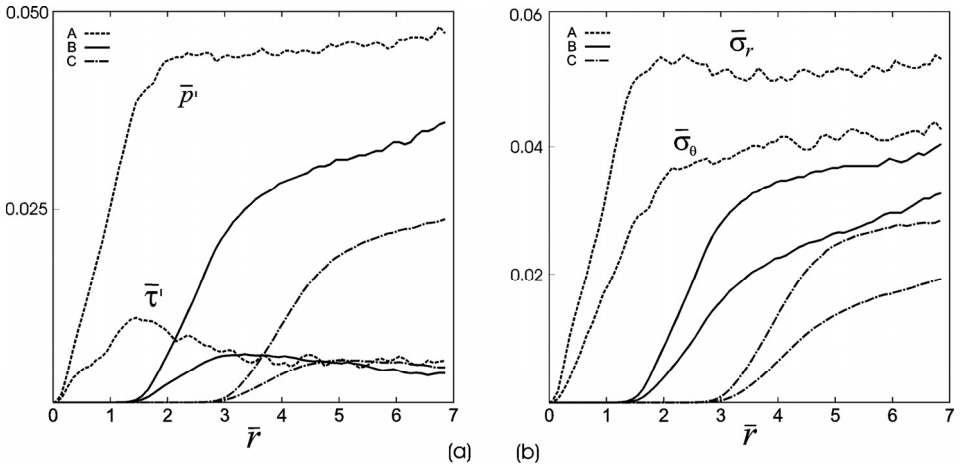

Fig. 3.34. Evolution of the stress state in three annular regions (A, B, and C) in the course of high-velocity cavity expansion; (a) mean normal stress (pressure) and principle stress difference (shear), and (b) stress components in radial and circumferential direction.

The radial σ_r and circumferential σ_θ stresses, and corresponding mean normal stress (pressure), $p' = (\sigma_r + \sigma_\theta)/2$, and principal stress difference (shear), $\tau' = (\sigma_r - \sigma_\theta)/2$, are plotted vs. time (or radial expansion of the cavity perimeter) in Fig. 3.34. In interpreting these data it must be reiterated that the stresses are averaged over the annular regions (Fig. 3.30). Hence these results are meaningful (statistical averaging is legitimate) only when the entire surface of the annular region belongs to the same regime. For example, a pronounced inflection point, beyond which the deformation process is characterized by the steady-state shear flow of material $\dot{\tau} = 0$, corresponds to the state at which the entire averaging region is covered by the process region.

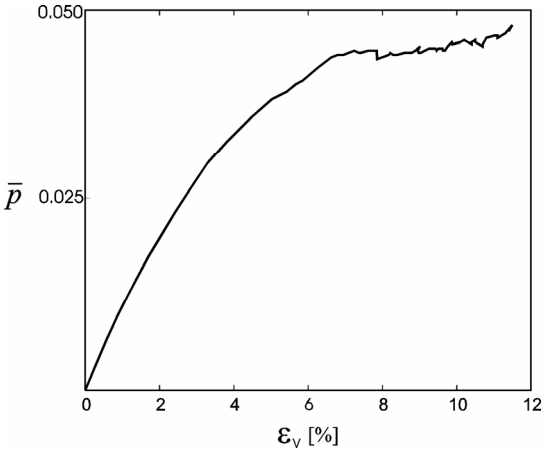

Fig. 3.35. Mean normal stress (pressure) plotted vs. volumetric strain in annular region A.

Two important observations follow from the relation between the mean normal stress and volumetric strain, $\varepsilon_V = \varepsilon_r + \varepsilon_\theta$, plotted in Fig. 3.35. Firstly, the commonly utilized assumption (Forrestal and Tzou, 1997) that the bulk modulus for the considered brittle material remains constant is correct only at relatively small volumetric strains $|\varepsilon_V| < 0.02$. Secondly, the onset of the large increase of strains, attributed to the considerable degradation of the effective bulk modulus, coincides with the beginning of steady-state shear flow $\dot{\tau} = 0$.

3.4.2 Low -Velocity Cavity Expansion

The deformation and damage pattern are entirely different in the case of the low-velocity cavity expansion. The energy imparted in the course of expansion at the rates smaller than critical rate, can crush material uniformly only within a small region closest to the cavity. Instead, at a critical distance from the cavity (which is a function of initial cavity radius) the damage localizes into several radial macrocracks. The three, clearly recognizable, regions shown in Figs. 3.31c,d are: (*i*) a thin annular region of uniformly distributed damage, (*ii*) a region within which the damage is localized into several macrocracks, and (*iii*) elastic region. According to the simulation results the macrocracks propagate with the velocity (0.25 – 0.35) C_L, which is in a reasonably good agreement with the results of the terminal crack velocity (Sieradzki et al., 1988; Zhou et al., 1996; Cox et al., 2005). The deformation pattern is in this case a reflection of the fact that the energy released during the damage evolution (link ruptures) represents a reasonably large fraction of the total externally imparted energy (Fig. 3.33b).

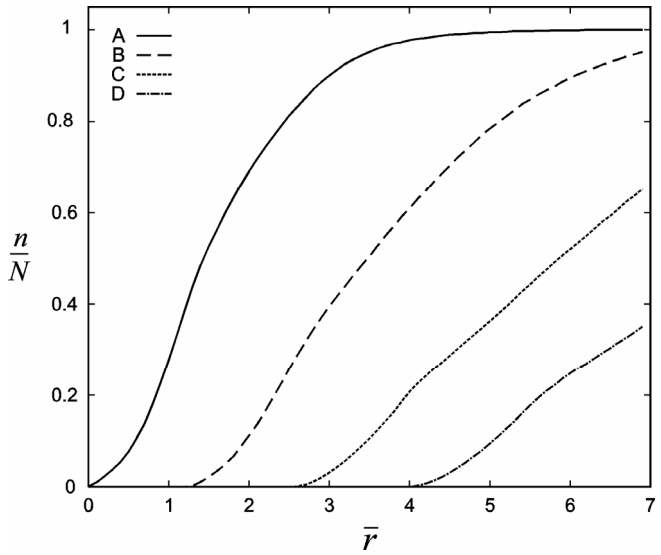

Fig. 3.36. Fraction of ruptured links in regions A to D plotted vs. non-dimensional change of the cavity radius.

3.4.3 Radial Traction at Cavity Surface

The estimates of the radial traction σ_r^c at the cavity perimeter is one of the most interesting and important aspects of this virtual experiment. This stress, related to the target resistance, is plotted vs. the nondimensional extent of expansion $\bar{r} = \Delta a / l_c$ in Fig. 3.37 for the seven considered cavity expansion rates. The examination of these plots clearly indicates that the two qualitatively different responses can occur for different cavity expansion rates. At a high rate cavity expansion, at which the damage is distributed and axially symmetric, the radial tractions σ_r^c that resist the cavity expansion are characterized by a sharp peak followed by a steep relaxation into a saturation state (of a much lower, constant stress) (Fig. 3.37a). The peak value of the radial traction is equal to the radial stress at the elastic wave front

$$\bar{\sigma}_r^F = \frac{\sigma_r^F}{K_0} = \frac{3(1-\upsilon_0)}{(1+\upsilon_0)}\left(\frac{\dot{a}}{C_L}\right) \tag{3.6}$$

at the cavity edge ($r = a$) (Kromm, 1948). The radial stress computed from (3.6), for three highest cavity-expansion velocities $\left(\dot{a}/C_L = 0.135, 0.08, 0.04\right)$, is labeled by small dots on the ordinate in Fig. 3.37a. The ratio between the saturation and peak stresses varies within a narrow band (0.32 – 0.36).

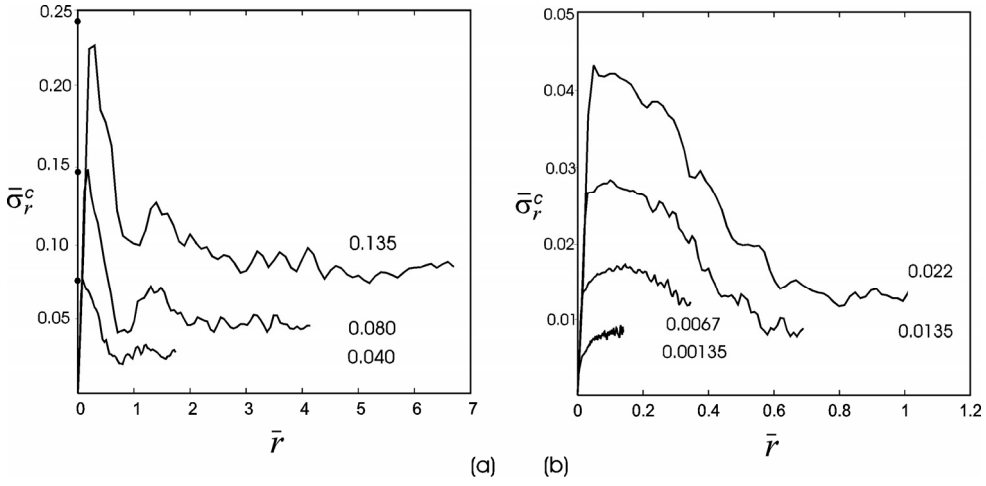

Fig. 3.37. Radial traction at the cavity surface vs. change of the cavity radius, for: $\dot{a} = \left(0.04 \div 0.135\right) C_L$ (a), and $\dot{a} = (0.00135 \div 0.022)\, C_L$ (b).

The saturation stress at high cavity expansion rates can be, therefore, approximated by a simple expression

$$\bar{\sigma}_r^c = \frac{\bar{\sigma}_r^F}{3} = \left(\frac{1-\upsilon_0}{1+\upsilon_0}\right)\left(\frac{\dot{a}}{C_L}\right) \tag{3.7}$$

At a modest rate of cavity expansion $\left(\dot{a} = 0.00135 C_L\right)$, the response is dominated by several macrocracks and the radial stress at the elastic wave front is relatively small. The radial traction σ_r^c increases slowly until it reaches from below the saturation plateau (Fig. 3.37b).

The evolution of σ_r^c at the highest cavity-expansion rate $\left(\dot{a} = 0.135 C_L\right)$ is plotted in Fig. 3.38a for four different force-contraction relations. The corresponding force-contraction relations are illustrated in Fig. 2.3. The linear Hookean model is labeled by *H*, while the nonlinear relations, based on expression (2.15), are labeled by the value of repulsive wall parameter, namely $B = 5, 8, 10$. The sensitivity of the peak stresses on the repulsive wall parameter *B* is again attributed to a very small number of atoms (six) forming the cavity perimeter at the simulation outset coupled with the disorder.

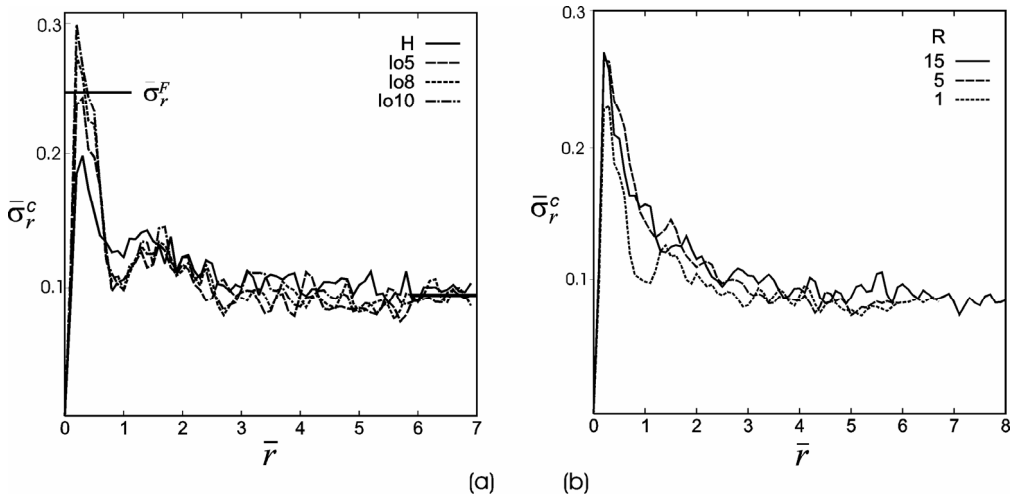

Fig. 3.38. Radial traction at the cavity surface vs. change of the cavity radius; for various (a) force-contraction relations, and (b) initial cavity radii.

As the cavity expands, the number of particles on its perimeter increases as some particles which were originally within the bulk emerge on the cavity surface. Averaging over a large number of particles along the expanded hole provides for a smoother stress evolution curve. This conclusion is supported by the fact that the saturation stress appears to be identical for all four force-contraction relations.

The computer simulations were also performed for three widely different initial cavity radii $\left(a_0 = l_c, 5l_c, 15l_c\right)$ at the highest cavity-expansion rate $\left(\dot{a} = 0.135 C_L\right)$. The objective of this investigation is twofold: (*i*) to examine the influence of the initial size of the cavity on the rate of stress transition from the peak to the saturation state, and (*ii*) to verify the effect of the size of the averaging sample. The size effect is manifested by the dependence of field properties and the radial traction at the cavity perimeter, on the number of particles at the cavity radius. An intuitive proposition, that the irregular, saw-tooth nature of stress evolution curve (Fig. 3.37) is caused by a small number of particles used in traction computation, is clearly confirmed by the simulation results plotted in Fig. 3.38b. As the number of particles forming the cavity rim increases, the crossover curve connecting the peak and saturation stresses tends to a smooth, exponentially decaying form. Furthermore, as the initial radius (i.e. averaging sample) increases, the peak stress obtained from the simulation data approaches the theoretical result (3.6) with $\approx 5\%$ error. At the same time the saturation stress remains unchanged. Finally, the simulation results plotted in Fig. 3.38b do not exhibit a notable difference in the rate and/or form of stress decay. This result is also consistent with the expression (3.6). Although the exponentially decaying crossover curve, for a large initial size of the cavity, is more aesthetically appealing, the results obtained for the numerical simulation with the smallest initial radius are presented herein for the sake of consistency with the analytical model to be formulated in the sequel.

Some of the more important observations that follow from the presented simulation results are that the radial traction σ_r^c at the cavity perimeter is: (*i*) relatively independent of the cavity expansion rate $\dot{a}$ for very small expansion velocities, and (*ii*) a linear function of $\dot{a}$ for the large expansion velocities (Fig. 3.39). Consequently, the relation between the radial traction at the cavity surface and the cavity expansion rate can be defined by determining only three data points. The first data point is provided by the static solution

$$\left(\frac{\sigma_r^c}{K_0}\right)_{st} = \left\{\frac{3\left(1-2\upsilon_0\right)}{\left(1+\upsilon_0\right)\left(3-2\upsilon_0\right)}\frac{\sigma_f}{K_0}\right\}^{1/2} \tag{3.8}$$

of fracture mechanics problem (Forrestal and Longcope, 1990). The expression (3.8) defines intercept of the curve $\sigma_r^c = f(\dot{a})$ with the ordinate (full circle in Fig. 3.39). Two remaining data points can be provided either by the approximate expression (3.7), for the saturation radial traction at the cavity surface that expands at large velocity, or by the analytical model developed in Section 4.1. Except for the closed-form static solution (3.8), only the high-velocity cavity-expansion results are used in this identification process since the axial symmetry of the deformation and damage at accompanying strain rates render corresponding solutions simpler, less random and, therefore, more reliable. When the solutions for the static and high-velocity cavity expansions are available, a functional relation $\sigma_r^c = f(\dot{a})$, necessary for the calculation of the depth of penetration, can be inferred by a simple curve-fitting using the corresponding data points. The detailed analysis is left for Section 4.2. At this point it is sufficient to mention that a common approach (Forrestal and Tzou, 1997)[18] is to use a second-order (quadratic) polynomial since it usually leads to a satisfactory approximation of test data. An alternative is to use a simple bilinear relation (solid line in Fig. 3.39) suggested by the preceding analysis. The horizontal part of this curve represents the response at small velocities of cavity expansion. The position of the horizontal line is fixed by the static solution (3.8), while the inclined straight line is defined by two data points obtained from high-velocity cavity expansion. Previously discussed transition from the localized to distributed damage occurs approximately within the shaded area in Figure 3.39. (The interception of the two straight lines defines the damage-mode transition velocity given by (4.19).) According to these virtual experiment data, the transition region is characterized by balance between the kinetic and potential (deformation) energy. On that point, it is interesting to note that Nakamura et al. (as cited by Anderson, 1991) used the equality of the kinetic energy and deformation energy to define a transition time between a short-time response (inertial effects are significant) and a long-time response (essentially quasi-static) of a dynamically loaded specimen.

To illustrate the concepts discussed above, Fig. 3.39 is plotted by using actual results. The data points marked by the hollow-square symbols correspond to the saturation radial stresses $\bar{\sigma}_r^c$ obtained directly by the particle dynamics simulations (Fig. 3.37). The analytical static solution, $\left(\bar{\sigma}_r^c\right)_{st} = 0.0086$, computed from (3.8), is labeled by a black circle. The tensile strength, $\sigma_m = K_0/6400$, used in computation of $\left(\bar{\sigma}_r^c\right)_{st}$, is estimated from the results obtained from the simulation of the static tensile test presented in Section 3.3.1. The results plotted in Fig. 3.39 are essential for the

[18] The analytical solution for the radial traction at the surface of the cavity expanding in an infinitely extended elastic-perfectly plastic material has the quadratic form.

modelling of penetration depth performed in Section 4.2 since they govern the forces of penetration resistance at the projectile nose.

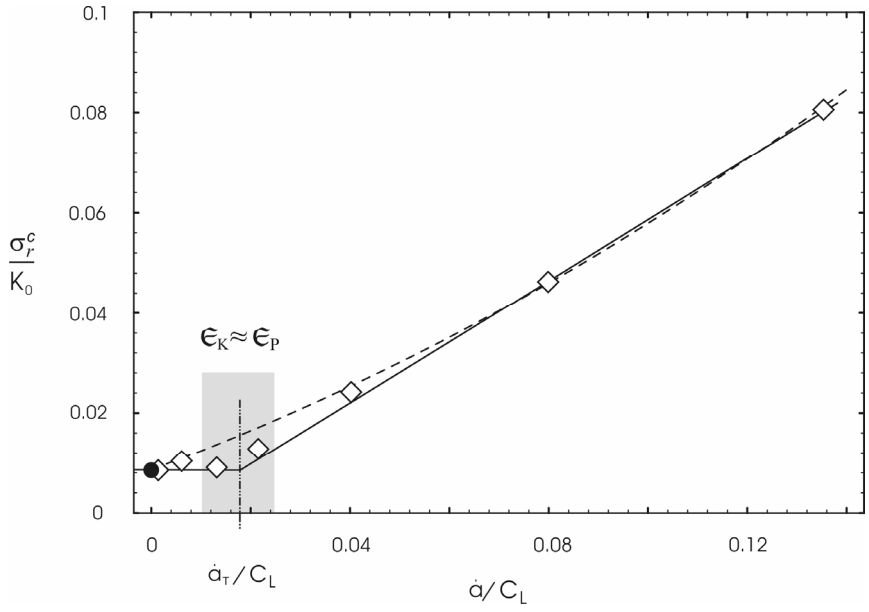

Fig. 3.39. Radial traction at the cavity surface vs. velocity of the cavity expansion. (Black circle marks the analytical static solution, the hollow squares mark the particle dynamics results.)

CHAPTER 4

ANALYTICAL MODELS

4.1 HIGH-VELOCITY EXPANSION OF A CYLINDRICAL CAVITY WITHIN AN INFINITE BRITTLE MATERIAL

The ultimate reason for performed numerical simulations is to provide a rational basis for analytical modelling of the high-velocity cylindrical cavity expansion for the axially symmetric, elastic-damaged-comminuted response pattern, based on the simulation observation and data presented in Chapter 3. Since the damage evolution in this case is dominated by the crack nucleation it is reasonable to assume statistical homogeneity of the material (Krajcinovic, 1996). Thus, traditional damage mechanics models should be applicable and the damage parameter could be approximated by a scalar $D = n/N$ (Krajcinovic and Mastilovic, 1995). The analytical model will at the moment be focused on the cylindrical cavity expanding with constant velocity $\dot{a}$ from zero radius through a brittle material with pressure dependent shear strength.

As discussed in Section 1.3, most of the numerical simulation methods in the field of high-velocity impact dynamics are founded on three conservation laws: conservation of mass, conservation of momentum, and conservation of energy. The equations of mass and momentum conservation written in cylindrical coordinates for an axially symmetric plane strain case, have the familiar form

$$\frac{\partial v}{\partial r} + \frac{v}{r} = -\frac{1}{\rho}\left(\frac{\partial \rho}{\partial t} + v\frac{\partial \rho}{\partial r}\right) \tag{4.1a}$$

$$\frac{\partial \sigma_r}{\partial r} + \frac{1}{r}(\sigma_r - \sigma_\theta) = -\rho\left(\frac{\partial v}{\partial t} + v\frac{\partial v}{\partial r}\right) \tag{4.1b}$$

where v is particle velocity (positive outward), σ_r and σ_θ radial and circumferential

components of Cauchy stress (positive when compressive), and ρ mass density. All stresses and velocities are related to the simulation data averaged over a sufficiently large surface area (see Fig. 3.30). Equations (4.1) are in the sequel specified for each of three regions (shown in Fig. 4.1) guided by the simulation data (see Mastilovic and Krajcinovic, 1999a).

4.1.1 ELASTIC REGION

The elastic region extends over the target surface between the elastic stress wave front $r = C_L\, t$ and the first link rupture front $r = x_D\, C_L\, t$. The stress-displacement relations in this region are

$$\sigma_r = \frac{-E_0}{(1-2\upsilon_0)(1+\upsilon_0)}\left\{(1-\upsilon_0)\frac{\partial u}{\partial r} + \upsilon_0 \frac{u}{r}\right\} \tag{4.2a}$$

$$\sigma_\theta = \frac{-E_0}{(1-2\upsilon_0)(1+\upsilon_0)}\left\{(1-\upsilon_0)\frac{u}{r} + \upsilon_0 \frac{\partial u}{\partial r}\right\} \tag{4.2b}$$

where u is radial displacement (positive outward), E_0 modulus of elasticity, and υ_0 Poisson's ratio of the pristine material. The application of linear elasticity is justified by the small critical elongations at which the links rupture.

The momentum equation (4.1b) for the elastic region is, using (4.2) and neglecting the convective term, transformed into the familiar form

$$\frac{\partial^2 u}{\partial r^2} + \frac{1}{r}\frac{\partial u}{\partial r} - \frac{u}{r^2} = \frac{1}{C_L^2}\frac{\partial^2 u}{\partial t^2} \tag{4.3}$$

The subsequent introduction of the similarity transformation $x = r/C_L t$, recasts the wave equation (4.3) into an ordinary differential equation

$$(1-x^2)\frac{d^2\bar{u}}{dx^2} + \frac{1}{x}\frac{d\bar{u}}{dx} - \frac{\bar{u}}{x^2} = 0 \tag{4.4a}$$

where $\bar{u} = u/C_L t$ is the dimensionless displacement (Hansen, 1964; Ames, 1965; Forrestal and Tzou, 1997).

The boundary value problem is completed by adding the boundary conditions along the propagating elastic stress wave

$$\bar{u}(x=1)=0 \tag{4.4b}$$

and elastic-process regions interface

$$(\sigma_r-\sigma_\theta)/2=\tau_0+m_0 p \qquad @\, x=x_D^+ \tag{4.4c}$$

to the wave equation (4.4a).

The boundary condition (4.4b) expresses an obvious requirement that the particle displacement vanishes at the elastic wave front. The condition (4.4c) along the elastic-process region interface requires that the shear stress becomes sufficient to cause the nucleation of the first crack (ruptured link) within the pristine elastic material. The Mohr-Coulomb form (4.4c) is often used for the fracturing of rocks (Paterson, 1978; Jaeger and Cook, 1979; Desai and Siriwardane, 1984; etc.). The parameters τ_0 and m_0, being the zero-pressure shear strength and pressure-shear hardening coefficient of the pristine material, are measured in tests. Relation of these parameters to the cohesive strength and friction is useful only in a qualitative sense.

The boundary value problem (4.4) can be solved by introducing two successive transformations $\bar{u}=x\xi$ and $\varphi=d\xi/dx$ (Forrestal and Luk, 1988). The solutions for the dimensionless radial stress $\bar{\sigma}_{r1}=\sigma_{r1}/K_0$ and velocity $\bar{v}_1=v_1/C_L$, in the elastic region, at the elastic-damaged interface $\left(x=x_D^+\right)$ are

$$\bar{v}_1=\frac{v_1}{C_L}=2A_e x_D\sqrt{1-x_D^2} \tag{4.5a}$$

$$\bar{\sigma}_{r1}=\frac{\sigma_{r1}}{K_0}=\frac{3A_e}{1+\upsilon_0}\left\{(1-2\upsilon_0)\sqrt{1-x_D^2}+x_D^2\ln\left(\frac{1+\sqrt{1-x_D^2}}{x_D}\right)\right\} \tag{4.5b}$$

where the constant

$$A_e=\frac{1+\upsilon_0}{3}\frac{\tau_0}{K_0}\left\{(1-2\upsilon_0)\sqrt{1-x_D^2}-\frac{2}{3}m_0(1+\upsilon_0)x_D^2\ln\left(\frac{1+\sqrt{1-x_D^2}}{x_D}\right)\right\}^{-1} \tag{4.5c}$$

depends on the parameters of the pristine material.

4.1.2 INTERFACE SEPARATING ELASTIC AND PROCESS REGIONS

Conservation of mass and momentum laws across the interface separating the elastic and process regions ($r = x_D C_L t$) require that

$$[\rho(v - V)] = 0 \tag{4.6a}$$

$$[\sigma_r + \rho v(v - V)] = 0 \tag{4.6b}$$

where brackets $[G] = G^+ - G^-$ stand for the magnitude of the discontinuity (jump) of the bracketed variable across the interface propagating with velocity $V = x_D C_L$ (Hopkins, 1960). Non-dimensional forms of Hugoniot jump conditions (4.6) are

$$\overline{\rho}_2(\overline{v}_2 - x_D) = \overline{\rho}_1(\overline{v}_1 - x_D) \tag{4.7a}$$

$$\overline{\sigma}_{r2} + \overline{\rho}_2\beta\overline{v}_2(\overline{v}_2 - x_D) = \overline{\sigma}_{r1} + \overline{\rho}_1\beta\overline{v}_1(\overline{v}_1 - x_D) \tag{4.7b}$$

where $\overline{\rho} = \rho/\rho_0$, $\beta = 3(1-\upsilon_0)/(1+\upsilon_0)$ while subscripts "1" and "2" denote the quantities on the elastic ($x = x_D^+$) and damaged ($x = x_D^-$) side of the interface, respectively. Hugoniot jump conditions (4.7) require that the particle velocity and radial stress are C^o continuous across the interface if the material density remains unchanged; that is, when $\rho_2 = \rho_1$.

At the damaged side of the interface between elastic and process region ($x = x_D^-$) the dimensionless radial stress and particle velocity read

$$\overline{v}_2 = \overline{v}_1 + (x_D - \overline{v}_1)(1 - \overline{\rho}_1/\overline{\rho}_2) \tag{4.8a}$$

$$\overline{\sigma}_{r2} = \overline{\sigma}_{r1} + \overline{\rho}_1\beta(x_D - \overline{v}_1)(\overline{v}_2 - \overline{v}_1) \tag{4.8b}$$

The constitutive description of materials on both sides of the interface between elastic and process regions has to be invoked to express $\overline{v}_2$ as the function of known physical quantities and material properties. The pressure-volumetric strain relation $p = K_0\,\varepsilon_V = K_0\,(1-\rho_0/\rho)$ is in the elastic region ($x_D \le x \le 1$) used together with failure criterion (4.4c). The constitutive description of the material on the damaged side of the interface ($x = x_D^-$), which accounts for degradation of the material properties due to the damage evolution by random microcrack nucleation, is

$$\bar{p} = \bar{K}\left(1 - 1/\bar{\rho}\right) \tag{4.9a}$$

$$\left(\bar{\sigma}_r - \bar{\sigma}_\theta\right)/2 = \bar{\tau} + m\,\bar{p} \tag{4.9b}$$

where $\bar{p} = p/K_0$ and $\bar{K} = K/K_0$. In general, the material parameters $\bar{\tau}$ and m are different from the corresponding pristine material parameters $\bar{\tau}_0$ and m_0.

The dimensionless particle velocity

$$\bar{v}_2 = \bar{v}_1 + \frac{\left(x_D - \bar{v}_1\right)\left\{1 - \bar{\rho}_1 + \bar{\rho}_1\left(\dfrac{1+\upsilon}{3\bar{K}}\right)\left[\left(1+\theta_1\right)\bar{\sigma}_{r1} - \theta_2\bar{\tau}\right]\right\}}{1 - \left(\dfrac{1+\upsilon}{3\bar{K}}\right)\left(1+\theta_1\right)\beta\left[\bar{\rho}_1\left(x_D - \bar{v}_1\right)\right]^2} \tag{4.10a}$$

and radial stress

$$\bar{\sigma}_{r2} = \bar{\sigma}_{r1} + \bar{\rho}_1\beta\left(x_D - \bar{v}_1\right)\left(\bar{v}_2 - \bar{v}_1\right) \tag{4.10b}$$

derived by combining equations (4.8) and (4.9), are needed for the numerical integration of the equation governing the deformation in the process region. In equation (4.10)

$$\bar{\rho}_1 = \left\{1 - \left(\frac{1+\upsilon_0}{3}\right)\left[\left(1+\theta_1^0\right)\bar{\sigma}_{r1} - \theta_2^0\bar{\tau}_0\right]\right\}^{-1}$$

and

$$\theta_1^0 = \frac{3 - 2\left(1+\upsilon_0\right)m_0}{3 + 2\left(1+\upsilon_0\right)m_0},\ \theta_1 = \frac{3 - 2\left(1+\upsilon\right)m}{3 + 2\left(1+\upsilon\right)m},\ \ \theta_2^0 = \frac{6}{3 + 2\left(1+\upsilon_0\right)m_0},\ \ \theta_2 = \frac{6}{3 + 2\left(1+\upsilon\right)m}.$$

are the material parameters on two sides of the interface separating the process and elastic regions.

Equations (4.10) are the initial particle velocity and radial stress needed for the numerical integration of equation (4.13) governing the deformation process in the process region.

4.1.3 PROCESS REGION

The deformation of the material within the process region ($x_C C_L t \le r \le x_D^- C_L t$) is completely defined by the conservation laws (4.1), constitutive equations (4.9) and evolution of effective material properties inferred from the simulation data. The deterioration of material properties (computed locally and averaged within the corresponding annular region; Fig. 3.30), attributed to the random nucleation of microcracks (distributed damage)

$$G = G_0(1 - \kappa D) \tag{4.11}$$

is assumed to be a linear function of the similarity variable x (Fig. 4.1). The linear dependence of effective material properties on damage, suggested by the self-consistent model, which typically holds well beyond the state at which the material ceases to be statistically homogeneous (Hansen et al., 1989; Krajcinovic and Basista, 1991; Krajcinovic, 1996), is often attributed (Kachanov, 1993) to the statistical balance of crack interaction reflected by shielding and amplification effects.

While the material is isotropic in both adjacent regions, the isotropy is violated in the process region. As shown in Fig. 3.32a the rate at which the components $\overline{C}_{\theta\theta}$ and $\overline{C}_{rr}$ decrease is obviously not identical. However, the complications related to this slight violation of isotropy are not commensurable to the perceived gain in accuracy and rigor.

The conservation laws

$$\frac{d\bar{v}}{dx} + \frac{\bar{v}}{x} = \frac{1}{\bar{\rho}}(x - \bar{v})\frac{d\bar{\rho}}{dx} \tag{4.12a}$$

$$\frac{d\bar{\sigma}_r}{dx} + \frac{1}{x}(\bar{\sigma}_r - \bar{\sigma}_\theta) = \bar{\rho}\beta(x - \bar{v})\frac{d\bar{v}}{dx} \tag{4.12b}$$

are derived from (4.1) using the similarity transformation $x = r/C_L t$ and introduction of dimensionless variables $\bar{v} = v/C_L$, $\bar{\rho} = \rho/\rho_0$ and $\bar{\sigma}_{\cdot} = \sigma_{\cdot}/K_0$.

The non-dimensional density and circumferential stress are eliminated from conservation laws (4.12) by using equations (4.9). The equations are derived, after lengthy but straightforward manipulations, in the form

$$\frac{d\bar{v}}{dx} = \frac{1}{\Re_p}\left\{\frac{\bar{v}}{x} - \bar{\rho}(x-\bar{v})\left[\Phi_p + \Xi_p - \mu_p(1+\theta_1)\Pi_p\right]\right\} \tag{4.13a}$$

$$\frac{d\bar{\sigma}_r}{dx} = \frac{1}{\Re_p}\left\{\Pi_p + \Delta_p\left[\frac{\bar{v}}{x} - \bar{\rho}(x-\bar{v})\left(\Phi_p + \Xi_p\right)\right]\right\} \tag{4.13b}$$

that is convenient for numerical integration, where

$$\mu_p = \frac{1+\upsilon}{3\bar{K}}, \quad \Phi_p = \{(1+\theta_1)\bar{\sigma}_r - \theta_2\bar{\tau}\}\frac{d\mu_p}{dx}, \quad \Xi_p = \mu_p\left(\frac{d\theta_1}{dx}\bar{\sigma}_r - \theta_2\frac{d\bar{\tau}}{dx} - \frac{d\theta_2}{dx}\bar{\tau}\right), \tag{4.13c}$$

$$\Pi_p = \frac{1}{x}\{(1-\theta_1)\bar{\sigma}_r + \theta_2\bar{\tau}\}, \quad \Delta_p = \bar{\rho}\beta(x-\bar{v}), \quad \Re_p = \bar{\rho}\,\mu_p\,(x-\bar{v})(1+\theta_1)\Delta_p - 1$$

The coupled system of two non-linear, first-order, ordinary differential equations (4.13) is integrated numerically for $\bar{v}$ and $\bar{\sigma}_r$ in the domain $\left(x_C \le x \le x_D^-\right)$. The boundary conditions for the numerical integration are the non-dimensional particle velocity and radial stress on the elastic-damaged interface (4.10).

4.1.4 TRANSFORMED (COMMINUTED) REGION

The comminuted (pulverized) material in the transformed region spanning the target surface between the cavity surface ($x_a C_L t$) and the transformed-process zones interface ($x_C C_L t$) is considered incompressible $\left(\bar{\rho}_c = Const. \Leftrightarrow \upsilon_c = 0.5\right)$ and unable to support shear stresses in absence of the confining pressure. Consequently, it can be modeled by a Mohr-Coulomb, non-cohesive material and the mass conservation equation (4.1a) reduces to an ordinary, first-order differential equation. The controlled rate of the cavity expansion, $\bar{v}\left(x = x_a\right) = x_a$, is the prescribed boundary condition. Consequently, the non-dimensional particle velocity is in the transformed region related to the dimensionless cavity-expansion velocity, $x_a = \dot{a}/C_L$, by a simple algebraic expression

$$\bar{v} = x_a^2/x \tag{4.14}$$

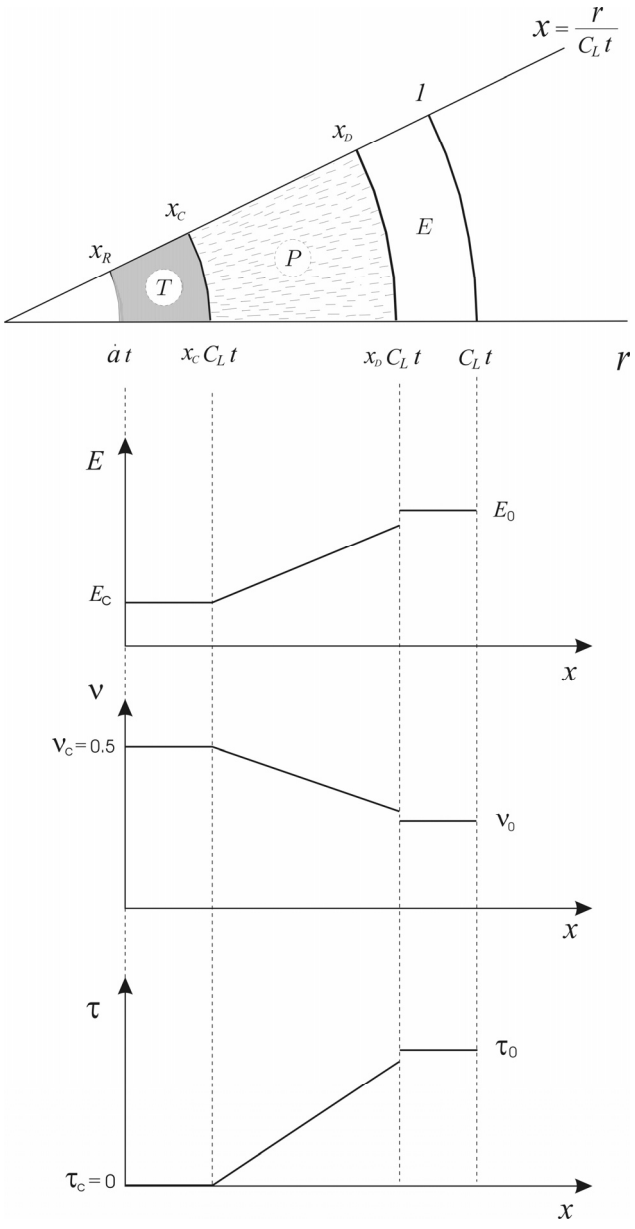

Fig. 4.1. Change of effective material properties and model parameters in the course of high-velocity expansion of cylindrical cavity within an infinite medium.

Combining the momentum conservation equation (4.1b) with the pressure-dependent flow criterion, $(\bar{\sigma}_r - \bar{\sigma}_\theta)/2 = m_c \bar{p}$, and knowing particle velocity (4.14), it is possible to derive a simple differential equation that can be solved analytically for $\bar{\sigma}_r$. The integration constant is evaluated from the already known value of the radial stress at the interface between process and transformed regions, $\bar{\sigma}_r(x = x_C) = \bar{\sigma}_{r4} = \bar{\sigma}_{r3}$. The subscripts "3" and "4" refer to the damaged $(x = x_C^+)$ and comminuted $(x = x_C^-)$ material along the interface. This boundary condition follows from the fact that the amount of damage continuously increases as the material within the process region smoothly transforms into the comminuted material. As the result of this smooth transition it is reasonable to assume that $\bar{\rho}_4 = \bar{\rho}_3$. Consequently, the Hugoniot jump conditions (4.5) require that the radial stress and particle velocity are continuous across the damaged-comminuted material interface. Finally, the dimensionless radial stress in the transformed (comminuted) region is

$$\bar{\sigma}_r = \bar{\sigma}_{r4}\left(\frac{x}{x_C}\right)^{-\gamma_t} + \xi_t\left[\frac{1}{m_C} + \left(\frac{x_a}{x_C}\right)^2\right]\left\{\left(\frac{x}{x_C}\right)^{-\gamma_t} - 1\right\} \tag{4.15}$$

where $\xi_t = \beta \bar{\rho}_C (1 + m_C) x_a^2/2$ and $\gamma_t = 2m_C/(1 + m_C)$.

The non-dimensional radial stress applied to the cylindrical cavity surface $(x = x_a)$ is, therefore,

$$\bar{\sigma}_r^0 = \bar{\sigma}_{r4}\left(\frac{x_a}{x_C}\right)^{-\gamma_t} + \xi_t\left[\frac{1}{m_C} + \left(\frac{x_a}{x_C}\right)^2\right]\left\{\left(\frac{x_a}{x_C}\right)^{-\gamma_t} - 1\right\} \tag{4.16}$$

4.1.5 SUMMARY OF COMPUTATIONAL PROCEDURE

The particle velocity and radial stress at the elastic side $(x = x_D^+)$ of the interface between elastic and process regions are evaluated using equations (4.5). The expressions (4.10) that define the basic unknowns $\bar{v}$ and $\bar{\sigma}_r$ on the opposite side of the interface $(x = x_D^-)$ provide the initial values for the numerical integration of the differential equations (4.13) governing the deformation within the process region $(x_C \le x \le x_D^-)$. The radial stress at the damaged-comminuted interface $(x = x_C)$ is evaluated by the integration of (4.13) and is, subsequently, used for the computation of the radial stress at the cavity surface $(x = x_a)$ by using equation (4.16).

In general, the value for the particle velocity, $\bar{v}_4 = x_a^2 / x_C$, at the damaged-comminuted interface obtained directly from equation (4.14), is slightly different from the one computed from the numerical integration of the equations (4.13). Therefore, it is necessary to adjust the positions of the process (x_D) and transformed (x_C) region fronts iteratively, until the continuity of the particle velocity at the interface is satisfied. The computed radial traction at the surface of the cylindrical cavity is independent of time and/or radius of the cavity.

4.1.6 NUMERICAL RESULTS

The governing equations (4.5) and (4.13) are solved numerically for the three highest cavity expansion velocities $\dot{a} = \varpi C_L$, where $\varpi = 0.135, 0.08, 0.04$, for which the stress, strain and damage fields are axially symmetric in statistical sense. The lattice properties are determined from the mechanical properties of the pristine material as shown in Section 3.4, and the model parameters are estimated from the simulation results discussed in Section 3.3.

The abrupt (discontinuous) change of the elastic properties of the material across the elastic-damaged interface is estimated to be $\approx 20\%$ judging from the evolution of the effective (volume averaged) modulus of elasticity and Poisson's ratio in the course of deformation process plotted in Fig. 4.2. The data presented in Fig. 4.2 cover the time interval starting from the beginning of simulation and end when the propagating damage front sweeps over the entire considered annular averaging region. Since the damage evolution is self-similar, approximately the same level of change of the material properties can be assumed for any arbitrarily small thickness of annular averaging. This intuitive notion is confirmed by the simulation results obtained by averaging over the regions half as thick (Fig. 4.3). The annular averaging region must be as thin as possible to capture the abrupt transition through the interface. On the other end, local fluctuations increase when the averaging regions are thin. In the absence of a resolution (or any other characteristic) length, traditional continuum theories predict the transition to be instantaneous.

In particle dynamics simulation the minimal thickness is limited by the model resolution length, i.e. the mean value of the distribution of distances separating the particles l_c. Unfortunately, a very small thickness of averaging volume would render the simulation results unreliable since a very thin area may not be statistically representative, i.e. exceptions of fields taken over such a small surface area will be dependent on the area size. Obviously, the accuracy of the estimate of the discontinuous change of material properties through the interface is a compromise

between conflicting requirements for the minimal thickness of the averaging region and a maximal size of the averaging sample. The optimal solution, in view of the presently available computer hardware, $\delta_R = 0.2T_H$ (Fig. 3.30), is consistently used throughout this study.

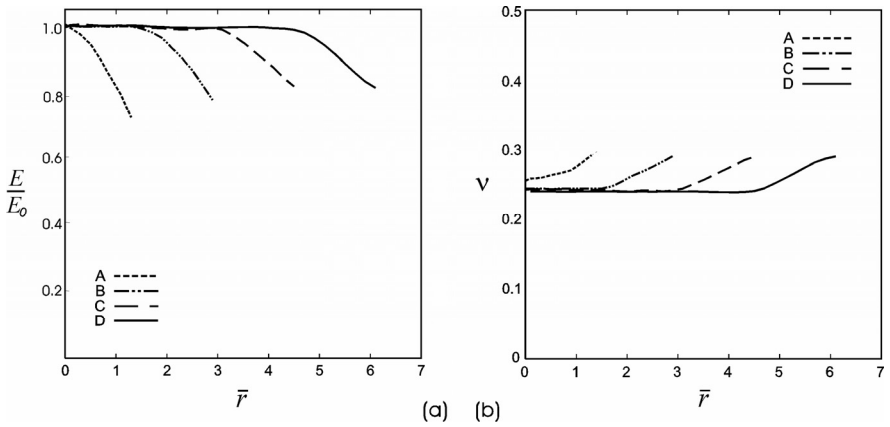

Fig. 4.2. Change of effective material properties across the interface between elastic and process region averaged over the four annular regions of thickness δ_R = 0.2 T_H; (a) modulus of elasticity, and (b) Poisson's ratio.

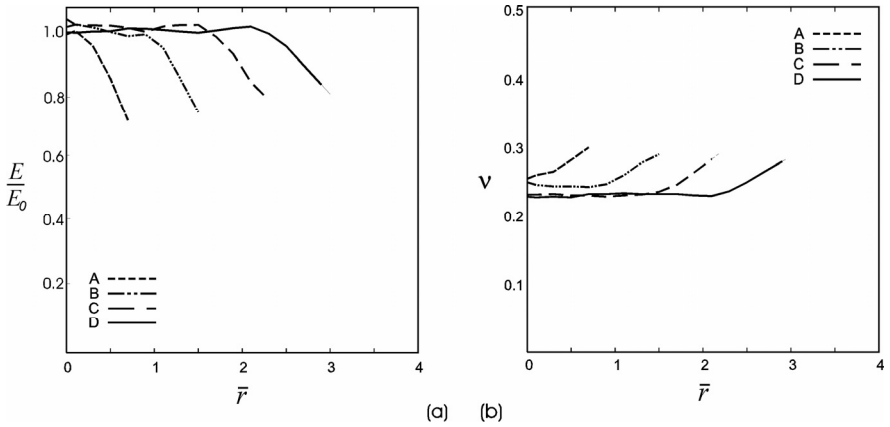

Fig. 4.3. Change of effective material properties across the interface between elastic and process region averaged over the four annular regions of thickness δ_R = 0.1 T_H; (a) modulus of elasticity, and (b) Poisson's ratio.

The discontinuity of magnitude of zero-pressure shear parameter τ_0 across the interface is estimated from the biaxial simulations, presented in Section 3.3.2, to be

$\approx 20\%$. According to these simulations the shear-pressure coefficient m_0 appears to be unchanged at the level of damage ($n/N \approx 0.3$) that accumulates during the abrupt material transition through the elastic-damaged interface. In the absence of any test results related to the change of shear-pressure coefficient in the course of deformation, the discribed virtual experiments remain the only source of data. Therefore, the numerical analysis is based on the premise that the shear-pressure coefficient remains unchanged during the entire process of cavity expansion, i.e. $m = m_0 = const$. It seems appropriate to emphasize that this is not a simplifying assumption in a usual sense, since the developed computer code can readily take into account the evolution of shear-pressure coefficient if necessary.

From the definition of incompressibility within the comminuted region Poisson's ratio is $\upsilon_c = 0.5$. The zero-pressure shear strength is assumed to vanish ($\tau_c = 0$) within this region since the comminuted material is non-cohesive. The corresponding value of modulus of elasticity $E_C = 0.45\ E_0$ is estimated from the stagnation level achieved for $n/N \approx 1$ (Fig. 3.32b).

The change of all effective material properties through the damaged region is assumed to be linear (Fig. 4.1). Therefore, the effective properties within this region are completely defined by the corresponding "boundary" values at the damaged side of the interface between the elastic and process regions $\left(x = x_D^-\right)$ and in the comminuted region. Finally, the initial locations of the process and transformed region fronts are $x_D = 0.85$ and $x_C = 0.25$.

The analytical results from the model (labeled by square symbols in Fig. 4.4) are compared with the particle dynamics cavity-expansion simulation data (solid line). Three target response regimes (linear elastic, crossover, saturization) can be clearly recognized. The minimum requirement is to determine the peak and stagnation values of the radial stress $\overline{\sigma}_r^c$.

The peak value of the radial traction is, as discussed above, provided by the analytical solution (3.6), which is surprisingly well supported by the simulation results. The saturation value of radial traction at the cavity surface necessitates a combination of the analytical and numerical computational procedure that is summarized in Section 4.1.5. The solution of corresponding boundary value problem provides an estimate of the stagnation value of the radial traction, which is independent of the time and/or extent of the increase of the cavity radius. According to results presented in Fig. 4.4, the agreement between the analytical model predictions and the simulation curves is very satisfactory.

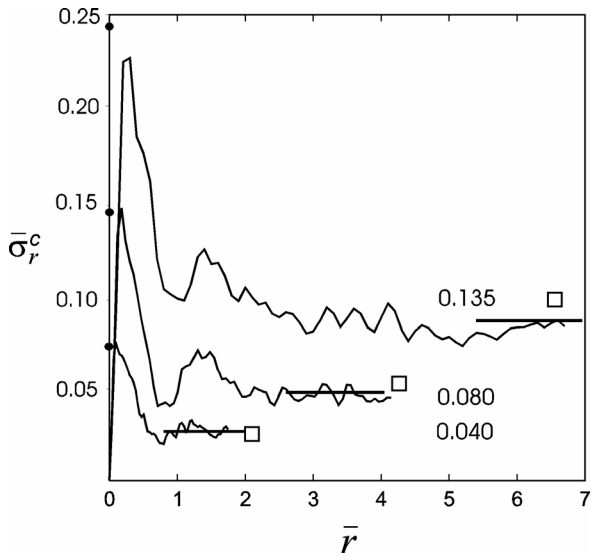

Fig. 4.4. Simulation (solid lines) and analytical results (dots and hollow squares).

The change of the particle velocity, radial stress and mass density across the target is, for the two highest cavity-expansion velocities $\dot{a} = 0.135\,C_L$ and $\dot{a} = 0.08\,C_L$, presented in Table 4.1 and Table 4.2, respectively. The characteristic radii, on which the state variables are computed, are: the elastic $\left(x = x_D^+\right)$ and damaged $\left(x = x_D^-\right)$ side of the interface between the elastic and process region, the interface between the process and transformed region ($x = x_C$) and the surface of the cavity ($x = x_R$). The positions of the process (x_D) and transformed (x_C) region fronts, presented in the tables, are obtained through the iterative procedure, outlined in Section 4.5, that provides continuity of the particle velocity and radial stress at the interface between process and transformed regions.

Table 4.1. Change of the particle velocity, radial stress and mass density across the target for the cavity expansion at velocity $\dot{a} = 0.135 C_L$.

	v/C_L	σ_r/K_0	ρ/ρ_0
$x = x_D^+ = 0.75$	2.37×10^{-3}	4.46×10^{-3}	1.002
$x = x_D^- = 0.75$	3.86×10^{-3}	5.96×10^{-3}	1.004
$x = x_C = 0.25$	0.0730	0.0606	1.106
$x = x_R = 0.135$	0.135	0.109	1.106

According to the results presented in the tables, the particle velocity, radial stress and mass density increase across the interface between the elastic and process regions, as expected. This discontinuous change of the state variables is followed by one order of magnitude larger increase in the process region. The change of particle velocity and radial stress across the much smaller transformed region is approximately the same as the one in the process region, while the mass density remains constant due to incompressibility of the comminuted material.

Table 4.2. Change of the particle velocity, radial stress and mass density across the target for the cavity expansion at velocity $\dot{a} = 0.08\, C_L$.

	v/C_L	σ_r/K_0	ρ/ρ_0
$x = x_D^+ = 0.68$	1.95×10^{-3}	3.74×10^{-3}	1.002
$x = x_D^- = 0.68$	2.46×10^{-3}	4.21×10^{-3}	1.0025
$x = x_C = 0.17$	0.0390	0.0330	1.049
$x = x_R = 0.08$	0.08	0.0600	1.049

The smaller imparted energy in the course of cavity expansion at velocity $\dot{a} = 0.08\, C_L$ compared to one at $\dot{a} = 0.135\, C_L$, is reflected through the twice smaller change of the mass density and the absolute and relative (compared to the corresponding size of the process region) decrease of the size of the comminuted region. The gradual decrease of the size of the transformed region is observed earlier in the particle dynamics simulation results. At the cavity expansion velocity of approximately $\dot{a} = 0.0135\, C_L$, the transformed region practically disappears, while the region of localized damage emerges at the outer boundary of the process region (Fig. 3.31b). It is intuitively appealing that the velocity of the damage front gradually decreases from the large fraction of the longitudinal elastic wave velocity (≈ 0.8–$0.9\, C_L$), characteristic of the damage front propagation at the high cavity-expansion rates, to about half of the Rayleigh wave velocity, characteristic of macrocrack propagation at moderate cavity-expansion rates. It should be emphasized, though, that the analytical model results, presented in Tables 4.2 and 4.2, predict more gradual transition compared to the particle dynamics simulation results.

4.1.7 SUMMARY AND CONCLUSIONS

Although this study focuses on material (intensive) aspects of the considered problem it cannot be overemphasized that the performance of the brittle targets depends strongly on their geometry and structure (Hauver, 1993). These, and other extensive, aspects of the problem are not addressed in this study. As demonstrated by the particle dynamics simulations in Section 3.4, in the case of large velocity cavity expansions considered in the present analytical model, the evolution of the radial tractions $\bar{\sigma}_r$ applied at the cavity rim passes through three different regimes. In the first, linearly elastic, regime the radial stress (traction) at the cavity perimeter increases linearly from zero to the peak value defined by the radial stress at the elastic wave front (3.6). During the second, crossover, regime the tractions needed to drive the cavity at a fixed rate diminish since the effective stiffness of the material decreases with the accumulation of damage that follows the inception and growth of the process region. In the third, saturization, regime the radial traction at the cavity surface reaches the stagnation value characteristic of every cavity expansion rate. The minimum requirement for a design method is to determine the peak and stagnation values of the tractions $\bar{\sigma}_r$.

It is important to recognize that all parameters of the proposed model are not only identified but also possible to determine by either physical or virtual experiments. First, the mechanical properties of a disordered two-dimensional central-force lattice (particle mass and mean link stiffness), utilized in Section 3.3, are determined from the corresponding properties of the pristine material. The mean link stiffness $\bar{k} = 8E_0/5\sqrt{3}$ is proportional to the plane strain modulus of elasticity E_0; the Poisson's ratio is fixed to $\upsilon_0 = 1/4$. The apparent plane-strain elastic parameters are related to the material properties by the relationships $E_0^{(\varepsilon)} = E_0/\left(1-\upsilon_0^2\right)$ and $\upsilon_0^{(\varepsilon)} = \upsilon_0/\left(1-\upsilon_0\right)$. The utilized distribution of link stiffnesses and strengths was selected somewhat arbitrary in the absence of complete test data. The parameters $\bar{\lambda}, \alpha_l$ are determined from the statistics of the grain and/or granular geometry. The structural-disorder parameter β_l depends on the distribution of residual stresses and their effect on the material strength. The critical link-rupture strain $\varepsilon_{cr} = 0.1\%$ is estimated based on the macroscopic rupture strain of the ceramics in static tests (Davidge, 1979). In hindsight of performed uniaxial tension simulations presented herein (Section 3.3), the link-rupture strain must be higher, $\varepsilon_{cr} \approx 0.5\%$, for the macroscopic rupture strain to be 0.1% under static conditions. The slope of the repulsive wall parameter B is conceptually related to the empirical coefficient S_1 in the

ballistic equation of state (3.2). Its identification, therefore, requires combination of the experimental and simulation data.

Second, regading the present analytical model, the strength parameters τ_0 and m_0 are estimated from simulations in which a rectangular two-dimensional lattice is subjected to the longitudinal tension combined with lateral compression at prescribed deformation rate (Section 3.3.2). The zero-pressure shear strength τ_0 is equal to the magnitude of the lattice shear stress $\left|\sigma_x - \sigma_y\right|/2$ at which the first link ruptures, in the lattice subjected to a load at which $p = (1+\upsilon_0)(\sigma_x + \sigma_y)/3 = 0$. The shear-pressure coefficient m_0 is defined by (4.4c) for an arbitrary biaxial state of stress (defined by various values of the ratio r_C, Fig. 3.28). In the considered case, $B = 5$, the shear pressure coefficient is constant and the initial failure (damage) curve plotted in the pressure-shear space is a straight line within a pressure range of interest (Fig. 3.29b). The nonlinearity, detected on higher pressures and for steeper repulsive walls of the potential, was commonly observed in the tests performed on rocks (Paterson, 1978) and concrete (van Mier, 1984).

The abrupt (discontinuous) change of material elastic properties across the interface separating the elastic and process regions is estimated to be ≈ 20% from the evolution of modulus of elasticity and Poisson's ratio (Fig. 4.2). During self-similar damage evolution, the change of the material properties is not dependent on the thickness of averaging region. This intuitive notion is confirmed by the simulation results obtained by averaging over different regions.

The discontinuities of the magnitudes of zero-pressure shear parameter τ_0 and pressure-shear coefficient m_0 across the interface are estimated from another set of biaxial simulations (Section 3.3.2, Fig. 3.28). These simulations are performed on the specimen with the initial ratio of ruptured links $n/N = 0.3$, that is estimated to be, on average, the accumulated damage during the material transition across the interface (Fig. 3.36). According to these simulations the abrupt (discontinuous) change of the magnitude of zero-pressure shear parameter is estimated to be ≈ 20%. On the other hand, the shear-pressure coefficient m_0 appears to be unchanged as the damage is abruptly increased from $D = n/N = 0$ to ≈ 0.3 during the passage through the interface separating the elastic from the process regions. In the absence of experimental data related to the change of shear-pressure coefficient the numerical analysis presented above is based on the premise that the shear-pressure coefficient remains unchanged during the entire process of cavity expansion, i.e. that $m = m_0 = const$. The Poisson's ratio in the comminuted region is taken to be $\upsilon_c = 0.5$ assuming the transformed material to be incompressible. The corresponding value of elastic modulus, estimated to be $E_C = 0.45\, E_0$ (Fig. 3.32b), is very close to the elastic modulus at the peak of the force-displacement curve for a lattice with the identical distribution of link strengths

(Krajcinovic and Basista, 1991). The change of all mechanical properties through the damaged region is, for simplicity, assumed to be linear (Fig. 3.39). The initial locations of the damage and comminuted fronts are $x_D = 0.85$ and $x_C = 0.25$.

Finally, the static uniaxial tension simulations ($r_C \equiv 0$) are performed to estimate the tensile strength (σ_m) of the pristine material. The stress-strain curves obtained from three different physical realizations of the same statistics are presented by Mastilovic and Krajcinovic (1999a). The stress corresponding to the peak of the curve is a random variable, due to the non-homogeneous material response in that region. The estimate of the uniaxial tensile strength, $\sigma_m/K_0 = 1.67\times10^{-4}$, is statistical in nature, which was vividly demonstrated by Mastilovic et al. (2008).

In conclusion, it appears that the proposed analytical model provides a realistic qualitative and quantitative picture of the considered process. Most of the micro-scale details were provided by Mastilovic and Krajcinovic (1999a) for the first time. Even the most important macrosopic distinction between the large and slow velocity of cavity expansion, and the underlying microscopic reasons for this distinction, have not been discussed in literature prior to that paper.

4.2 PENETRATION DEPTH

Despite its shortcomings, various modifications of the classical Tate-Alekseevsy model (Alekseevsky, 1966; Tate, 1967) remain the workhorse of continuum penetration mechanics. This model proved to be useful for estimation of penetration depth in metal targets. The reason for this longevity was that the deformation patterns of ductile targets exhibit universal trends (scaling similarity). Hence, the functional dependance of the target resistance of ductile metals on the strain and strain rate can often be deduced from experience with similar targets, projectiles, and impact rates (Mastilovic and Krajcinovic, 1999c).

The deformation of targets made of materials with inferior cohesive strength, which are predisposed to extensive cracking (i.e., damage accumulation) prior to failure, shows much more versatility and sensitivity to loading conditions. The response mode of brittle deformation of such materials depends not only on the crack density but also on the sign of the normal stress (thus the structure sensitivity), microstructural disorder, frictional slip of two mating crack surfaces, etc. In general, the deformation pattern of these materials during high-velocity penetration includes the transformed, process, and elastic regions, in order of their distance from the crater

(Fig. 4.1), as discussed in detail in Section 4.1. Briefly, the material of the transformed (comminuted) region is pulverized to the extent that the damage density approaches the maximum level (Fig. 3.36) and the deformation becomes similar to granular flow. The damage of the process region is substantial as the host of microcracks grow and self-organize into a densely packed multitude of shear bands (e.g., Fig. 3.31a).

The resistance of the target material to the cavity expansion and its capacity to absorb further the imparted energy without failure depends on the relative widths of of these three regions (Forrestal and Longcope, 1990; Mastilovic and Krajcinovic, 1999a,b). The widths of these regions depend not only on the external loading power but also on the microscale material disorder (i.e., damage tolerance). In absence of detailed micromechanical test data the present analytical model, aiming at the penetration depth estimate, relies on the virtual experiment data (i.e., the results of particle dynamics simulations presented in Section 3.4). Fig. 3.31 shows the damage patterns of the two-dimensional lattice for four different rates of void expansion: $\dot{a} = 0.135$, 0.0135, 0.00135, and $0.000135 C_L$; the damage evolution modes are discussed at length in Section 3.4.

The radial tractions at the cavity surface required for the cavity expansion at given rates are plotted in Fig. 3.37 versus the nondimensional cavity expansion. The peak values of radial tractions

$$\sigma_r^F = \frac{1-\upsilon_0}{(1-2\upsilon_0)(1+\upsilon_0)} \frac{E_0 \dot{a}}{C_L} \tag{4.17}$$

are derived from (3.6), which is obtained by solving the problem of stress wave propagation generated by the expansion of cylindrical cavity at constant velocity $\dot{a}$ within two-dimensional elastic plate (Kromm, 1948). In (4.17), E_0 and υ_0 are the modulus of elasticity and Poisson's ratio of pristine (damage-less) material, respectively.

The present alalytical approach relies crucially on the stagnation values of radial traction at the cavity perimeter, which can be determined from an analytical model based on the particle dynamics simulations and conservation principles (Mastilovic and Krajcinovic, 1999a). Analytical solutions are exhibited in Fig. 4.4 by small hollow squares. According to Fig. 3.39, the functional dependence of the radial traction σ_r^c (deduced from the simulation data) on the cavity expansion rate $\dot{a}$ can be approximated, with similar accuracy, either by a bilinear relation (solid line) or a quadratic parabola (dashed line). The intercept with the ordinate (the solid circle in Fig. 3.39) is the radial traction $(\sigma_r^c)_{st}$ at which the cavity perimeter starts to expand

quasi-statically in an infinite medium. Following Forrestal and Longcope (1990) and Mastilovic and Krajcinovic (1999a), these traction are

$$\left(\frac{\sigma_r^c}{K_0}\right)_{st} = \left[\frac{3(1-2\upsilon_0)}{(1+\upsilon_0)(3-2\upsilon_0)}\frac{\sigma_m}{K_0}\right]^{1/2} \tag{4.18a}$$

where σ_m is the uniaxial tensile strength of the material estimated by the quasi-static uniaxial tensile simulations (Section 3.3.1). Relation (4.18) of the bilinear approximation is valid for $0 \le \dot{a} \le \dot{a}_T = v_{nT}$, where the transition velocity v_{nT} is a material parameter. It is interesting to point out that the potential and kinetic energies are equal to each other at the transition velocity v_{nT} (Mastilovic and Krajcinovic, 1999a).

According to Mastilovic and Krajcinovic (1999a) relation between the peak value of the radial tractions (4.17) and the saturated value falls for all high expansion rates within a narrow range of [2.78, 3.12]. Assuming that the ratio is equal to 3, the inclined part of the bilinear approximation (Fig. 3.39), which is valid at large penetration velocities, is defined by

$$\frac{\sigma_r^c}{K_0} = \frac{\sigma_r^F}{3K_0} = \frac{1-\upsilon_0}{1+\upsilon_0}\frac{\dot{a}}{C_L} \qquad for\ \dot{a} \ge \dot{a}_T = v_{nT} \tag{4.18b}$$

The relation (4.18b) is a very good approximation of simulation data for the considered material characterized by reasonably large disorder (Mastilovic and Krajcinovic, 1999c).[19]

The transition velocity of cavity expansion $\dot{a}_T = v_{nT}$

$$\frac{v_{nT}}{C_L} = \frac{1+\upsilon_0}{1-\upsilon_0}\left[\frac{3(1-2\upsilon_0)}{(1+\upsilon_0)(3-2\upsilon_0)}\frac{\sigma_m}{K_0}\right]^{1/2} \tag{4.19}$$

follows straightforwardly from (4.18a) and (4.18b).

The quadratic parabola approximation, fitted from simulation data (Section 3.4), is

[19] Recall that a material is considered "disordered" if the random fluctuation of its micro-texture affects macroscale response (damage evolution).

$$\frac{\sigma_r^c}{K_0} = 0.0086 + 0.37\ \frac{\dot{a}}{C_L} + 1.25\left(\frac{\dot{a}}{C_L}\right)^2 \tag{4.20}$$

Expressions (4.18) and (4.20) are fitted by using the simulation data points for three different expansion rates $\left\{\dot{a}/C_L;\ \sigma_r^c/K_0\right\}=\ \{(0, 0.0086);\ (0.08, 0.046);\ (0.135, 0.081)\}$.

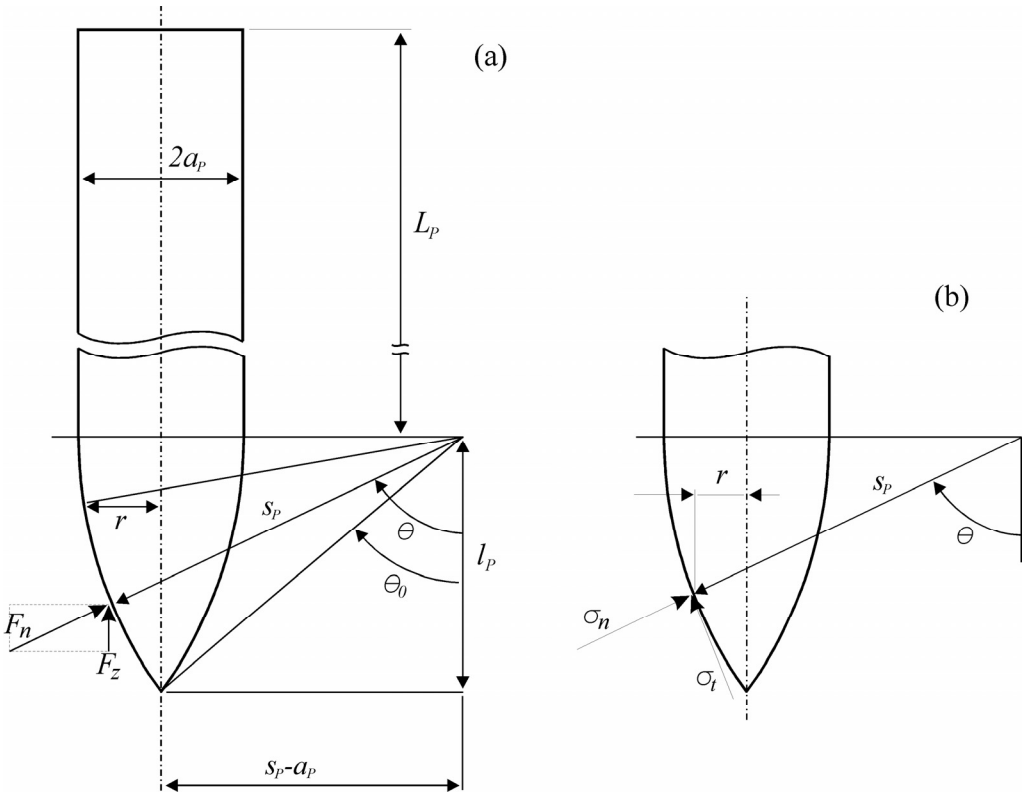

Fig. 4.5. Geometry of the ogival nose projectile (a), stress components at the ogival nose (b).

The largest difference between the bilinear and parabolic approximations of the simulation results shown in Fig. 3.39 corresponds to the transition from the localized to distributed damage pattern. The quadratic parabola provides a simpler model and requires only two tests (one static and one dynamic), assuming that the curve has a zero slope at the intersection with the ordinate. Since this transition depends on the microstructural disorder, it seems prudent to consider both bilinear and quadratic approxiamtions.

The ogive nosed projectile (Fig. 4.5) consists of a long shank and an ogive nose defined by a circular arc of radius s_P. The nose geomety is defined by

$$Sin\,\theta_0 = 1 - \frac{1}{2\psi_P} \quad where \quad \psi_P = \frac{s_P}{2\,a_P} \tag{4.21}$$

where a_P is the shank radius (Fig. 4.5). The tractions that resist penetration are outlined in Fig 4.5b. The infinitesimal force normal to the ogive nose surface is

$$dF_n = \left(2\pi\, r\, s\, d\theta\right) d\,\sigma_n \tag{4.22}$$

Following Forrestal et al. (1998), the relation between tangential and normal tractions applied to the nose is, in absence of experimental data, assumed to be related as

$$\sigma_t = \mu\,\sigma_n \tag{4.23}$$

where μ is a model parameter interpreted as a measure of friction.

The axial component of the resistance force

$$F_z = 2\pi\left(\frac{s_P}{a_P}\right)^2 a^2 \int_{\theta_0}^{\pi/2} \left(Cos\,\theta + \mu\, Sin\,\theta\right)\left(Sin\,\theta - Sin\,\theta_0\right)\sigma_n\, d\theta \tag{4.24}$$

is obtained from (4.22) and (4.23) after straightforward manipulation (e.g., Mastilovic and Krajcinovic, 1999c).

Following Forrestal and Luk (1988), the normal traction $\sigma_n\left(v_z, \theta\right)$ on the ogive nose is approximated by traction $\sigma_r^c\left(\dot{a}\right)$ needed to expand the cylindrical cavity at the rate $\dot{a}$, i.e., that

$$\sigma_n\left(\theta\right) = \sigma_r^c\left(r = a\right) \quad \text{and} \quad v_n = v_z\, Cos\,\theta = \dot{a} \tag{4.25}$$

Obviously, the assumptions (4.25) are, from the rigorous standpoint, geometrically incorrect since the cavity is not cylindrical, however, the error introduced by these mathematical simplifications is acceptable as argued by Bishop et al. (1945).

4.2.1 BILINEAR APPROXIMATION OF THE RADIAL TRACTION

Consider first the case when the relation between the radial traction at the cylindrical cavity surface and the expansion rate is approximated by the bilinear relation (4.18). The normal traction on the ogive nosed projectile are from (4.18), (4.24) and (4.25)

$$\bar{\sigma}_n = \frac{\sigma_n}{K_0} = \begin{cases} \left(\bar{\sigma}_r^c\right)_{st} = \left[\dfrac{3(1-2\upsilon_0)}{(1+\upsilon_0)(3-2\upsilon_0)}\sigma_m\right]^{1/2} = const. \quad for \quad v_n \le v_{nT} \\ \dfrac{1-\upsilon_0}{1+\upsilon_0}\dfrac{v_n}{C_L} = \dfrac{1-\upsilon_0}{1+\upsilon_0}\dfrac{v_z}{C_L}Cos\,\theta \qquad for \quad v_n \ge v_{nT} \end{cases} \tag{4.26}$$

The material parameter v_{nT}, defined by (4.19) , is from (4.25)

$$v_{nT} = \frac{1+\upsilon_0}{1-\upsilon_0}\left(\bar{\sigma}_r^c\right)_{st} C_L = v_z\, Cos\,\theta_T = \dot{a}_T \tag{4.27}$$

Therefore, if the penetration velocity exceeds v_{nT}, normal traction imparted to the lower part of the ogive nose corresponds to the case when damage is distributed (Fig. 3.31a). The normal traction at the upper part of the ogive nose, corresponds to the damage localized into several macrocracks (Fig. 3.31c,d). Hence,

$$\bar{\sigma}_n = \begin{cases} \left(\bar{\sigma}_r^c\right)_{st} = const. \qquad for \quad \theta_T \le \theta \le \pi/2 \\ \dfrac{1-\upsilon_0}{1+\upsilon_0}\dfrac{v_z}{C_L}Cos\,\theta \quad for \quad \theta_0 \le \theta \le \theta_T \end{cases} \tag{4.28}$$

where the angle

$$\theta_T = arc\,Cos\left[\frac{1+\upsilon_0}{1-\upsilon_0}\left(\bar{\sigma}_r^c\right)_{st}\frac{C_L}{v_z}\right] \tag{4.29}$$

that separates two tractions is derived from (4.27).

The angle θ_T (4.29) must satisfy two obvious conditions $-1 \le Cos\,\theta_T \le 1$ and $\theta_T \ge \theta_0$. At small penetration velocities, $v_z \le V_{nT}$, these conditions are satisfied if

$$v_z \le \frac{1+\upsilon_0}{1-\upsilon_0}\left(\overline{\sigma}_r^c\right)_{st}\left(1-\frac{1}{4\psi_P}\right)^{-1/2} C_L = v_{zT}, \quad \theta_T = \theta_0, \quad and \quad \overline{\sigma}_n = \left(\overline{\sigma}_r^c\right)_{st} \tag{4.30}$$

Conditions (4.30) are satisfied when the target deformation is quasi-static and $\overline{\sigma}_n$ is defined by (4.18a). In that case, the axial force component governing the target resistance is

$$F_z = 2\pi a_P^2 \psi_P^2 K_0 \left(\sigma_r^c\right)_{st}\left[1+\mu\left(\pi-2\theta_0\right)\right] + F_\Theta = F_{II} \tag{4.31}$$

where $F_\Theta = 4\left(1-a_P/s_P\right)\left(Sin\,\theta_0 - \mu\,Cos\,\theta_0 - 1\right) + Cos\,2\theta_0 + \mu\,Sin\,2\theta_0$ (Mastilovic and Krajcinovic, 1999c).

At large penetration velocities, defined as $v_z \ge v_{zT}$, the lower part of the ogive nose ($\theta_0 \le \theta < \theta_T$) is in the regime defined by $\mathfrak{E}_K \gtrdot \mathfrak{E}_P$ (the inclined part of the graph in Fig. 3.39), while the upper part ($\theta_T \le \theta \le \pi/2$) is in the regime defined by $\mathfrak{E}_K \lessdot \mathfrak{E}_P$ (i.e., $\sigma_r^c = const.$; Eq. (4.26)). The target resistance is

$$F_z = 2\pi a_P^2 \psi_P^2 \left[\frac{1-\upsilon_0}{1+\upsilon_0}\frac{v_z}{C_L} I_1 + \left(\sigma_r^c\right)_{st} I_2\right] = F_I \tag{4.32}$$

where

$$I_1 = K_0\left\{\mu\left[Sin\,\theta_T - Sin\,\theta_0 - \frac{1}{3}\left(Sin\,3\theta_T - Sin\,3\theta_0\right)\right] - \frac{1}{3}\left(Cos\,3\theta_T - Cos\,3\theta_0\right) - \left(Cos\,\theta_T - Cos\,\theta_0\right) - 2\left(1-\frac{a_P}{s_P}\right)\left(\theta_T-\theta_0\right) - \left(1-\frac{a_P}{s_P}\right)\left(Sin\,2\theta_T - Sin\,2\theta_0\right)\right\}$$

and

$$I_2 = 1 - 4\left(1-\frac{a_P}{s_P}\right)\left(1+\mu\,Cos\,\theta_T - Sin\,\theta_0\right) + \mu\left(\pi - 2\theta_T\right) + Cos\,2\theta_T + \mu\,Sin\,2\theta_T .$$

The penetration depth

$$D = m_P \left(\frac{v_{zT}^2}{2 F_{II}} + \int_{v_{zT}}^{v_s} \frac{v_z}{F_I} dv_z \right) \tag{4.33}$$

is obtained from Newton's second law (Mastilovic and Krajcinovic, 1999c). In (4.33), m_P is the projectile mass and v_s is the striking velocity.

4.2.2 PARABOLIC APPROXIMATION OF THE RADIAL TRACTION

Now lets consider the second case when the relation between the radial traction at the cylindrical cavity surface and the expansion rate is approximated by the quadratic parabola (Fig. 3.39)

$$\overline{\sigma}_r^c = A_1 + A_2 \frac{\dot{a}}{C_L} + A_3 \left(\frac{\dot{a}}{C_L} \right)^2 \tag{4.34}$$

Constants A_i (i=1,2,3) in expression (4.34) are obtained by using conditions

$$\overline{\sigma}_r^c \equiv \left(\overline{\sigma}_r^c \right)_{st}, \quad \frac{\dot{a}}{C_L} = 0$$

$$\frac{d\left(\overline{\sigma}_r^c \right)}{d\left(\dot{a}/C_L \right)} = 0, \quad \frac{\dot{a}}{C_L} = 0$$

$$\frac{d\left(\overline{\sigma}_r^c \right)}{d\left(\dot{a}/C_L \right)} = \frac{1-\upsilon_0}{1+\upsilon_0}, \quad \frac{\dot{a}}{C_L} = \left(\frac{\dot{a}}{C_L} \right)_{hv}$$

where subscript "*hv*" stands for high velocity and $\left(\dot{a}/C_L \right)_{hv} \approx 0.1$.

After easy manipulations the radial traction at the cavity surface is obtained in the following form

$$\overline{\sigma}_r^c = \left(\overline{\sigma}_r^c \right)_{st} + H_1 v_n^2 \tag{4.35}$$

where $H_1 = \dfrac{1-\upsilon_0}{2\left(1+\upsilon_0\right)} \dfrac{1}{C_L \dot{a}_{hv.}}$ (Mastilovic and Krajcinovic, 1999c).

The target resistance force can be derived by substituting (4.35) into (4.24) and performing rather straightforward but tedious integration.

The final form of the penetration depth is

$$D = \frac{m_P}{4\pi s_P^2 \beta_D K_0} \ln\left(1 + \frac{\beta_D}{\alpha_D} v_s^2\right) \tag{4.36}$$

where the two constants, α_D and β_D , are

$$\alpha_D = \frac{1}{4}\left(\bar{\sigma}_r^c\right)_{st}\left[1 + \mu(\pi - 2\theta_0) + 2\frac{1-2\psi_P}{\psi_P}(1 + \mu Cos\,\theta_0 - Sin\,\theta_0) + Cos\,2\theta_0 + \mu\, Sin\,2\theta_0\right]$$

and

$$\beta_D = \frac{1}{16}\frac{1-\upsilon_0}{1+\upsilon_0}\frac{1}{C_L\,\dot{a}_{hv}}\left[\frac{17}{12} - \frac{1}{3\psi_P} + \frac{\mu}{2}(\pi - 2\theta_0) + (1-2\psi_P)(3 + \mu Cos\,\theta_0) + Cos\,2\theta_0 + \frac{1-2\psi_P}{3\psi_P}(\mu Cos\,3\theta_0 - 9\,Sin\,\theta_0 - Sin\,3\theta_0) + \frac{1}{4}(Cos\,\theta_0 + \mu\, Sin\,3\theta_0)\right]$$

.

4.2.3 EXAMPLES

The concrete and limestone targets are appropriate examples not only because experimental data are available but also since the inelastic deformation of these two brittle materials is, under the conditions of the target confinement, almost always attributed to the damage in form of distributed microcracks.

The particular concrete and limestone considered are defined by the properties listed in Table 4.3.

Table 4.3. Properties on concrete and limestone used in two experiments.

	K_0 $[GPa]$	E_0 $[GPa]$	υ_0 $[-]$	σ_m $[MPa]$	ρ_0 $[kg/m^3]$	C_L $[m/s]$
Concrete [A]	6.7	11.3	0.22	13.0	2260.	2390.
Limestone [B]	22.	37.	0.22	5.0	2300.	4285.

Note: [A] Forrestal et al. (1996) and Forrestal and Tzou (1997).
[B] Green (1992) and Frew et al. (1996).

The penetration depth of an ogive nose rigid projectile (defined by the parameters listed in Table 4.4) through the two brittle materials are computed by using (4.33) and (4.36), for a range of striking velocity, and plotted in Fig. 4.6.

Table 4.4. Projectile parameters.

	m_P $[kg]$	a_P $[mm]$	ψ_P $[-]$
Concrete [A]	1.6	15.25	3.0
Limestone [B]	0.117	6.35	3.0

Note: [A] Forrestal et al. (1996) and Forrestal and Tzou (1997).
[B] Green (1992) and Frew et al. (1996).

These results are compared with the available test data for concrete and limestone (Forrestal et al. (1996) and Forrestal and Tzou (1997); and Frew et al. (1996), respectively). The computations are performed for two reasonable values of the fitting "frictional" coefficient. All other parameters used in computations can be directly measured in laboratory and *in situ*.

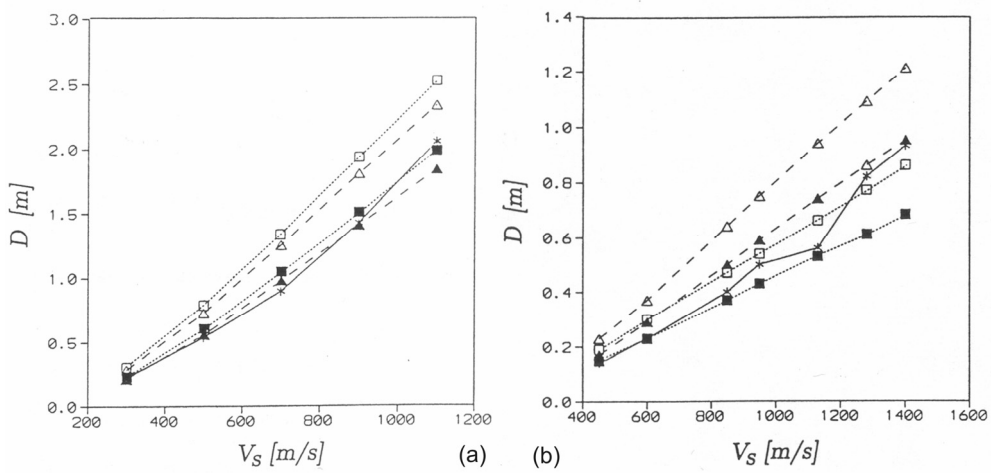

Fig. 4.6. Depth of penetration data (the solid line) for: (a) concrete, and (b) limestone. The model predictions are represented by: dotted lines - parabolic approximation, and dashed lines – bilinear approximation; asterix denotes the experimental data, full symbols correspond to $\mu = 0.2$ while the emtly symbols correspond to $\mu = 0.1$.

The deviations from the test data for concrete in the case of the bilinear model are from 18 to 33 percent for $\mu = 0.1$ and from –3.4 to 14 percent for $\mu = 0.2$. The parabolic approximation yield the similar results. The model accuracy, for the latter value of the frictional coefficient, is probably within the experimental scatter.

The deviations from the test data range for limestone in the case of the bilinear model are from 18 to 33 percent for $\mu = 0.1$ and from –3.4 to 14 percent for $\mu = 0.2$. Again, the model accuracy for $\mu = 0.2$ is satisfactory. The parabolic approximation seems somewhat more accurate for the higher striling velocities.

4.2.4 SUMMARY AND CONCLUSIONS

The objectives of the proposed analytical model are to identify the radial traction at the cavity rim needed to expand it at a given rate, to use it to determine the forces on the projectile nose with which the target resists the penetration of a conical projectile, and, finally, to estimate the penetration depth.

The peak value of tractions σ_r^F is given by the analytical, closed form solution (4.17) which is extremely well replicated by the simulations. The stagnation value of tractions $\overline{\sigma}_r$ (independent of time and cavity radius) is obtained by a numerical solution of the governing equations (4.5) and (4.13). This solution is also supported by the simulation data that oscillate about a constant value which is very close (see Fig. 4.4) to the numerical solutions for all three different cavity expansion velocities $\dot{a} = \kappa C_L$, $\kappa = 0.135, 0.08, 0.04$ for which the proposed continuum model is applicable.

The analytical model described in Section 4.2 is intentionally reduced to its simplest form. For example, the deformation of the projectile and the first elastic peak σ_r^F (4.17) of the target resistance (Fig. 4.4) are neglected. A simple relation between the elastic peak and stagnation radial straction, (4.18b), is used to render the model deterministic. The only fitting parameter μ (4.23) is assumed to be constant during penetration. The link properties (Fig. 2.6) are defined by a minimum of parameters related to material properties that can be measured in the laboratory (Section 4.1.7).

In general, it may be argued that the deterministic relation (4.18a) is a source of an unacceptable error. In this case the discrete system parameters reflecting microstructural disorder must be deduced from the experimental data (which were unavailable at the time this model was developed).

CHAPTER 5

FINALE

Dynamic fracture is a phenomenon that straddles a wide range of temporal and spacial scales. Consequently, keeping in mind limits imposed by computer capabilities, there is a clear need for formulation of a numerical technique that merges discrete and continuum descriptions. A typical penetration process is a catastrophic event characterized by large deformations and high strain rates. It encompasses the inertia effects, stress wave propagation, fracture, mass transport and phase transitions that takes place within few microseconds. This class of phenomena belongs to the category of nonlinear, nonlocal and non-equilibrium processes that cannot be considered using the traditional methods of the thermodynamics with internal variables. Moreover, the usual continuum concepts such as stress, strain and even temperature are at best conditionally applicable. In view of these complexities it may be that the objective of analytical models must be reduced to the estimates of the global parameters such as penetration depth, by using estimates of local fields formulated in a statistical form.

The strategy selected in the present study was to use the simulations of discrete systems (the molecular dynamics and particle dynamics) to: (*i*) acquire an insight into the micromechanical aspects of the considered problem, and (*ii*) identify and/or infer the material properties and model parameters necessary for the analytical modeling, (*iii*) formulate an analytical model to estimate peneration depth. Thus, the gist of the present study was to perform an investigation of the micromechanics of deformation and damage evolution observed in the virtual experiments on discrete systems to formulate a simple, approximate model of the considered high strain rate event. As a part of this effort, it is imperative to provide rational estimates of the radial traction at the surface of the cylindrical cavity expanding with constant velocity within an infinite brittle material with disordered microstructure and use it to obtain estimates of the penetration depth. This approach necessarily encompass investigation of universal trends in which the disorder and strain rate influence dynamic behavior of the idealized brittle material. The final objective, which might turn to be the most important, but remains evasive at present, is to provide rational constitutive relations for the design of hydrocodes.

The approach to the analytical modeling proposed in Sections 4.1 and 4.2 utilizes the particle dynamics simulations (Sections 2.2, 3.3, and 3.4) to acquire an insight into micromechanical aspects of the problem of dynamic loading of brittle materials with random microstructure and inferior tensile strength. The material of the target is characterized by the inferior tensile strength, pressure-dependent shear strength, and compressibility (prior to the comminution). Mindful of the fact that the lattice models are seldom, if ever, used in engineering design, where the quantitative accuracy is prerequisite, an attempt was made to ensure that each model parameter was clearly identified and related quantitatively to the material parameters measurable in either the laboratory or vitual experiments (Section 4.1.7). The geometric α_l and structural β_l disorder parameters were, in the absence of the detailed micromechanical data, selected in an approximative way, based on the guidance provided by available data. To emphasize the dearth of important data it suffices to mention that in most of the experimental studies of the impact and wave propagation phenomena in ceramic materials the average grain diameter is reported. Unfortunately, this datum is not followed by any additional informations, such as the size range in which the grains are distributed, not to mention the distribution itself or the estimate of residual stresses. Under such circumstances the geometrical disorder parameter α_l had to be selected to match, as close as possible, a visual image of the generic microstructural texture of materials observed on available micrographs. The choice of the particle dynamics simulations as a source of the macroscopic data was related to the fact that the simple and intuitively appealing constitutive relation (Fig. 2.6) is practically the only input; all other constitutive parameters are obtained from simulation or test data. Another favourable aspect of the particle dynamics model is related to the natural and simple introduction of the stochastic aspects of the microstructure, which is crucial to provide realistic patterns of damage nucleation and evolution. This analytical approach incorporates both aleatory variability and epistemic uncertainty in a straightforward manner, as discussed in Section 2.2. The simplicity of particle dynamic models and the corresponding economy in the computation time provides a basis necessary for the determination of universal trends. The fine resolution of this method eliminates, or at least alleviates, the problem of mesh-sensitivity. Finally, the important advantage of the discrete systems over the finite elements discretization approach is that the time consuming numerical schemes to track the material interfaces are not necessary.

The main difficulty in modeling a thermodynamically nonlinear, nonlocal and non-equilibrium process is directly related to the selection of rational constitutive models (assuming that they exist). Indeed, as discused at length throughout this study, one can even argue that the concepts of stress and temperature, let alone stiffness tensors, are of dubious utility in the considered case. The local values of stresses,

strain, particle velocity and damage may differ significantly from the volume averaged values. Ensemble averaging renders the graphs smoother and more pleasing to the eye. However, since there is no reason to believe that the considered class of problems is ergodic, any relation between volume and ensemble averages is of a qualitative nature. Nevertheless, in view of the fact that the primary objective of the present study was the determination of global properties, such as the resistance σ_r^c to the cavity opening (penetration) and corresponding penetration depth, it may be considered that the local fluctuations of stress, strain and damage fields are of limited importance. In other words, since the test indicate that the dependence of the resistance to the expanding cavity on the input parameters is surprisingly repeatable and orderly it was assumed that averaging of fields over rather large portions of the target is a reasonable strategy.

The particle dynamics simulations performed within a wide range of cavity-expansion rates vividly demonstrate the strain-rate sensitivity of a damage/fracture pattern. The recorded velocities of the macrocracks and damage front propagation were in excellent agreement with the experimental data. The transient evolution of the radial traction at the rim of the cylindrical cavity indicates that two qualitatively different responses may take place depending upon the velocity of the cavity expansion. At a high cavity-expansion rates, the damage is uniformly distributed and axially symmetric. The corresponding radial tractions σ_r^c were characterized by a sharp peak, followed by a steep relaxation into a saturation state. The peak values of the traction correspond to the radial stress at the elastic wave front at the cavity rim. Alternatively, at small rate of cavity expansion, the response is dominated by the propagation of several macrocracks. The radial stress σ_r^c increased slowly until it reached the saturation plateau from bellow.

Some of the more important observations deduced from the obtained simulation results were that the radial stress at the cavity perimeter is: (*i*) relatively insensitive to the cavity expansion rates at small expansion velocities, and (*ii*) a linear function of cavity expansion rate at the large expansion velocities. Consequently, the most important relation between the cavity expansion rate and the resistance to the expansion can be defined by determining only three data points. The first data point was provided by the static solution of the fracture mechanics problem, while the two remaining data points could be obtained by considering the high velocity cavity expansion problem by using either the analytical model results or the approximate expression following from simulations. This fact provide the rationale for the emphasis on the high-velocity cavity expansion in this study. Furthermore, the high-velocity cavity expansion is of primary interest in the design.

At the considered high cavity-expansion rates the nucleation of microcracks is the

prevalent failure mechanism rendering the deformation axially symmetric in a statistical sense. This axial symmetry of the deformation and damage renders the corresponding solutions simpler, less random and, therefore, more reliable. The accumulation of damage results in the gradual deterioration of the effective (volume averaged) material properties in the course of deformation process. The deterioration of effective material properties was, in the present investigation, considered as the continuous phase transition. The spatial extent of particular phases (elastic, process, and transformed) is defined by the velocities of propagation of corresponding fronts. The deformation regions grow in a self-similar manner since the material is assumed to be infinitely extended. Hence, the similarity theory is convenient to use in order to simplify the governing partial differential equations.

The deformation within each of three zones is, subject to the introduced assumptions, defined by the conservation of mass and linear momentum. The constitutive equations relating kinematic (strain and damage) and kinetic (stress) fields were carefully deduced from the simulation data. A rather delicate rearrangement of the governing nonlinear differential equations, subjected to boundary conditions, leads to a system of ordinary differential equations which is solved numerically for the resistance to cavity expansion.

The obtained estimate of the stagnation value of the radial traction at the cavity surface is independent of the time and/or cavity radius. The computed solution is consistent with the corresponding particle dynamics simulation data according to which the tractions along the rim oscillate about a constant value which is very close to the provided by the analytical model. The oscillations about the analytical solution attenuate if the data from a single simulation are replaced by the corresponding data averaged over an ensemble of simulations. The penetration depth analysis is intentionally reduced to its simplest form. For instance, the deformation of the projectile and the first elastic peak of the target resistance (see Fig. 4.4) are neglected. A simple relation between the elastic peak and stagnation levels of radial traction is used to render model deterministic. The only fitting parameter is the frictional coefficient μ is assumed to be constant. The link properties (Fig. 2.6) are defined by a minimum of parameters related to clearly defined and easy to determine material parameters. In view of this simplicity, the agreement of model predictions with experimental data for concrete and limestone (Fig. 4.6) is very encouraging.

Another goal of this work is to investigate universal trends in which the disorder and strain rate influence dynamic behavior of the idealized brittle material, by performing repeated lattice simulations for different physical realizations of the microstructural statistics. The dynamic simulations of the uniaxial tension test, $\dot{\varepsilon} \in \left[0.1\, s^{-1}, 1\times 10^{8}\, s^{-1}\right]$, are performed under practically identical stress conditions.

The results reveal the ordering effect of kinetic energy on the dynamic response of the idealized brittle material reflected by transition from the random to deterministic behavior. This transition is evident in the reduction of the strength dispersion and damage evolution patterns. The ordering effect of kinetic energy may be attributed to the diminishing flaw-sensitivity of brittle materials with the loading-rate increase. The flaw structure of the material (inherent and induced) is crucial in determining the dynamic tensile strength at low loading rates. With the increase of loading power, the dynamic strength is becoming increasingly a deterministic property defined by the chemical bonding. At high loading rates, the external energy overwhelms the cohesive energy of the material resulting in the pulverization. The corresponding uniformity of damage evolution patterns indicates an absence of the cooperative phenomena in opposition to the clustering of microcracks into microcrack clouds characteristic of the medium loading range. The evolution of the microcrack clouds may represent the dominant toughening mechanism in brittle materials not susceptible to dislocation activities. The effect of this process is reflected by the pronounced inelastic behavior not only in the softening but also in the hardening phase. These observations are reminiscent of Anderson's (1958) conclusions that: (*i*) localization is impossible in the absence of disorder and (*ii*) the localization range depends on the frequency and energy of electron waves. The reported discrete simulations can be correlated with experiments and used to pinpoint universal trends independent of the local fluctuations of stress and strain fields and the details of the microstructural disorder. In general, use of simulation data to formulate continuum model, require knowledge of universal trends characterizing the evolution of stress and strain and their relation to the modes of damage accumulation.

In conclusion, it seems that the proposed approach provides a realistic qualitative and quantitative picture of the considered process. A large number of useful micro-scale details of the deformation process are provided here for the first time. Nonetheless, is must be emphasized that there is an obvious limitation regarding the accuracy of the two-dimensional modeling of the physical phenomena. The spatial lattices may appear promising, especially keeping in mind that they suffer much less from the plane lattice homogenization drawbacks related to periodicity of two-dimensional molecular dynamic (nanoscale) models, but the extension to three dimensions may not be straightforward. Only the future research efforts may reveal whether the loss of simplicity is justified by potential gains in accuracy of quantitative description.

APPENDIX A

ELASTIC PROPERTIES OF TWO-DIMENSIONAL SYSTEMS

The Hooke's law for a three-dimensional isotropic material can be written as

$$\varepsilon_{11} = \frac{1}{E}\left[\sigma_{11} - \upsilon\left(\sigma_{22} + \sigma_{33}\right)\right] \quad \text{and} \quad \varepsilon_{12} = \frac{1+\upsilon}{E}\sigma_{12} \tag{A1}$$

along with four other similar expressions. In equation (A1) E and υ are the mechanical properties of the material, namely, the modulus of elasticity and the Poisson's ratio, respectively.

It is often convenient, when dealing with two-dimensional problems, to write the stress-strain relationship in the similar form

$$\varepsilon_{11} = \frac{1}{E^{(2D)}}\left[\sigma_{11} - \upsilon^{(2D)}\sigma_{22}\right] \quad \text{and} \quad \varepsilon_{12} = \frac{1+\upsilon^{(2D)}}{E^{(2D)}}\sigma_{12} \tag{A2}$$

where coefficients $E^{(2D)}$ and $\upsilon^{(2D)}$ are, formally, two-dimensional counterparts of the material properties E and υ. Obviously, $E^{(2D)}$ and $\upsilon^{(2D)}$ are nothing more then coefficients that are obtained by combining the actual material properties under the conditions of:

- the plane strain ($2D = \varepsilon$: $\varepsilon_{33} = \varepsilon_{13} = \varepsilon_{23} = 0$)

$$E^{(\varepsilon)} = \frac{E}{1-\upsilon^2} \quad \text{and} \quad \upsilon^{(\varepsilon)} = \frac{\upsilon}{1-\upsilon} \tag{A3a}$$

- the plane stress ($2D = \sigma$: $\sigma_{33} = \sigma_{13} = \sigma_{23} = 0$)

$$E^{(\sigma)} = E \quad \text{and} \quad \upsilon^{(\sigma)} = \upsilon \tag{A3b}$$

Specifically, for the plane-strain problem with the constraint imposed in the homogeneous simulation setup:

$$\sigma_{22} = 0 \quad \Leftrightarrow \quad \varepsilon_{22} = -\upsilon^{(\varepsilon)}\, \varepsilon_{11} = -\frac{\upsilon}{1-\upsilon}\varepsilon_{11} \tag{A4}$$

the slope of the $\sigma_{11} - \varepsilon_{11}$ curve is $E^{(\varepsilon)} = E/\left(1-\upsilon^2\right)$.

The plane-strain stiffness components are sample-average quantities obtained in the usual molecular dynamics manner (Vitek, 1996) during simulations. Hence, it is convenient to express the elastic constants, E and υ, in terms of the plane-strain stiffness components

$$E = \frac{C_{12}^{(\varepsilon)}\left(3C_{11}^{(\varepsilon)} - 4C_{12}^{(\varepsilon)}\right)}{C_{11}^{(\varepsilon)} - C_{12}^{(\varepsilon)}}, \quad \upsilon = \frac{C_{11}^{(\varepsilon)} - 2C_{12}^{(\varepsilon)}}{2\left(C_{11}^{(\varepsilon)} - C_{12}^{(\varepsilon)}\right)} \tag{A5}$$

Equations (A5) follow from the stiffness coefficient matrix

$$\left[C_{ab}^{(\varepsilon)}\right] = \begin{bmatrix} C_{11}^{(\varepsilon)} & C_{12}^{(\varepsilon)} & C_{16}^{(\varepsilon)} \\ C_{21}^{(\varepsilon)} & C_{22}^{(\varepsilon)} & C_{26}^{(\varepsilon)} \\ C_{61}^{(\varepsilon)} & C_{62}^{(\varepsilon)} & C_{66}^{(\varepsilon)} \end{bmatrix} = \frac{E}{(1+\upsilon)(1-2\upsilon)} \begin{bmatrix} 1-\upsilon & \upsilon & 0 \\ \upsilon & 1-\upsilon & 0 \\ 0 & 0 & (1-2\upsilon)/2 \end{bmatrix} \tag{A6}$$

corresponding to the apparent plane-strain constitutive equations (Nemat-Nasser and Hori, 1993). Notice the compacted notation in equations (A5) and (A6): $11 \to 1$, $22 \to 2$, and $12 \to 6$.

Also, notice that the isotropy condition $C_{66}^{(\varepsilon)} = \left(C_{11}^{(\varepsilon)} - C_{12}^{(\varepsilon)}\right)/2$ and the symmetry condition $C_{12}^{(\varepsilon)} = C_{66}^{(\varepsilon)}$ imply that

$$C_{12}^{(\varepsilon)} = \frac{C_{11}^{(\varepsilon)}}{3} \tag{A7}$$

Since equation (A7) is satisfied by two-dimensional lattices with the central-force interaction, equations (A5) are reduced to

$$E = \frac{5}{6}\, C_{11}^{(\varepsilon)}, \quad \upsilon = \frac{1}{4} \tag{A8}$$

while from equations (A3a) and (A8) it follows that

$$E^{(\varepsilon)} = \frac{8}{9} C_{11}^{(\varepsilon)}, \quad \upsilon^{(\varepsilon)} = \frac{1}{3} \tag{A9}$$

Finally, keeping in mind the relationship between the plane-strain modulus of elasticity and the link stiffness of the triangular lattice with the nearest-neighbor central-force interaction, $E^{(\varepsilon)} = 2k/\sqrt{3}$, (Monette and Anderson, 1994), it is obvious, based on equations (A3a) and (A8) that

$$E = \frac{5\sqrt{3}}{8} k \tag{A10}$$

Equation (A10) provides a connection between the mechanical property of the material, E, and the link stiffness (or the average link stiffness, $\bar{k}$, in the case of the structurally disordered lattice) of the discrete element system.

APPENDIX B

DYNAMIC EXPANSION OF CYLINDRICAL CAVITY IN ELASTIC CONTINUUM

The plane stress solution of the problem of a circular cavity of radius a in infinite elastic plate subjected to a sudden pressure or constant-velocity radial displacement at the cavity perimeter was originally derived by Kromm (1948). The gist of the method is to reduce the governing differential equation to an integral equation of Volterra's first kind, suitable for a numerical solution.

The boundary and initial value problem is defined by the governing partial differential equation

$$\frac{\partial^2 u}{\partial r^2} + \frac{1}{r}\frac{\partial u}{\partial r} - \frac{u}{r^2} = \frac{1}{C_L}\frac{\partial^2 u}{\partial t^2} \tag{B1a}$$

subject to the initial

$$u \equiv 0, \frac{\partial u}{\partial t} \equiv 0 \quad t = 0, r > a \tag{B1b}$$

and boundary conditions

$$\frac{\partial u}{\partial t} = \dot{a} \quad t \geq 0, r = a \tag{B1c}$$

In equations (B1), u is the particle displacement, r current radius, t time, $\dot{a}$ prescribed (controlled) cavity expansion rate, and C_L velocity of elastic longitudinal waves.

Using the Laplace transformation[†] the wave equation (B1a) can be reduced to an ordinary differential equation

[†] In the following analysis the Laplace transformation and inverse Laplace transformation are denoted by $\mathcal{L}\{\ \}$ and $\mathcal{L}'\{\ \}$, respectively.

$$r^2\frac{d^2U}{dr^2}+r\frac{dU}{dr}-\left[\left(\frac{sr}{C_L}\right)^2+1\right]U=0 \tag{B2a}$$

while the boundary condition (B1c) becomes

$$U(a,s)=\frac{\dot{a}}{s^2} \tag{B2b}$$

In equation (B2) $U(r,s)=\mathcal{L}\{u(r,t)\}$ while s is the Laplace's variable.

The particle displacement in the Laplace space

$$U(r,s)=\frac{\dot{a}}{s^2}\frac{K_1(sr/C_L)}{K_1(sa/C_L)} \tag{B3}$$

where $K_1()$ is the modified Bessel function of the second kind, obtained by solving the boundary value problem (B2). The general solution of the boundary value problem (B2) contains the modified Bessel function of the first kind $I_1()$, which is discarded in order to obtain the bounded solution. Since the "inverse transformation" of the solution (B3) cannot be derived analytically it is necessary to resort to a numerical solution.

Manipulations are simplified introducing variables in the form of

$$\begin{gathered}\bar{r}=\frac{r}{a},\quad \bar{t}=\frac{C_L t}{a},\quad \bar{s}=\frac{sa}{C_L},\quad \bar{u}=\frac{u}{a}\frac{C_L}{\dot{a}},\quad \bar{U}=U\frac{C_L}{\dot{a}}\frac{C_L}{a^2}\\ \frac{\partial\bar{u}}{\partial\bar{r}}=\frac{\partial u}{\partial r}\frac{C_L}{\dot{a}},\quad \frac{\partial\bar{u}}{\partial\bar{t}}=\frac{\partial u}{\partial t}\frac{1}{\dot{a}},\quad \bar{\sigma}_r=\left\{1-\left[\upsilon^{(\varepsilon)}\right]^2\right\}\frac{\sigma_r}{E^{(\varepsilon)}}\frac{C_L}{\dot{a}},\quad \bar{\sigma}_\theta=\left\{1-\left[\upsilon^{(\varepsilon)}\right]^2\right\}\frac{\sigma_\theta}{E^{(\varepsilon)}}\frac{C_L}{\dot{a}}\end{gathered} \tag{B4}$$

In equation (B4) σ_r and σ_θ are the radial and circumferential components of stress tensor, while $\upsilon^{(\varepsilon)}$ and $E^{(\varepsilon)}$ are the elastic material properties in two-dimensional formulation (Appendix A).

The particle displacement (B3) is, in view of (B4), equal to

$$\bar{U}(\bar{r},\bar{s})=\frac{1}{\bar{s}^2}\frac{K_1(\bar{s}\bar{r})}{K_1(\bar{s})} \tag{B5}$$

Furthermore equation (B5) can be written in the form

$$\overline{U}(\bar{r},\bar{s})e^{\bar{s}}K_1(\bar{s})=\frac{1}{\bar{s}^2}e^{\bar{s}}K_1(\bar{s}\bar{r}) \tag{B6}$$

which has the advantage that the inverses of the functions $e^{\bar{s}}K_1(\bar{s})$ and $e^{\bar{s}}K_1(\bar{s}\bar{r})/\bar{s}^2$ are amenable to analytical solution using the Schlafli integral theorem (Watson, 1945).

The Schlafli integral representation of the modified Bessel function of the second kind $K_n(z)$

$$K_n(z)=\frac{\Gamma(1/2)}{\Gamma(n+1/2)}\left(\frac{z}{2}\right)^n\int_1^\infty e^{-zt}\left(t^2-1\right)^{n-1/2}dt \tag{B7}$$

is the basis of the oncoming analysis. In the preceding equation Γ() stands for the Gamma function. As a first step in deriving the appropriate inverse transforms, $K_1(\bar{s})$, written in the integral form of equation (B7), is multiplied by $e^{\bar{s}}$ yielding

$$e^{\bar{s}}K_1(\bar{s})=\bar{s}\int_1^\infty e^{-\bar{s}(t-1)}\sqrt{t^2-1}dt \tag{B8a}$$

A change of the integration variable $\tau=t-1$

$$e^{\bar{s}}K_1(\bar{s})=\bar{s}\int_0^\infty e^{-\bar{s}\tau}\sqrt{(\tau+1)^2-1}d\tau \tag{B8b}$$

followed by the integration by parts of (B8b) leads to the first inverse transformation

$$k(\bar{t})=\mathcal{L}^{-1}\left\{e^{\bar{s}}K_1(\bar{s})\right\}=\frac{\bar{t}+1}{\sqrt{(\bar{t}+1)^2-1}} \tag{B9}$$

on the left side of expression (B6).

Similarly, by multiplying $K_1(\bar{s}\bar{r})$, written in the integral form (B7), by $e^{\bar{s}}/\bar{s}^2$

$$\frac{1}{\bar{s}^2}e^{\bar{s}}K_1(\bar{s}\bar{r})=\frac{\bar{r}}{\bar{s}}\int_1^\infty e^{-\bar{s}(\bar{r}t-1)}\sqrt{t^2-1}dt \tag{B10a}$$

changing the integration variable $\tau=\bar{r}t-1$

$$\frac{1}{\bar{s}^2}e^{\bar{s}}K_1(\bar{s}\bar{r})=\frac{1}{\bar{s}\bar{r}}\int_1^{\infty}e^{-\bar{s}\tau}\sqrt{(\tau+1)^2-\bar{r}^2}\,d\tau \tag{B10b}$$

and integrating by parts, the following expression

$$\frac{1}{\bar{s}^2}e^{\bar{s}}K_1(\bar{s}\bar{r})=\int_{\bar{r}-1}^{\infty}e^{-\bar{s}\tau}\left[\frac{\tau+1}{2\bar{r}}\sqrt{(\tau+1)^2-\bar{r}^2}-\frac{\bar{r}}{2}\ln\left(\frac{\bar{t}+1+\sqrt{(\bar{t}+1)^2-\bar{r}^2}}{\bar{r}}\right)\right]d\tau \tag{B10c}$$

is obtained. The inverse transformation of the right side of (B6)

$$u(\bar{r},\bar{t})=\mathcal{L}^{-1}\left\{\frac{1}{\bar{s}^2}e^{\bar{s}}K_1(\bar{s}\bar{r})\right\}=$$

$$=\left\{\frac{\bar{t}+1}{2\bar{r}}\sqrt{(\bar{t}+1)^2-\bar{r}^2}-\frac{\bar{r}}{2}\ln\left(\frac{\bar{t}+1+\sqrt{(\bar{t}+1)^2-\bar{r}^2}}{\bar{r}}\right)\right\}\mathcal{H}(\bar{r}-1) \tag{B11}$$

can be readily inferred by comparison of (B10c) and the definition of Laplace transform $\mathcal{L}\{f(t)\}=\int_0^{\infty}e^{-st}f(t)dt$. In (B11) $\mathcal{H}(\ )$ refers to the Heaviside (unit step) function.

The left side of equation (B6) is the product of two Laplace transforms for which the inverse transforms (B9) and (B11) are now available. Thus, is convenient to invoke the convolution theorem (Watson, 1945)

Let $f(t)$ and $g(t)$ satisfy the hypothesis of the existence of Laplace transforms. Then the product of their transforms $F(s)=\mathcal{L}\{f(t)\}$ and $G(s)=\mathcal{L}\{g(t)\}$ is the transform $H(s)=\mathcal{L}\{h(t)\}$ of the convolution $h(t)$ of $f(t)$ and $g(t)$, which is denoted by $(f*g)(t)$ and defined by

$$h(t)=(f*g)(t)=\int_0^t f(\tau)\,g(t-\tau)\,d\tau \tag{B12}$$

Therefore, the equation (B6) can be written in the convolution integral form

$$\int_{\bar{r}-1}^{\bar{t}}\bar{u}(\tau)\,k(\bar{t}-\tau)\,d\tau=u(\bar{r},\bar{t}) \tag{B13}$$

Since the functions $\kappa(\bar{t})$ and $\alpha(\bar{r},\bar{t})$ are available the particle displacement $\bar{u}(\bar{r},\bar{t})$ can be obtained solving the integral equation (B14) numerically (Press et al., 1995). In short, the convolution integral can be rewritten in form of the system of algebraic equations

$$\sum_{m=1}^{n} \bar{u}_m k_{nm} = \alpha_n \tag{B14a}$$

where

$$\bar{u}_m = \bar{u}(\bar{r}, \bar{t}_{m-1} + \delta/2), \quad k_{nm} = \int_{\bar{t}_{m-1}}^{\bar{t}_m} \kappa(\bar{t}_n - \tau)\, d\tau, \quad \alpha_n = \alpha(\bar{r}, \bar{t}_n) \tag{B14b}$$

Since the square matrix of the system (B14a) is of the lower triangular form the particle displacement can be evaluated by following scheme

$$\bar{u}_i = \frac{\alpha_i}{k_{ii}} - \sum_{\alpha=1}^{i-1} \frac{\bar{u}_\alpha k_{i\alpha}}{k_{ii}} \tag{B15}$$

The numerical solution of the problem is obtained from (B15) for three radiuses $r = a, 2.5\,a, 4\,a$, and plotted in Fig. B.1.

Next it is necessary to evaluate the radial and circumferential stresses starting from the well known linear elasticity constitutive expressions.

$$\sigma_r = \frac{E^{(\varepsilon)}}{\left\{1 - \left[\upsilon^{(\varepsilon)}\right]^2\right\}} \left(\frac{\partial U}{\partial r} + \upsilon^{(\varepsilon)} \frac{U}{r} \right) \tag{B16a}$$

$$\sigma_\theta = \frac{E^{(\varepsilon)}}{\left\{1 - \left[\upsilon^{(\varepsilon)}\right]^2\right\}} \left(\frac{U}{r} + \upsilon^{(\varepsilon)} \frac{\partial U}{\partial r} \right) \tag{B16b}$$

The convolution integral representations

$$\int_{\bar{r}-1}^{\infty} \bar{\sigma}_i(\bar{r},\tau)\, \kappa(\bar{t} - \tau)\, d\tau = \alpha_i(\bar{r}, \bar{t}), \quad i = r, \theta \tag{B17}$$

are derived following the same procedure described above for the estimate of the

particle velocity. The function $\mathcal{k}(\bar{t})$ is defined by (B9), while the functions on the right side of the expression (B17) are

$$u_r(\bar{r},\bar{t})=\left\{-\frac{1+\upsilon^{(\varepsilon)}}{2}\ln\left(\frac{\bar{t}+1+\sqrt{(\bar{t}+1)^2-\bar{r}^2}}{\bar{r}}\right)-\frac{1-\upsilon^{(\varepsilon)}}{2}\left(\frac{\bar{t}+1}{\bar{r}^2}\right)\sqrt{(\bar{t}+1)^2-\bar{r}^2}\right\}\mathcal{H}(\bar{r}-1) \tag{B18}$$

$$u_\theta(\bar{r},\bar{t})=\left\{-\frac{1+\upsilon^{(\varepsilon)}}{2}\ln\left(\frac{\bar{t}+1+\sqrt{(\bar{t}+1)^2-\bar{r}^2}}{\bar{r}}\right)+\frac{1-\upsilon^{(\varepsilon)}}{2}\left(\frac{\bar{t}+1}{\bar{r}^2}\right)\sqrt{(\bar{t}+1)^2-\bar{r}^2}\right\}\mathcal{H}(\bar{r}-1)$$

The radial and circumferential stresses evaluated by the numerical solution of (B17) are plotted vs. time for three different radiuses in Fig. B.2. The initial jump (discontinuity) of stress components corresponds to the value of the radial and circumferential stress at the elastic wave front (Kromm, 1948)

$$\sigma_r=\frac{E^{(\varepsilon)}}{\left\{1-\left[\upsilon^{(\varepsilon)}\right]^2\right\}}\frac{\dot{a}}{C_L}\sqrt{\frac{a}{r}}=\frac{1}{\upsilon^{(\varepsilon)}}\sigma_\theta \tag{B19}$$

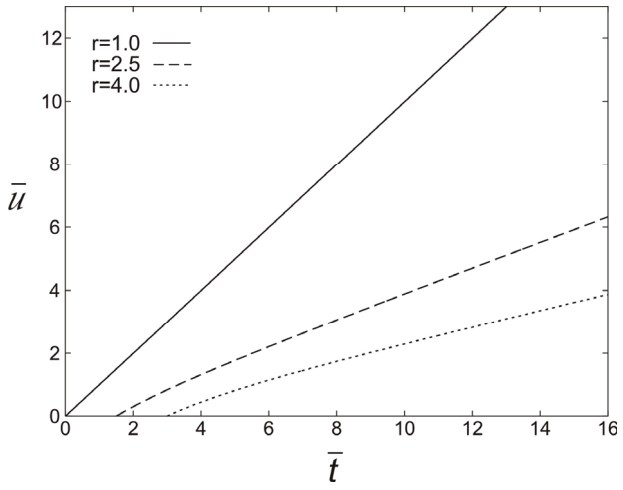

Fig. B.1. Particle displacement vs. time at three different radii.

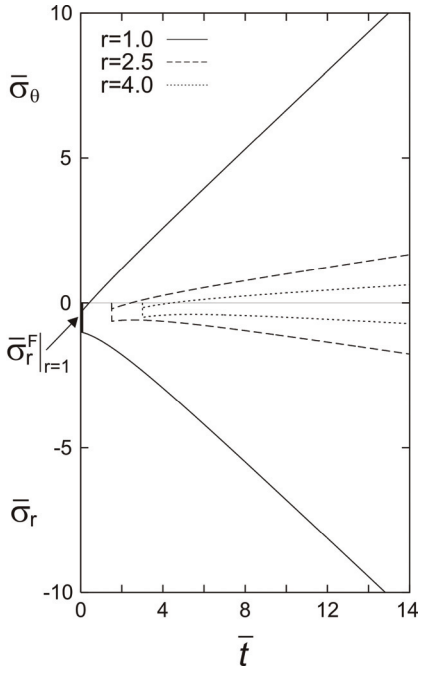

Fig. B.2. Radial and circumferential stress components vs. time at three radii.

In the case of the plane strain, $E^{(\varepsilon)} = E/\left(1-\upsilon^2\right)$, $\upsilon^{(\varepsilon)} = \upsilon/\left(1-\upsilon\right)$ (A3a), the stress components at the elastic wave front at the perimeter of the cylindrical cavity ($r = a$) are

$$\sigma_r^F = \frac{(1-\upsilon)E}{(1-2\upsilon)(1+\upsilon)}\frac{\dot{a}}{C_L} = \frac{1-\upsilon}{\upsilon}\sigma_\theta^F \tag{B20}$$

APPENDIX C

PARRINELLO-RAHMAN MOLECULAR DYNAMICS

The computational restrictions on the ensemble size unavoidably overemphasize the importance of external surfaces on the deformation pattern. To eliminate the undesirable surface effects a considered ensemble of particles is approximated by a periodic arrangement of equal cells. However, the fixed geometry of periodic cell (surrounded from all sides by identical neighbors, similar to a cell model used in micromechanics (Nemat-Nasser and Hori, 1993)) proved to be too restrictive in many applications, as discussed previously. This restriction motivated Parrinello and Rahman (1981, 1982) to modify the original concept by introducing macroscopic dynamic variable that control the change of the cell shape and size.

The equations of motion of the individual particles within the periodic cell (defined by the scaled position vectors $s_i = h^{-1} r_i$)[‡] is

$$\ddot{s}_i = -\sum_{j \neq i} \frac{1}{m_i} \frac{1}{r_{ij}} \frac{\partial \phi}{\partial r_{ij}} \left(s_i - s_j \right) - M^{-1} \dot{M} \, \dot{s}_i \qquad \left(i = 1,...,N \right) \tag{C1}$$

The equation of motion for the box itself (defined by the matrix $h = \left\{ \vec{a}, \vec{b}, \vec{c} \right\}$ whose components are vectors spanning the edges of the periodic cell) is

$$W \ddot{h} = \left(\pi - p_e \right) \sigma - h \Sigma \tag{C2}$$

Both equations of motion can be derived from the Lagrangian (2.15) introduced by Parinnello and Rahman. In equations (C1) and (C2) the parameter $\sigma = \Omega_b \left(h^T \right)^{-1}$ carries the information that define the size (Ω_b is the volume of the box) and the shape (h) of the periodic box; all other variables and parameters are already introduced. The right hand side of (C2) relates the change of the shape of periodic box to the dynamic imbalance between the externally applied, and the internally generated, stress tensor. The fictitious mass W in (C2) determines the response time needed by the system to recover from the stress imbalance. Andersen suggested that the fictitious mass is to the first order equal to L/C_L, where L is the box size and C_L longitudinal velocity of

[‡] The superscripts "-1" and "T" designate the inverse and transpose matrix, respectively.

elastic waves (Andersen, 1980). The true meaning and the choices for the fictitious mass are discussed at length in several papers (Anderson, 1980; Parrinello and Rahman, 1981; Nose and Klein, 1983; Li and Johnson, 1992).

The internally generated pressure matrix π represents the response of the system subjected to the externally applied pressure p_e (more precisely, the spherical part of the externally applied stress tensor S).

$$\pi = \frac{1}{\Omega_b}\left[\sum_i m_i \dot{r}_i \dot{r}_i^T - \sum_i \sum_{j>i} \frac{1}{r_{ij}}\left(\frac{\partial \phi}{\partial r_{ij}}\right) r_{ij} r_{ij}^T\right] \tag{C3}$$

Following the standard elasticity definition, the strain tensor can be identified as $\varepsilon = (1/2)\left[\left(h_0^T\right)^{-1} M h_0^{-1} - 1\right]$, where h_0 is the matrix defining the reference state. The symmetric tensor $\sum$ is related to the external Cauchy stress S

$$\Sigma = h_0^{-1}\left(S - p_e I\right)\left(h_0^T\right)^{-1}\Omega_{b0} \tag{C4}$$

where I is the identity matrix, and subscript "0" refers to the reference (undeformed) state

.

In the case of a displacement controlled test, i.e. when $S = 0 \Rightarrow p_e = 0, \Sigma = 0$, the differential equation (C3) reduces to

$$W \ddot{h} = \pi \sigma \tag{C5}$$

Li and Johnson noticed that the Parinnello-Rahman molecular dynamics, in contrast to the conventional molecular dynamics, does not conserve the angular momentum (Li and Johnson, 1992). More specifically, since the Lagrangian (2.15) is not derived from first principles the conservation of angular momentum is by no means guaranteed.[§] The angular momentum that is not conserved may cause the net

[§] Strictly speaking, the fact that the angular momentum is not conserved is characteristic for the imposition of periodic boundary conditions in general. It is usually argued that the unwanted effects should disappear due to averaging over a long time, since the number of atoms exchanged with the image boxes will be nearly equal in all directions forcing the components of angular momentum to fluctuate about constant values. While this may be true in the case of totally random phenomena the same is by no means obvious in the case of strongly "spatially biased" events. Therefore, tacitly assumed conservation of angular momentum in molecular dynamics simulations on cells with periodic boundary conditions should be subject to a serious inquire, especially in the context of the Parinnello-Rahman

rotation of the periodic box and lead to a build-up of shear stress that are not physical in nature. This was, in fact, observed in the simulations performed in this study. In order to overcome this difficulty Li and Johnson suggested a modified version of Parinnello-Rahman Lagrangian

$$\Lambda_L = \frac{1}{2}\sum_{i=1}^{N} m_i \, \dot{s}_i^T M \, \dot{s}_i - \sum_{i=1}^{N}\sum_{j>1}^{N} \phi\left(r_{ij}\right) + \frac{1}{2} W \, Tr\left(\dot{h} \, Q \, \dot{h}^T\right) - p_e \, \Omega_b \qquad \text{(C6)}$$

that generates differential equations which take into account symmetry and rotation invariance. In (C6) $Q = \Omega_b^2 h^{-1}\left(h^T\right)^{-1}$ is an additional matric tensor and *Tr*() denotes the trace of a matrix.

The equation of motion of the periodic box, for the case when only hydrostatic pressure is applied

$$W\ddot{h} = \left(1/\Omega_b\right)\left(p_i - p_e 1\right)h - \left(W/\Omega_b^2\right)\left[-2\Omega_b\dot{\Omega}_b\dot{h} + Tr\left(\dot{h}Q\dot{h}^T\right)h + \dot{h}Q\dot{M} - \Omega_b\sigma\dot{h}^T\dot{h}\right] \qquad \text{(C7)}$$

can be derived from the Lee and Johnson Lagrangian (C6), while the equation of motion of the particles in the box, defined by the scaled positions s_i (C1), remain unchanged. With a proper choice of *W*, the rotations and distortions of the box completely disappear when the ensemble is subjected to the hydrostatic external load.

---

modification.

APPENDIX D

SHORT-TIME RESPONSE OF TWO-DIMENSIONAL LATTICES DURING DYNAMIC LOADING

The scope of Appendix D analysis is limited to an investigation of a detail of the dynamic response of the two-dimensional triangular and square lattices: a transition from short-time (*st*) to long-time (*lt*) elastic properties, which is not accompanied by the corresponding change of stiffness tensor components. The study is performed on three two-dimensional truss-type lattices under two different simulation setups: the homogeneous (Mastilovic, 2008), and natural (inhomogeneous) (Mastilovic, accepted). It is demonstrated that the difference between the two sets of elastic properties is a result of combining effects of the lateral inertia and the disorder of the discrete system. Although the following discussion refers to the triangular lattice with the first-neighbor central interactions, two other two-dimensional lattices investigated by Mastilovic (2008, accepted), the triangular lattice with the second-neighbor central interactions and the square lattice with the second-neighbor central interaction, behave similarly.

The present discussion is also limited only to the natural (inhomogeneous) simulation setup, presented in Mastilovic (accepted), since the homogeneous simulation setup is discussed in detail in Section 3.3. The corresponding analysis of the homogeneous simulation setup is available in (Mastilovic, 2008). The natural tension simulation mimics the corresponding laboratory experiment. The displacement-control mechanical load, $\dot{y} = \pm \dot{\varepsilon}\, L/2$, applied on the specimen boundaries ($y = \pm L/2$) (see Fig. 3.18), is transferred by stress waves through the specimen, which results in the characteristic "staircase" time history of the local stress (Fig. 3.20a).

Fig. D1 presents the time histories of the stress in the loading direction divided by the corresponding strain rate, and the Poisson's ratio. It is evident from Fig. D1a that the two characteristic slopes are the natural-setup counterparts of short-time and long-time moduli ($E_{st}^{(\varepsilon)}$, $E_{lt}^{(\varepsilon)}$, respectively[**]) from Fig. 3.23, presented herein in a more convenient graph. The solid curve in Fig. D1a is common for all loading rates that

[**] The apparent plane-strain modulus of elasticity $E^{(1)}$ and the apparent plane-strain Poisson's ratio $\nu^{(1)}$ will be, for brevity, referred to as the modulus of elasticity and the Poisson's ratio in the remainder of this Appendix.

remain elastic for the given graph limits; departures from that curve mark onsets of the inelastic deformation that is characterized by damage nucleation and, depending on the loading rate, different levels of cooperative phenomena (Mastilovic et al., 2008). Thus, the only difference between the moderate and the high loading rates is that in the later case specimens fail before the $E_{st}^{(\varepsilon)} \to E_{lt}^{(\varepsilon)}$ elastic transition occurs, which explains the unchanged stiffness tensor components, in spite of the apparent change of the modulus of elasticity (and the Poisson's ratio).

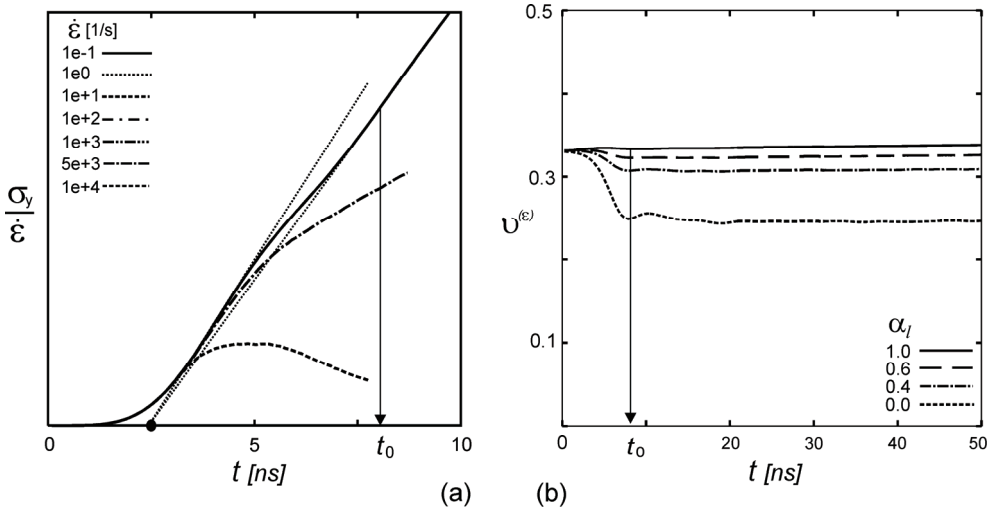

Fig.D1. Time history of: (a) the stress normalized by the corresponding strain rate, and (b) the Poisson's ratio for the tension test of the structurally and geometrically disordered sample.

The influence that inertia exerts on the modulus of elasticity is reflected by $\left(E_{st}/E_{lt}\right)^{(\varepsilon)} > 1$ even for the ideal lattice. The stiffness components, the elastic moduli, and the Poisson's ratio are weakly (≈ 5%) affected by moderate geometrical disorder ($0.4 \le \alpha_l \le 1$). On the other hand, the stiffness components and the Poisson's ratio are insensitive to the structural disorder (i.e., β_l-independent), while the effect on the moduli of elasticity is similar to that of the geometrical disorder.

The simulation results further indicate that for the ideal triangular lattice with the first-neighbor central interactions

$$E^{(\varepsilon)} = \begin{cases} E_{st}^{(\varepsilon)} = C_{11}^{(\varepsilon)} & t < t_0 \\ E_{lt}^{(\varepsilon)} = 8C_{11}^{(\varepsilon)}/9 & t \ge t_0 \end{cases} \tag{D1}$$

while for the moderately disordered lattice the expressions hold only approximately (hence "=" should be replaced by "≈" under the curly brace) with the degree of approximation driven by the level of disorder. The expression for $E_{lt}^{(\varepsilon)} = 8\,C_{11}^{(\varepsilon)}/9$ is derived in Appendix A as equation (A9).

The $E_{st}^{(\varepsilon)} \to E_{lt}^{(\varepsilon)}$ transition time is

$$t_o \approx 2\pi \frac{l_c}{C_L} = T_0 \tag{D2}$$

where T_0 is the period of harmonic undamped oscillations corresponding to the natural frequency $\omega_0 = C_0/l_c$ of the discrete system, $l_c = \overline{\lambda}$ the model resolution length, and C_L the velocity of the elastic longitudinal wave propagation. The transition time is independent of the aspect ratio and size of the specimen used in simulations.

As evident from Fig. D1b, the Poisson's ratio experiences the similar elastic transition: it changes from the analytical value 1/3, characteristic of the ideal triangular lattice with the first-neighbor central interactions (A9). Again, the dependence is relatively moderate for moderately geometrically disordered lattice: the difference in $\upsilon^{(\varepsilon)}$ is ≈ 5% for the change in α_l from 1 to 0.4. The more substantial $\upsilon^{(\varepsilon)}$ reduction is observed for the strongly geometrically disordered lattice (α_l = 0.02); the lower bound of $\upsilon_{lt}^{(\varepsilon)}$ settles at 1/4. On the other hand, $\upsilon^{(\varepsilon)}$ is independent of structural disorder, defined by parameter β_l.

At first look, the $E_{st}^{(\varepsilon)} \to E_{lt}^{(\varepsilon)}$ elastic transition might appear reminiscent of the difference between the adiabatic and the isothermal moduli of elasticity (Edelglass, 1966), but one should recall that the $E_{st}^{(\varepsilon)} \to E_{lt}^{(\varepsilon)}$ elastic transition occurs at all loading rates investigated herein, reaffirming that all physical events are dynamic on some scale. Similarly, it is well known that the dynamic modulus of elasticity measured by, for instance, the Ultrasonic Pulse Method, somewhat exceeds the quasi-static counterpart. The Ultrasonic Pulse Method is based on the relationship $E = \rho C_L^2$ between the modulus of elasticity and velocity of longitudinal wave propagation. For the ideal triangular lattice with the first-neighbor central interactions $(\alpha_l = 1, \beta_l = 1)$, this relation yields the analytical result $E^{(\varepsilon)} = 57.7$ (Monette and Anderson, 1994), which agrees remarkably well with $E_{lt}^{(\varepsilon)}$ obtained in the simulations (Mastilovic, accepted).

In summary, the outlined investigation identifies two sources of disagreement between the elastic properties:

- the inertia of the system, which in the case of natural simulation setup and the moderately disordered lattice governs the observed elastic transition $E_{st}^{(\varepsilon)} \approx C_{11}^{(\varepsilon)} \rightarrow E_{lt}^{(\varepsilon)}$.
- the geometrical and structural disorder, which influences the $E_{st}^{(\varepsilon)} \rightarrow E_{lt}^{(\varepsilon)}$ elastic transition (including the ratio $E_{st}^{(\varepsilon)} / E_{lt}^{(\varepsilon)}$) independently of the inertial effects.

As discussed in Section 3.3, the homogeneous lattice simulation setup is based on the imposed initial velocity field defined by equations (3.3) that, regardless of the loading power, practically cancels out the stress component perpendicular to the loading direction (Fig. 3.19). In other words, the imposed initial velocity field (3.3) cancels out the inertial effect and consequently the difference in moduli under the first bullet; but the latter re-emerges with well-defined transition time (Mastilovic, 2008) with introduction of the lattice disorder (the second bullet).

Finally, it is shown that only the ideal lattice behavior is equivalent to the behavior of a solid under the plane-strain conditions. “As soon as the disorder is introduced, the behavior of a solid could only be approximated by the behavior of the two-dimensional systems, with the degree of accuracy that decreases with the level of disorder “quenched” within the lattice.” (Mastilovic, accepted).

REFERENCES

Achenbach, J. D. (1973). *Wave Propagation in Elastic Solids*. North-Holland, Amsterdam.

Alekseevskii, V. P. (1966). Penetration of a rod into target at high velocity. *Combus. Explos. Shock Waves* **2**: 63-66.

Allen, M. P. and Tildesley, D. J. (1987). *Computer Simulation of Liquids*. Oxford University Press Inc., New York.

Ames, W. F. (1965). *Nonlinear Partial Differential Equations in Engineering*. Academic Press, New York.

Andersen, H. C. (1980). Molecular dynamics simulations at constant pressure and/or temperature. *J. Chem. Phys.* **72**: 2384-2392.

Anderson, T.L. (1991). Fracture Mechanics, CRC Press, Boston

Anderson, C. E. Jr, and Walker, J. D. (1991). An examination of long-rod penetration. *Int. J. Impact Engng.* **11**: 481-501.

Anderson, C. E. Jr, Walker, J. D. and Hauver, G. E. (1992*). Target resistance for long-rod penetration into semi-infinite targets*. North-Holland, Amsterdam.

Anderson, C. E. Jr and Morris, B. L. (1992). The ballistic performance of confined $Al_2 0_3$ ceramic tiles. *Int. J. Impact Engng*. **12**: 167-187.

Anderson, C. E. Jr, Walker, J. D., Bless, S. J. and Partom, Y. (1996). On the L/D effect for long-rod penetrators. *Int. J. Impact. Engng*. **18**: 247-264.

Ashby, M. F. and Sammis, C. G. (1990). The damage mechanics of brittle solids in compression. *PAGEOPH* **133**: 489-521.

Bao, Y., Jin Z. (1994). Evolution of impact resistance and brittleness of structural ceramics. *Nuclear Engineering and Design* **150**: 323-328.

Batra, R. C. and Wright, T. W. (1986). Steady state penetration of rigid perfectly plastic targets. *Int. J. Impact Engng*. **24**: 41-54.

Bazant Z.P. 2008. Mechanics based statistical prediction of structure size and geometry effects on safety factors for composites and other quasibrittle materials. *Theoretical and Applied Mechanics*. (accepted)

Beale, P. D. and Srolowitz, D. J. (1988). Elastic fracture in random materials. *Phys. Rev. B* **37**: 5500-5507.

Belytschko, T., Lu, Y. Y. and Gu, L. (1994). Element-free Galerkin methods. *Int. J. Num. Methods Engng.* **37**: 229-256.

Benson, D. J. (1992). Computational methods in Lagrangian and Eulerian hydrocodes. *Comput. Methods Appl. Mech. Engng.* **99**: 235-394.

Benson, D. J. (1997). A mixture theory for contact in multi-material Eulerian formulations. *Comput. Methods Appl. Mech. Engng*. **140**: 59-86.

Billington, E. W. and Tate, A. (1981). *The Physics of Deformation and Flow*. McGraw-Hill, New York.

Bishop, R. F., Hill, R. and Mott, N. F. (1945). The theory of indentation and hardness tests. *Proc. Phys. Soc. Lond.* **57**: 147-159.

Blanton, T. L. (1981). Effect of strain rate from 10^{-2} to 10 $\sec^{-1}$ in triaxial compression tests on three rocks. *Int. J. Rock Mech. Min. Sci. & Geomech. Abstr*. **18**: 47-62.

Bless, S. J., Rosenberg, Z., and Yoon, B. (1987). Hypervelocity penetration of ceramics, *Int. J. Impact Engng*. **5**: 165-171.

Born M., von Karman T. (1912). Über schwingungen in raumgittern. *Physik. Z*. **13**: 297-309.

Born, M. and Huang, K. (1956). *Dynamical Theory of Crystal Lattices*. Clarendon Press, Oxford.

Brar, N. S. and Bless, S. J. (1991). Impact-induced failure waves in glass bars and plates, *Appl. Phys. Lett*. **59**: 3396-3398.

Brara, A., Camborde, F., Klepaczko, J.R., Mariotti, C., (2001). Experimental and numerical study of concrete at high strain rates in tension. Mech. Mater., **33**: 33-45.

Buehler, M.J., Gao, H., and Huang, Y. (2004). Atomistic and continuum studies of stress and strain fields near a rapidly propagating crack in a harmonic lattice, *Theoretical and Applied Fracture Mechanics* **41**: 21-42.

Cagnoux, J. and Longy, F. (1987). Is the dynamic strength of alumina rate dependent? In: *Shock Waves in Condensed Matter 1987* (Edited by S. C. Schnidt and N. C. Holmes), pp. 293-296, Elsevier, Amsterdam.

Callen, H. B. (1961). *Thermodynamics*. John Willey, New York.

Camacho, G. T. and Ortiz, M. (1996). Computational modelling of impact damage in brittle materials. *Int. J. Solids Structures* **33**: 2899-2907.

Chandler, D. (1987). *Introduction to Modern Statistical Mechanics*. Oxford University Press, New York.

Chang, Z. and Redner, S. (1990). Kinetics of fragmentation. *J. Phys. A: Math. Gen*. **23**: 1233-1258.

Cox, B.N., Gao, H., Gross, D., and Rittel, D. (2005). Modern topics and chalenges in dynamic fracture. *J. Mech. Phys. Solids* **53**: 565-596.

Cundal, P. A. and Strack, O. D. (1979). A discrete numerical model for granular assemblies. *Geotechnique* **29**: 47-65.

Curtin, W. A. and Scher, H. (1990). Brittle fracture in disordered materials: a spring network model. *J. Mater. Res*. **5**: 535-553.

Dandekar, D. P. (1992). Effect of shock-re-shock on spallation of titanium diboride. In: *Shock Compression of Condensed Matter - 1991* (Edited by S. C. Schmidt *et al*), pp. 487-490. Elsevier, Amsterdam.

Dandekar, D. P. (1994). Response of ceramics under shock-wave loading. In: *High Pressure Science and Technology - 1993*, (Edited by S. C. Schmidt *et al*), pp. 729-732. American Institute of Physics, New York.

Dandekar, D. P. (1994). Shear strengths of aluminum nitride and titanium diboride under plane shock wave compression. *Journal de Physique* **4**: 379-387.

Davidson, L. and Graham, R. A. (1979), Shock compression of solids, *Phys. Rep.* **55**, 255-379.

Desai, C. S. and Siriwardane, H. J. (1984). *Constitutive Laws for Engineering Materials with Emphasis on Geological Materials*. Prentice-Hall Inc., Englewood Cliffs, NJ.

Dienes, J. K. (1978). A statistical theory of fragmentation. In: *Proceedings of the 19th U. S. Symposium on Rock Mechanics* . Conferences and Institutes, Extended Programs and Continuing Education, New York.

Duvall, G. E. and Graham, R. A. (1977). Phase transitions under shock-wave loading. *Rev. Modern Phys.* **49**: 523-579.

Edelglass S.M. (1966) Engineering Materials Science. The Ronald Press Company, New York.

Ercolessi, F. (1997). A molecular dynamics primer. Spring College in Computational Physics, ICTP, Trieste, Italy.

Espinosa, H. D. and Brar, N. S. (1995). Dynamic failure mechanisms of ceramic bars: experiments and numerical simulations. *J. Mech. Phys. Solids* **43**: 1615-1633.

Espinosa, H.D., Zavattieri, P.D. (2003a). A grain level model for the study of failure initiation and evolution in polycrystalline brittle materials. Part I: Theory and numerical implementation. Mech. Mater., **35**: 333-364.

Espinosa, H.D., Zavattieri, P.D. (2003b). A grain level model for the study of failure initiation and evolution in polycrystalline brittle materials. Part II: Numerical examples. Mech. Mater., **35**: 365-395.

Evans, A. G., Gulden, M. E. and Rosenblatt, M. (1977). Impact damage in brittle materials in the elastic-plastic response regime. *Proc. R. Soc. Lond*. **361**: 343-365.

Evans, A. G. (1984). *Fracture in Ceramic Materials*. Noyes Publ., Park Ridge, NJ.

Finkel V.M. (1970). Physics of Fracture. Metalurgia Publ., Moscow.

Florence, A. L., Gefken, P. R., Seaman, L., Curran, D. R. and Shockey, D. A. (1992). Computational models for armor penetration, Technical Report. SRI International, Menlo Park.

Follansbee, P. S. (1985). The Hopkinson bar. In*: Mechanical Testing*, *Metals Handbook* **8**, 198-200. Am. Soc. Metals, Metals Park.

Forrestal, M. J. and Longcope, D. B. (1990). Target strength of ceramic materials for high-velocity penetration. *J. Appl. Phys.* **67**: 3669-3672.

Forrestal, M. J. and Tzou, D. Y. (1997). A spherical cavity-expansion penetration model for concrete targets. To appear in: *Int. J. Solids Structures*.UPDATE

Forrestal, M. J. and Longcope, D. B. (1990). Target strength of ceramic materials for high-velocity penetration. *J. Appl. Phys.* **67**: 3669-3672.

Forrestal, M. J. and Luk, V. K. (1988). Dynamic spherical cavity-expansion in a compressible elastic-plastic solid. *J. Appl. Mech.* **55**: 275-279.

Forrestal, M. J. and Luk, V. K. (1992). Penetration into soil targets. *Int. J. Impact Engng.* **12**: 427-444.

Forrestal, M. J., Frew, D. J., Hanchak, S. J. and Brar, N. S. (1996). Penetration of grout and concrete targets with ogive-nose steel projectiles. *Int. J. Impact Engng.* **18**: 465-476.

Forrestal, M. J. (1986). Penetration into dry porous rock. *Int. J. Solids Structures* **22**: 1485-1500.

Freund, L. B. (1990). *Dynamic Fracture Mechanics*. Cambridge University Press, Cambridge.

Frew, D. J., Forrestal, M. J., Hanchak, S. J. and Green, M. L. (1997). Penetration into limestone targets with ogive-nose steel projectiles. *Proceedings of 14th Army Symposium on Solid Mechanics, Myrtle Beach*, Battelle Press.

Fritts, M. J., Crowley, W. P. and Trease, H. (1983). The free-Lagrangian method. In: *Lecture Notes in Physics 238*, Springer Verlag, Berlin.

Gilman, J.J., (1969). Micromechanics of Flow in Solids. McGrow-Hill, New York.

Glenn, L. A. and Chudnovsky, A. (1986). Strain-rate effects on dynamic fragmentation.
J. Appl. Phys. **59**: 1379-1380.

Grady, D. E. (1980). Shock deformation of brittle solids. *J. Geophys. Res.* **85**: 913-924.

Grady, D. E. (1982). Local inertial effects in dynamic fragmentation. *J. Appl. Phys.* **53**: 322-325.

Grady, D. E. (1995a). *Dynamic Properties of Ceramic Materials*. Sandia Report, SAND 94-3266, Sandia National Laboratories, Albuquerque.

Grady, D. E. (1995b). *Shock Wave Properties of Brittle Solids*. Technical Memorandum TMDG0695, Sandia National Laboratories, Albuquerque.

Grady, D. E. (1996). Shock compression profiles in ceramics. *Sandia Repport SAND96-0551*. Sandia National Laboratories, Albuquerque.

Grady, D.E., (1998). Shock-wave compression of brittle solids. Mech. Mater., **29**: 181-203.

Graham, R. A. (1993). *Solids Under High-Pressure Shock Compression*. Springer-Verlag, Berlin.

Hansen, A. (1964). *Similarity Analysis of Boundary Value Problems in Engineering*. Prentice-Hall, Englewood Clifs.

Hansen, A. Roux, S. and Herrmann, H. J. (1989). Rupture of central-force lattices. *J. Phys. France* **50**: 733-744.

Haule, J. M. (1992). *Molecular Dynamics Simulation*. John Willey , New York.

Hauver, G. E., Netherwood, P. H., Benck, R. F. and Melani, A. (1992). Penetration of shaped-charge jets into glass and crystalline quartz. Technical Report BRL -TR-3273. Ballistic Research Laboratory, Aberdeen Proving Ground, MD.

Hauver, G. (1992). Phenomenological observations of penetration into brittle materials. In: *Material Modeling for Terminal Ballistic Simulation*. (Eddited by J. Walter), pp. 2-6. Technical Report BRL-TR-3392, Ballistic Research Laboratory, Aberdeen Proving Ground, MD.

Heard, H. C. and Cline C. F. (1980). Mechanical behavior of polycrystalline BeO, Al_2O_3 and AlN at high pressure. *J. Mater. Sci.* **15**: 1889-1897.

Hegemier, G. A. and Read, H. E. (1985). On deformation and failure of brittle solids: some outstanding issues. *Mech. Mater.* **4**: 215-259.

Heuze, F. E. (1990). An overview on projectile penetration into geological materials, with emphasis on rocks. *Int. J. Rock Mech. Min. Sci. & Geomech. Abstr*. **27**: 1-14.

Hill, R. (1950). *The Mathematical Theory of Plasticity*. Clarendon Press, Oxford.

Holian, B. L. and Grady, D. E. (1988). Fragmentation by molecular dynamics: the micro-scopic “big bang”. *Phys. Rev. Lett*. **60**: 1355-1358.

Holian, B. L., De Groot, A. J., Hoover W. G., anf Hoover C. G. (1990). Time-reversible equilibrium and nonequilibrium isothermal-isobaric simulations with centered-difference Stoermer algorithms. *Phys. Rev. A* **41**: 4552-4553.

Holian, B. L., Voter, A. F., and Ravelo, R. (1995). Thermostatted molecular dynamics: how to avoid the Tada demon hidden in Nose-Hoover dynamics. *Phys.Rev. E* **52**: 2338-2347.

Holian, B. L., Voter, A. F., Wagner, N. J., Ravelo, R. J., Chen, S. P., Hoover, W. G., Hoover, C. G., and Dontje, T. D. (1991). Effects on pairwise versus many-body forces on high-stress plastic deformation. *Phys. Rev. A* **43**: 2655-2661.

Holian, B. L. (1987). Hypervelocity-impact phenomena via molecular dynamics. *Phys. Rev. A* **36**: 3943-3946.

Hoover, W. G. (1985). Canonical dynamics: Equilibrium phase space distributions. *Phys. Rev. A* **31**: 1695-1697.

Hoover, W. G. (1991). *Computational Statistical Mechanics*. North-Holland, Amsterdam.

Hoover, W. G., Holian, B. L., and Posch, H. A. (1993). Comment on "Possible experiment to check the reality of a nonequilibrium temperature". *Phys.Rew. E* **48**: 3196-3198.

Hoover, W. G. (1986). *Molecular Dynamics*. Springer-Verlag, Berlin.

Hopkins, H. G. (1960). Dynamic expansion of spherical cavities in metals. In: *Progress in Solid Mechanics* (Editors I. N. Sneddon and R. Hill), Vol. 1, 83-163. North-Holland, Amsterdam.

Huang, C. and Subhash G. (2003). Influence of lateral confinement on dynamic damage evolution during uniaxial compressive response of brittle solids. *J. Mech. Phys. Solids* **51**: 1089-1105.

Jeager, J. C. and Cook, N. G. W. (1979). *Fundamentals of Rock Mechanics*. Chapman and Hall, London.

Jirasek, M. and Bazant, Z. P. (1995). Macroscopic fracture characteristics of random particle systems. *Int. J. Fract.* **69**: 201-228.

Johnson, G. R. and Cook, W. H. (1985). Fracture characteristics of three metals subjected to various strains, strain rates, temperatures and pressures. *Engng. Fract. Mech*. **21**, 31-48.

Jonas, G. H. and Zukas, J. A (1978). Mechanics of penetration: analysis and experiment. *Int. J. Engng. Sci.* **16**: 879-903.

Jou, D. and Casas-Vazquez, J. (1992). Possible experiment to check the reality of a nonequilibrium temperature. *Phys. Rev. A* **45**: 8371-8373.

Kachanov, M. (1993). Elastic solids with many cracks and related problems. In*: Advances in Applied Mechanics* (Edited by J. Hutchinson and T. Wu), Vol. 29, pp. 259-445. Academic Press, New York.

Kanel, G. I., Rasorenov, S. V. and Fortov, V. E. (1992). The failure waves and spallations in homogeneous brittle materials. In*: Shock Compression of Condensed Matter -1991* (Edited by S. C. Scmidt), pp. 451-454. North-Holland, Amsterdam.

Kendall, J. (1978). The impossibility of comminuting small particles by compression. *Nature* **272**: 710-711.

Kestin, J. (1992). Local-equilibrium formalism applied to mechanics of solids. *Int. J. Solids Structures* **29**: 1827-1836.

Kipp, M. E., Grady, D. E., and Chen, E. P. (1980). Strain-rate dependent fracture initiation. *Int. J. Fract.* **16**: 471-478.

Klopp, R.W., Clifton, R.J., Shawki, T.G., (1985). Pressure-Shear Impact and the Dynamic Viscoplastic Response of Metals. *Mech. Mater.*, **4**: 375-385.

Kohlhoff, S., Gumbsch, P. and Fischmeister, H. F. (1991). Crack propagation in b.c.c. crystals studied with a combined finite-element and atomistic model. *Phil. Mag. A* **64**: 851-878.

Kolsky, H. (1952). *Stress Waves in Solids*. Dover, New York.

Krajcinovic, D. and Basista, M. (1991). Rupture of central-force lattices revisited. *J. Physics I* **1**: 241-245.

Krajcinovic, D. and Mastilovic, S. (1995). Some fundamental issues of damage mechanics. *Mech. Mater.* **21**: 217-230.

Krajcinovic, D. (1996). *Damage Mechanics*. North-Holland, Amsterdam.

Krajcinovic, D. (1997). Essential structure of damage mechanics theories. In: Tatsumi, T., Watanabe, E., Kambe, T. (Eds.), Theoretical and Applied Mechanics 1996, Proc. 19th IUTAM. North-Holland, Amsterdam, pp. 411-426

Krajcinovic D., Mastilovic S. and Vujosevic M. (1998). Brittle to Quasi-Brittle Transition, *Meccanica* **231**: 1-17.

Krajcinovic D, Vujosevic M. (1998). Strain localization – short to long correlation length transition. *Int. J. Solids Structures* **35**: 4132-4147.

Krajcinovic D. and Mastilovic S. (1999). Statistical Models of Brittle Deformation, Part One: Introduction. *International Journal of Plasticity* **15**: 401-426.

Krajcinovic D. and Mastilovic S. (2000). Thermodynamics and Micromechanics of Damage; in *Continuous Damage and Fracture,* Benallal, A. (Ed.). Elsevier (ISBN: 2-84299-247-4), 19-27.

Krajcinovic D. and Mastilovic S. (2001a). Brittle and quasi-ductile damage at large strain rates. *Theoretical and Applied Fracture Mechanics* **35**: 9-18.

Krajcinovic D. and Mastilovic S. (2001b). Model of quasi-ductile deformations that bridges the scales. *Theoretical and Applied Fracture Mechanics* **37**: 167-182.

Krajcinovic, D, and Rinaldi, A. (2005). Therodynamics and statistical physics of damage processes in quasi-ductile solids. *Mechanics of Materials* **37**: 299-316.

Kromm, A. (1948). Zur Ausbreitung von Stosswellen in Kreislochscheiben. *ZAAM* **28**, 104-114.

Lankford, J. (1981). Mechanicsm responsible for strain-rate-dependent compressive strength in ceramic materials. *J. Am. Ceram. Soc*. **64**: C33-C34.

Lankford, J. (1981). Temperature-strain rate dependance of compressive strength and damage mechanisms in aluminium oxide. *J. Mater. Sci*. **16**: 1567-1578.

Lankford, J., Anderson, C. E. Jr, Royal, S. A. and Riegel, III, J. P. (1996). Penetration erosion phenomenology. *Int. J. Impact Engng*. **18***:* 565-578.

Lemaitre J (1996). A Course on Damage Mechanics. Springer, Berlin.

Lennard-Jones J.E., Devonshire A.F. (1939). Critical and cooperative phenomena. III: A theory of melting and the structure of liquids. *Proceedings of Royal Society of London A* **169**: 317-338.

Li, M. and Johnson, W. L. (1992). Fluctuations and thermodynamic response functions in a Lennard-Jones solid, *Phys. Rev. B* **46**: 5237-5241.

Li, M. and Johnson, W. L. (1993). Ergodicity and convergence of fluctuations in Parrinello-Rahman molecular dynamics. *Mat. Res. Soc. Symp. Proc.* **291**: 285-290.

Lok T.S., Li X.B., Liu D., Zhao P.J. (2002). Testing and Response of Large Diameter Brittle Materials Subjected to High Strain Rate. *Journal of Materials in Civil Engineering*: 262-269.

Louro, L. H. L. and Meyers, M. A. (1989). Effect of stress state and microstructural parameters on impact damage of alumina-based ceramics*, J. Mater. Sci.* **24**: 2516-2531.

Love, A.E.H. (1927). *A Treatise on the Mathematical Theory of Elasticity*. Cambridge University Press, Cambridge.

Lubarda V.A., Krajcinovic D. (1995). Some fundamental issues in rate theory of damage-elasto-plasticity, *Int. J. Plasticity* **11**: 763-797.

Lubarda V.A., Mastilovic S. and Knap J. (1996). Brittle-Ductile Transition in Porous Rocks by Cap Model, *Journal of Engineering Mechanics* **122** (7): 633-642.

Luk, V. K. and Piekutowski, A. J. (1991). An analytical model on penetration of eroding long rods into metallic targets. *Int. J. Impact Engng*. **11**: 323-340.

Mashimo, T. (1987). Shock yielding properties of brittle materials. In: *Shock Waves in Condensed Matter 1987* (Edited by S. C. Schnidt and N. C. Holmes), pp. 289-292, Elsevier, Amsterdam.

Mastilovic, S., Vujosevic, M. and Krajcinovic. D. (1996). Localization in disordered brittle media - lattice models. In: *Advances in Failure Mechanisms in Brittle Materials* (Edited by R. J. Clifton and H. D. Espinosa), pp. 171-184. ASME Press, New York.

Mastilovic S. and Krajcinovic D. (1999a). High Velocity Expansion of a Cavity within a Brittle Material. *Journal of Mechanics and Physics of Solids* **47**: 577-610.

Mastilovic S. and Krajcinovic D. (1999b). Statistical Models of Brittle Deformation, Part Two: Computer Simulations. *International Journal of Plasticity* **15**: 427-456.

Mastilovic S. and Krajcinovic D. (1999c). Penetration of Rigid Projectiles Through Quasi-Brittle Materials. *Journal of Applied Mechanics* **66**: 585-592.

Mastilovic S. and Krajcinovic D. (2005). Particle dynamics simulations of expansion of a cylindrical cavity within an infinite brittle medium. *Theoret. Appl. Mech.* **31** (3-4): 338-348.

Mastilovic S., Rinaldi A., Krajcinovic D. (2008). Ordering effect of kinetic energy on dynamic deformation of brittle solids. *Mechanics of Materials* **40** (4-5): 407-417

Mastilovic S., (2008). On elastic response of disordered triangular lattice during dynamic loading. *Theoret. Appl. Mech*. (Accepted for publication).

Mastilovic S. A note on short-time response of two-dimensional lattices during dynamic loading. *International Journal of Damage Mechanics*. (Accepted for publication).

Melchionna, S., Ciccotti, G., and Holian, B. L. (1993). Hoover NPT dynamics for systems varying in shape and size. *Molec. Phys.* **78**: 533-544.

Mesarovic S.Dj., Padbidri J. (2005). Minimal kinematic boundary conditions for simulations of disordered microstructures. *Philosophical Magazine* **85**: 65-78.

Meyers, M. A. and Aimone, C. (1983). Dynamic fracture (spalling) of metals. *Prog. Mater. Sci.* **28**: 1-96.

Mayers, M. A. (1994). *Dynamic Behavior of Materials*. John Wiley, New York.

Miller, O., Freund, L.B., and Needleman, A. (1999). Modeling and simulation of dynamic fragmentation in brittle materials, *Int. J. Fracture* **96**: 101-125.

Monaghan, J. J. (1988). An introduction to SPH. *Comp. Phys. Comm.* **48**: 89-96.

Monette, L. and Anderson, M. P. (1994). Elastic and fracture properties of the two-dimensional triangular and square lattices. *Modelling Simul. Mater. Sci. Eng*. **2**: 53-66

Mott, N. F. (1947). Fragmentation of shell cases. *Proc. R. Soc. Lon*., 300-308.

Nabarro, F. R. N. (1987). *Theory of Crystal Dislocations*. Dover, New York.

Nemat-Nasser, S., Isaacs, J. B. and Starrett, J. E. (1991). Hopkinson techniques for dynamic recovery experiments. *Proc. R. Soc. Lond. A* **435**: 371-391.

Nemat-Nasser, S. and Hori, M. (1993). *Micromechanics: Overall Properties of Heterogeneous Materials*. North-Holland, Amsterdam.

Nemat-Nasser, S., Deng, H. (1994). Strain-rate effect on brittle failure in compression. *Acta Metall. Mater.* **42** (3): 1013-1024.

Nicholas, T. and Bless, S. J. (1985). High strain rate tension testing. In*: Mechanical Testing*, *Metals Handbook* **8**, 208-214. Am. Soc. Metals, Metals Park.

Nicholas, T. and Rajendran, R. F. (1990). Material characterization at high strain rates. In: *High Velocity Impact Dynamics* (Edited by J. A. Zukas), pp. 127-297. John Wiley & Sons, New York.

Nicholas, T. and Recht, R. F. (1990). Introduction to impact phenomena. In: *High Velocity Impact Dynamics* (Edited by J. A. Zukas), pp. 1-65. John Wiley & Sons, New York.

Nikolaevskii, V. N. (1981). Limit velocity of fracture front and dynamic strength of brittle solids. *Int. J. Engng. Sci.* **25**: 41-55.

Nose, S. and Klein, M. L. (1983). Constant pressure molecular dynamics for molecular systems. *Molec. Phys.* **50**: 1055-1076.

Ortiz M. (1985). A constitutive theory for the inelastic behavior of concrete, *J. Mech. Mater.* **4**: 67-93.

Ortiz, M. (1996). Computational micromechanics. *Computational Mechanics* **18**, 321-339.

Ostoja-Starzewski M. (2002). Lattice models in micromechanics. *Appl. Mech. Rev* **55** (1): 35-60.

Parrinello, M. and Rahman, A. (1981). Polymorphic transitions in single crystals: a new molecular dynamics method. *J. Appl. Phys.* **52**: 7182-7190.

Parrinello, M. and Rahman, A. (1982). Strain fluctuations and elastic constants. *J. Chem. Phys.* **76**: 2662-2666.

Partom, Y. (1993). Ceramic armor resistance to long-rod penetration (R_t) and its dependence on projectile velocity, *Institute for Advance Technology R 0017,* University of Texas at Austin, Austin.

Paterson, M. S. (1978). *Experimental Rock Deformation - Brittle Field*. Springer, Berlin.

Press, W. H., Teukolsky, S. A., Vetterling, W. T., and Flannery, B. P. (1995). *Numerical Recipes in C, The Art of Scientific Computing*. Cambridge University Press, Cambridge.

Raiser , G., Clifton, R. J., and Ortiz, M. (1990). A soft-recovery plate impact experiment for studying microcracking in ceramics. *Mech. Mater.* **10**: 43-58.

Raiser, G. and Clifton, R. J. (1993). High strain rate deformation and damage in ceramic materials. *J. Engng. Mater. Technol.* **115**: 292-298.

Raiser, G. and Clifton, R. J. (1994). Failure waves in uniaxial compression of an aluminosilicate glass. In: *High Pressure Science and Technology-1993* (Edited by S. C. Schmidt and G. A. Samara), pp. 1039-1042.

Rajendran, A. M. (1993). An advanced ceramic model for impact dynamic codes. In: *Proc. 13th Army Symp. Solid Mech*. (Edited by S. Chou *et al*.), pp. 215-231.

Rajendran, A. M. (1994). Modeling the impact behavior of $AD85$ ceramic under multiaxial loading. *Int. J. Impact Engng*. **15**: 749-768.

Rajendran, A. M. and Dandekar, D. P. (1995). Inelastic response of alumina. *Int. J. Impact Engng.* **17**, 649-662.

Rajendran, A. M. and Grove, D. J. (1996). Modeling the shock response of silicon carbide, boron carbide and titanium diboride. *Int. J. Impact Mech*. **18**: 611-631.

Rajendran, A. M. Grove, D. J. and Bishnoi, K. D. (1997). *Analysis of Projectile Penetration Into a SiC / Ti Layered Plate*. ARL-TR-1364, Army Research Laboratory, Aberdeen Proving Ground, MD.

Rapaport, D.C. (1995). The art of molecular dynamics simulation. Cambridge University Press.

Ravichandran, G. and Subhash, G. (1994). Critical appraisal of limiting strain rates for compression testing of ceramics in a split Hopkinson bar. *J. Am. Ceram. Soc*. **77**: 263-267.

Reif, F. (1965). *Statistical Physics*. McGraw-Hill, New York.

Reinhart, J. S. (1975). *Stress Transients in Solids*. Hyperdynamics, Santa Fe.

Rice, M. H., McQueen, R. G. and Walsh, J. M. (1958). Compression of solids by strong shock waves. *Solid State Phys.* **6**: 1-98.

Rice J.R. (1976). Localization of plastic deformation. In: Koiter W.C. (Ed.), Proc. 14th Int. Congress of Theor. And Appl. Mech.. North Holland, Amsterdam, pp. 201-220.

Rice J.R. (1991), Inelastic constitutive relations for solids: an internal-variable theory and its application to metal plasticity, *J. Mech. Phys. Solids* **19**: 433-445.

Rinaldi A, Krajcinovic D., Mastilovic S. (2007). Statistical Damage Mechanics and Extreme Value Theory. *Int. J. Damage Mech*. **16**: 57-76.

Rosenberg, Z., Yaziv, D, Yeshurun, Y. and Bless, S. J. (1987). Shear strength of shock-loaded alumina as determined with longitudinal and transverse manganin gauges. *J. Appl. Phys.* **62**: 1120-1122.

Rosenberg, Z. and Tsaliah J. (1990). Applying Tate's model for the interaction of long rod projectiles with ceramic targets. *Int. J. Impact Engng.* **9**: 247-251.

Rosenberg, Z., Brar, N. S. and Bless, S. J. (1991). Dynamic high-pressure properties of *AlN* ceramic as determined by flyer plate impact. *J. Appl. Phys*. **70**: 167-182.

Ross, C. A., Jerome, D. M., Tedesco, J. W. and Hughes, M. L. (1996). Moisture and strain rate effects on concrete strength. *ACI Mater. J.* **93**: 293-300.

Sairam, S. and Clifton, R. J. (1994). Pressure-shear impact investigation of dynamic fragmentation and flow of ceramics, in: *Mechanical Testing of Ceramics and Ceramic Composites* (Edited by A. Gilat), pp. 23-40.

Sarva, S., Nemat-Nasser, S. (2001). Dynamic compressive strength of silicon carbide under uniaxial compression. Materials Science and Engineering, **A317**: 140-144.

Scagnetti, P. A., Nagem, R. J., Sandri, G. V. H. and Bifano, T. G. (1996). Stress and strain analysis in molecular dynamics simulation of solids. *J. Appl. Mech.* **63**: 450-452,

Senf, H. and Winkler, S. (1997). Experimental investigation of wave and fracture phenomena in impacted ceramics: sapphire. ARL-CR-310. Ernst-Mach-Institute, Weil am Rhein.

Shockey, D. A., Marchand, A. H., Skaggs, H. R., Cort G. E., Burkett M. W. and Parker R. (1990). Failure phenomenology of confined ceramic targets and impacting rods. *Int. J. Impact Engng*. **9**: 263-275.

Sieradzki, K., Dienes, G. J., Paskin, A. and Massoumzadeh, B. (1988). Atomistics of crack propagation. *Acta Metall.* **36**: 651-663.

Stellinwerf, R. F. (1990). Smoth particle hydrodynamics. In*: Advances in Free-Lagrange Method* (Edited by H. E. Trease, M. J. Fritts and W. P. Crowley), pp. 239-257. Springer-Verlag, Berlin.

Sternberg, J. (1989). Material properties determining the resistance of ceramics to high velocity penetration. *J. Appl. Phys.* **65**: 3417-3424.

Strassburger, E. and Senf, H. (1995). *Experimental Investigation of Wave and Fracture Phenomena in Impacted Ceramics and Glasses*. U. S. Army Research Lab., Aberdeen.

Sutton, A. P. and Pethica, J. B. (1990). Inelastic flow processes in nanometre volumes of solids. *J. Phys.: Condens. Matter* **2**: 5317-5326.

Tadmor, E. B., Ortiz, M. and Phillips, R. (1996a). Quasicontinuum analysis of defects in solids. *Phil. Mag*. **73**: 1529-1564.

Tadmor, E. B., Philips, R. and Ortiz M. (1996b). Mixed atomistic and continuum models of deformation in solids. *Langmuir* **12**: 4529-4541.

Tate, A. (1967). A Theory for the deceleration of long rods after impact. *J. Mech. Phys. Solids* **15**: 387-399.

Tate, A. (1969). Further results in the theory of long rod penetration. *J. Mech. Phys. Solids* **17**: 141-150.

Taylor, G. (1947). The use of flat-ended projectiles for determining dynamic yield stress. *Proc. Roy. Soc. Lond.* **194A**: 289-299.

Tersoff, J. (1988). New empirical approach for the structure and energy of covalent systems. *Phys. Rev. B* **37**: 6991-7000.

Trent, B. C. and Margolin, L. G. (1995). Numerical validation of a constitutive theory for an arbitrarily fractured solid. *Engng. Comput*. **12**: 125-134.

Van Mier, J. G. M. (1997). *Fracture Processes of Concrete*. CRC Press, New York.

Vitek, V. (1996). Pair potentials in atomistic computer simulations. In: *Interatomic potentials for atomistic simulations*, *MRS Bulletin* **21**: 20-23.

Voyiadjis G.Z., Kattan, P.I (1987). A plasticity-damage theory for large deformation of solids, *Int. J. Eng. Sci.* **30**: 1089-1108.

Vujosevic, M. (1996). *Damage Mechanics - Critical States*. Ph.D. Dissertation. Arizona State University, Tempe.

Wagner, N. J., Holian, B. L., and Voter, A. F. (1992). Molecular-dynamics simulations of two-dimensional materials at high strain rates. *Phys.Rev. A* **45**: 8457-8470.

Wannier, G. H. (1987). *Statistical Physics*. Dover, New York.

Watson, G. N. (1945). *Treatise on the Theory Bessel Function*. Macmillan, New York.

Weast, R. C. (1976). *Handbook of Chemistry and Physics*. CRC Press, Cleveland.

Weiner, J. H. (1983). *Statistical Mechanics of Elasticity*. John Wiley & Sons, New York.

Wilkins, M. L. and Guinan, M. W. (1973). Impact of cylinders on a rigid boundary. *J. Appl. Phys*. **44**, 1200-1206.

Wright, S. C., Huang, Y., and Fleck, N. A. (1992). Deep penetration of polycarbonate by a cylindrical indenter. *Mech. Mater.* **13**: 277-284.

Yoffe, E. H. (1951). The moving Griffith crack. *Phil. Mag.* **42**: 739-750.

Zallen, R. (1983) The Physics of Amorphous Solids, J. Willey and Sons, New York

Zhou, S. J., Lomdahl, P. S., Thomson, R. and Holian, B. L. (1996). Dynamic crack processes via molecular dynamics. *Phys. Rev. Lett*. **76**: 2318-2321.

Zhou, M., Clifton, R.J., (1997). Dynamic Constitutive and Failure Behavior of a Two-Phase Tungsten Composite. *J. Appl. Mech.* **64**: 487-494.

Zhou, M. (2003). A new look at the atomic level virial stress: on continuum-molecular system equivalence. *Proc. R. Soc. Lond. A* **459**: 2347-2392.

Zukas, J. A. (1982). Numerical simulation of impact phenomena. In: *Impact dynamics* (Edited by J. A. Zukas, T. Nicholas, F. H. Swift, L. Greszczuk and D. R. Curran), pp. 367-418. John Wiley & Sons, New York.

INDEX

W

CIP – Каталогизација у публикацији
Народна библиотека Србије, Београд

531.1/.3
539.42

MASTILOVIĆ, Sreten
Investigation of Dynamic Behavior of Brittle Solids by Discrete Systems / Sreten Mastilovic. – Belgrade : Faculty of Construction Management Union University = Beograd : Fakultet za graditeljski menadžment Univerziteta Union, 2008 (Beograd: Stillart). – X, 152 str. : graf. prikazi, tabele ; 25 cm

Tiraž 100. – Napomene i bibliografske reference uz tekst. – Bibliografija: str. 135-147. – Registar.

ISBN 978-86-85175-02-2

а) Механика чврстих тела б) Механика лома
COBISS.SR-ID 147895820

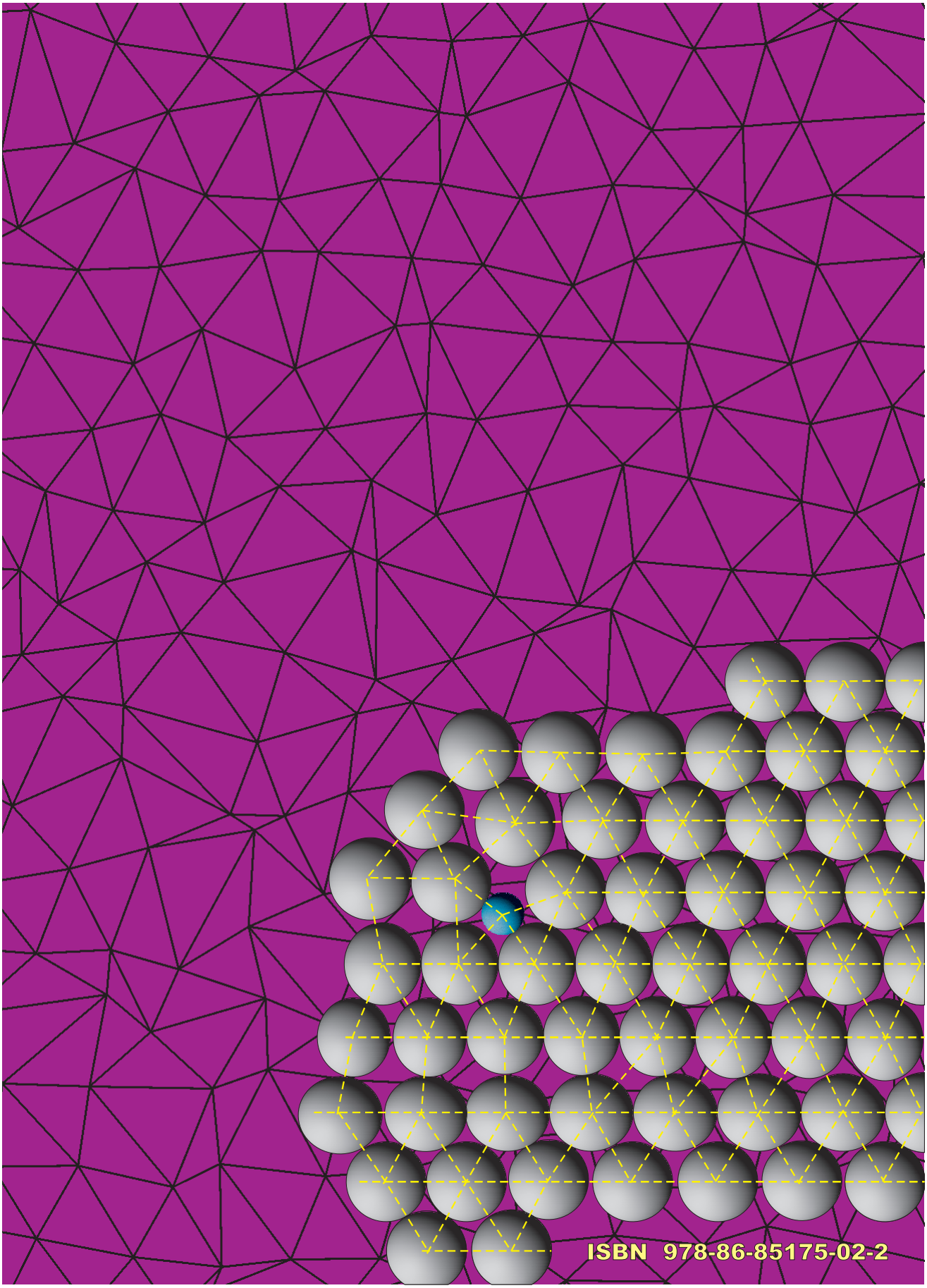

ISBN 978-86-85175-02-2